

# **Local electronic properties of individual nanostructures on the boron nitride nanomesh**

Dissertation zur Erlangung des akademischen Grades  
des Doktors der Naturwissenschaften (Dr. rer. nat.)  
an der Universität Konstanz  
Fachbereich Physik

vorgelegt von

Christian H. Michaelis

Tag der mündlichen Prüfung: 09. Februar 2010

Referent: Prof. Dr. K. Kern

Referentin: Prof. Dr. E. Scheer





Für Heinrich M. Michaelis (\*1932) und  
Heinrich A. Michaelis (1957-1985),  
die ihre Promotion nie beenden konnten.



# Contents

<b>1</b>	<b>Introduction</b>	<b>7</b>
<b>2</b>	<b>STM</b>	<b>11</b>
<b>3</b>	<b>Experimental</b>	<b>19</b>
3.1	General setup of the microscope . . . . .	19
3.2	Improvement of mechanical stability . . . . .	20
3.3	Low temperatures . . . . .	26
3.4	Enhancement in energy resolution . . . . .	37
3.5	Approach control and sample transfer . . . . .	42
3.6	Transfer chamber . . . . .	44
3.7	Possible future improvements . . . . .	47
<b>4</b>	<b>The boron nitride nanomesh</b>	<b>49</b>
4.1	Advantages of the nanomesh . . . . .	50
4.2	Preparation of the nanomesh . . . . .	51
4.3	The partial double layer model or how a Science paper can mislead . . .	53
4.4	Structure of the nanomesh (on different substrates) . . . . .	54
4.5	Apparent height . . . . .	56
4.6	Electronic properties/STS . . . . .	58
<b>5</b>	<b>Cobalt clusters on h-BN</b>	<b>61</b>
5.1	Buffer layer assisted growth . . . . .	61
5.2	STM topography . . . . .	64
5.3	Coulomb blockade gap? . . . . .	67
<b>6</b>	<b>Pb particles on h-BN</b>	<b>75</b>
6.1	Low temperature spectroscopy . . . . .	79
6.2	Quantum and critical fluctuations in the superconductivity of single, isolated Pb nanoparticles . . . . .	84
<b>7</b>	<b>Sn nanoparticles</b>	<b>89</b>
7.1	Superconducting proximity effect . . . . .	89
7.2	Shell effects in Sn nanoparticles . . . . .	90
<b>8</b>	<b>Summary and outlook</b>	<b>99</b>



# 1 Introduction

It is now almost a century since the discovery of phenomena like superconductivity by Kamerlingh-Onnes in 1911 [1] (see figure 1.1) or the formulation of the Bloch theorem [2]. Both are related to bulk materials. The motivation for this thesis is to leave the bulk regime and to study electronic properties at the nanoscale.

In the past decades the scientific interest turned more and more to smaller structures with reduced dimensions. Nanoscale clusters as zero-dimensional systems are important for both fundamental research as well as possible future applications in medical treatments [3] or data storage [4]. For example the length of one single bit on a hard disk is already around 25 nm.

To study such small objects and their electronic properties requires to approach at least two frontiers: obviously high spatial resolution, and low temperatures. The latter for multiple reasons. The diffusion of atoms and molecules is inhibited and the quality of the ultra high vacuum in cryogenic conditions remains stable over extended periods. Even more important is the enhanced energy resolution that is determined by the Fermi-Dirac broadening at the temperature  $T$ :

$$\Delta E \approx 3.2k_{\text{B}}T \quad (1.1)$$

without taking into account any instrumental broadening, external noises or ac modulation. The corresponding energy resolutions are above 1 meV for a helium bath cryostat at 4.2 K, and 0.13 meV at 0.5 K. Thus, the additional experimental effort to reach lower temperatures pays off in a one order of magnitude better energy resolution and a deeper insight in the physics involved.

The third reason is to observe effects that occur only below a certain transition temperature. While many quantum phenomena like the Kondo effect, charge density waves, superconductivity or magnetism can be observed at 4.2 K, others require lower temperatures. Therefore, many aspects of for example suprafluidity, spin lattices or single

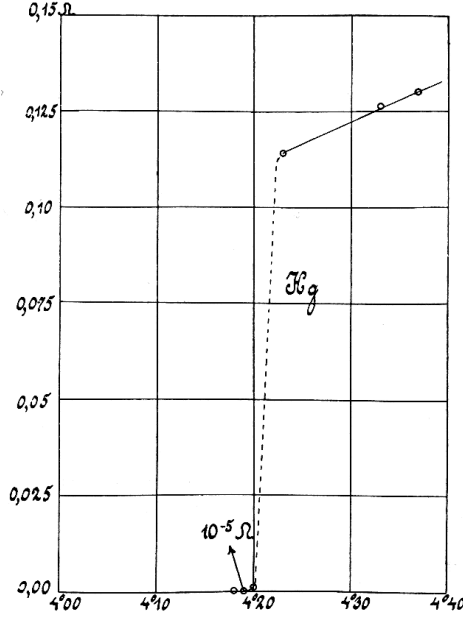


Figure 1.1: Discovery of superconductivity in mercury in 1911 by H. Kamerlingh-Onnes [1]. The superconducting transition temperature needs to be corrected by 50 mK to 4.15 K.

molecular magnets with low blocking temperatures and again superconductivity are waiting to be studied.

A sub-Kelvin scanning tunneling microscope is the perfect tool to combine spatial and energy resolution for local scale spectroscopy. There are more and more low temperature STMs available worldwide. Some reach temperatures below 1 K [5–7], few are installed in dilution refrigerators [8]. Unique for the present work is the combination of low temperatures and sample preparation in ultra high vacuum conditions that overcomes the limitation to cleavable samples.

Examining nanoscale objects with electron tunneling requires a conducting substrate. Since on normal metallic surfaces the adsorbates' electronic structure would strongly hybridize with the substrate's they need to be decoupled. This can be done with a variety of ultrathin films of salts, oxides or nitrides [9–20]. The boron nitride nanomesh [21] used in this work acts additionally as a template on the nanometer scale [22] for small clusters.

The pristine hexagonal boron nitride nanomesh is described in detail in chapter 4. Geometrical and electronic properties are discussed. In the following chapter cobalt clusters are deposited on a partial coverage of the nanomesh. The decoupled clusters

show different electronic features than those directly in contact with the metal substrate. The origin of an electronic gap - initially interpreted as a Coulomb blockade gap - is discussed from another viewpoint taking into consideration the molecular behavior of ultrasmall metallic clusters.

The subsequent chapters concern superconductivity in reduced sizes and dimensions. The transition from bulk superconductors (3D) over thin films (2D) to nanowires (1D) and granular systems/particles (0D) changes many superconducting properties like the London penetration depth  $\lambda_L$  and the coherence length  $\xi_0$  [23–26]. In thin films proximity effects start to play a role. In nanowires quantum phase slips already lead to finite resistivity below  $T_c$ . In granular systems the superconductivity might be microscopically observable but macroscopically destroyed due to phase decoherence. For zero-dimensional superconducting particles the question arises how small a superconductor can be. According to the Anderson criterion superconductivity will vanish as soon as the energy level spacing reaches the superconducting energy gap [27].

There are mainly two effects that influence the evolution of superconductivity with size: surface effects and quantum size effects. Surface effects stem from the larger surface to volume ratio, lead to phonon softening and an increase in the electron-phonon coupling and subsequently to an increase in  $T_c$ . Quantum size effects are e.g. shell effects and quantization of energy levels. For the latter a decrease in  $T_c$  and of the superconducting energy gap is predicted by the BCS theory.

The pioneering work of Ralph et al. triggered this work. They showed the occurrence of the parity effect in the superconducting energy gap  $\Delta$  for Al nanoparticles [28]: chapter 6 deals with individual Pb nanoparticles<sup>1</sup>. Decoupled particles show superconductivity with some striking differences to the bulk behavior. At low temperatures, the influence of quantum fluctuations is observed through a gradual decrease of the superconducting energy gap with a reduction in particle size accompanied by a simultaneous increase in the broadening of the tunneling spectra. At finite temperatures, critical thermal fluctuations give rise to a finite energy gap above  $T_c$  which, surprisingly, extends to temperatures as high as  $1.4 T_c$  for particles below 13 nm.

---

<sup>1</sup>The Pb is called *particle* in contrast to the Co *clusters* in chapter 5. The word (nano)particle is generally used for objects with a transition in the studied properties with decreasing size starting from the bulk. Nanoparticles have typical diameters in the nanometer range while clusters consist of a few to a few thousand atoms and are ruled by quantum effects. According to this definition the smaller superconducting particles should be called clusters. The word particle is maintained for simplicity.

While lead is a strong coupling superconductor similar sized nanoparticles of the weak coupling tin have been studied in the last chapter. Here, shell effects similar to electronic shells in atoms or clusters lead to a completely different observation. The shell effects cause variations in the superconducting energy gap as large as 100 % for particles with heights below 20 nm. The striking difference to the case of the Pb nanoparticles where no such oscillations are observed is due to the shorter coherence length in Pb which suppresses finite size corrections.

## 2 STM

Electron tunneling has been known for many decades and was widely used in layered systems for e.g. superconductor spectroscopy. For a good review see Wolf and references therein [29]. The idea to tunnel through a *vacuum* gap [30] led to the invention of scanning tunneling microscopy. It has been introduced to the surface science in the early 1980ies by Binnig and Rohrer who got the Nobel price for the invention of STM in 1986. This development was a huge enrichment for the community since it allows real space characterization of surfaces on the atomic scale and for non-periodic structures, too.

The main principle [31–34] is strikingly easy: A very sharp probe - the tip - is positioned over a surface in a distance in the range of a few Å. Both tip and sample have to be electrically conducting. The electronic wavefunctions of tip and sample overlap and a tunneling current can flow if a bias voltage is applied. Bias varies typically from  $\pm 10\text{V}$  down to the mV range. Currents are in the order of pA to nA. The corresponding current density is in the order of  $10^{10}\text{ A/m}^2$  due to the small area of tunneling of  $\sim (3\text{ Å})^2$ . The electrical fields in the junction are  $10^6 - 10^{10}\text{ V/m}$ .<sup>1</sup>

According to the simple and successful model of Tersoff and Hamann[35–38] for STM the tunneling current is

$$I(V) \propto \int_{-\infty}^{\infty} \rho_{\text{sample}}(E) \rho_{\text{tip}}(E - eV) \mathcal{T}(E, V, z) (f(E - eV, T) - f(E, T)) dE \quad (2.1)$$

$\rho$  represents the spatially resolved so-called local density of states of the tip or the sample and  $f$  the Fermi function. The transition matrix for the tunneling contact is

$$\mathcal{T}(E, V, z) = \exp \left( -2z \sqrt{\frac{m_e}{\hbar^2} (\Phi_{\text{sample}} + \Phi_{\text{tip}} - 2E + eV)} \right) \quad (2.2)$$

If the applied bias is much smaller than the work functions of tip  $\Phi_{\text{tip}}$  and sample  $\Phi_{\text{sample}}$

---

<sup>1</sup>The presence of the electrical field in the junction can influence the electronic properties like the shifting and splitting of states (Stark effect).

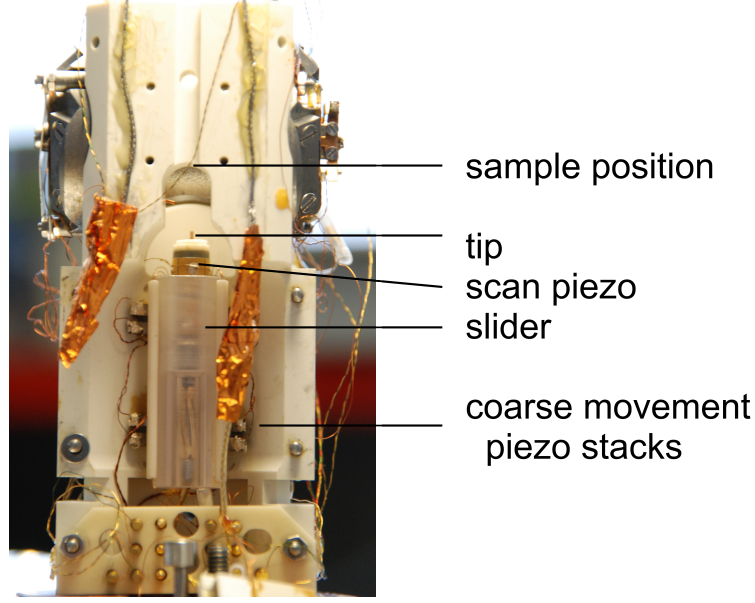


Figure 2.1: Realisation of the STM principle. The tip on top of the scan piezo faces the sample position. The Pan-type slider for the coarse approach is visible below.

the transition coefficient can be simplified by

$$\mathcal{T}(z) = \exp \left( -2z \sqrt{\frac{m_e}{\hbar^2} (\Phi_{\text{sample}} + \Phi_{\text{tip}})} \right) \quad (2.3)$$

Thus, the expression for the tunneling current can be rewritten in the limit of  $T \rightarrow 0$

$$I(V) = \mathcal{T}(z) \int_0^{eV} \rho_{\text{sample}}(E) \rho_{\text{tip}}(E - eV) dE \quad (2.4)$$

In addition to the simplified Tersoff-Hamann model the earlier Perturbation or Bardeen approach<sup>2</sup> [39], the Landauer-Bütticker approach [40, 41], and the Keldysh-Greens function approach [42, 43] should be mentioned.

To position tip and sample with sub Å precision over macroscopic distances (mm) a coarse and a fine positioning system are combined.

Coarse movement is usually done via a slip-stick motion[44]. In beetle (Besocke[45]) type STMs this movement is a rotation on concentric ramps. This very simple and robust setup provides intrinsic x,y coarse movement and is well temperature compensated. In Pan[46] type STMs like the one used in this work the z-motion is purely linear on a sapphire slider between two times three shear piezo stacks (see figure 2.1). They

---

<sup>2</sup>Tersoff and Hamann used the Bardeen approach.



can be driven simultaneously or individually as a walker. This z-motion is extremely reproducible. X,y coarse movement needs to be provided by other means. In the machine used here, a rotor stage allows to change the position in one dimension. Since all coarse movements imply friction they heat up the STM what needs to be considered for low temperature experiments.

For fine positioning and scanning piezoelectric ceramics[47] serve as actuators. The resolution in z is higher than in x,y direction because of the exponential  $I(z)$  dependence. The z distance needs to be feedback controlled[48] in the pm regime.

Figure 2.1 shows the realisation of the main principle. The tip is mounted on the central scan piezo. The outer electrode is divided in four (plus one) sectors allowing the x,y scanning and the z movement. Four out of six coarse movement shear piezo stacks are hidden behind the slider while two have been removed together with the leaf spring for demonstration.

For STM topography there are mainly two different modes: constant current and constant height. In the latter the feedback is switched off and the tip scans over the surface reading a current map. This is rarely used. Usually topography images are taken in constant current mode. The feedback loop corrects the z-distance in order to keep the tunneling current constant. The difference signal  $\Delta I = I - I_0$  is fed back to the z-piezo. This results in a z-height map of the surface topology.

Note that the STM is sensitive to the integrated local density of states (equation 2.4) and not the "true" height. So STM images can deviate with bias and tip significantly [49, 50] since they contain both topographic and electronic information of the surface and the tip.

As tip materials normal, paramagnetic, polycrystalline metals are used in most of the cases. Tungsten tips (electrochemically etched in NaOH) are widely used for imaging purposes. They are very sharp but require UHV treatment like sputtering or high temperature flashing to remove their oxide layer. Platinum, iridium or Pt/Ir tips are easier to prepare with side-cutting pliers and do not oxidize in air. They are blunter than tungsten tips and especially iridium tips are electronically featureless around  $E_F$  and therefore often used for spectroscopy.

For some systems a tip exchange is crucial. In variable and room temperature systems the diffusion of atoms and molecules on the tip may require a tip exchange. The same holds for studies on e.g. semiconductor substrates where a tip crash often destroys the metallic character of the tip. In the case of a metal substrate the tip can be prepared via dipping in the sample surface. Small voltage pulses or in severe cases high voltage

field emission can be used to clean the tip<sup>3</sup>. In general the tip preparation (for metallic tips) is exaggerated: All results of this thesis have been measured with the very same tungsten tip.

Besides the normal metal tips there are three classes of outstanding tips for special purposes: Molecular, (anti-)ferromagnetic and superconducting tips. The first class describes the modification of the tip with a molecule. Hydrogen or carbon monoxide are two recent examples [51, 52] where the molecules are used to enhance the intramolecular contrast in imaging adsorbed molecules.

The second class are (anti-)ferromagnetic tips for spin polarized tunneling where tip and sample act as a spin valve. Fe, Cr, Ni, Gd etc. tips are used, often prepared in situ via dipping in the sample or by direct evaporation on the tip [53, 54].

Superconducting tips consist mostly of a bulk superconductor like niobium or can be formed by dipping directly into a superconducting sample [55–57]. Their use is not very common due to the limitations in the low energy regime inside the superconducting gap which prohibits tunneling. By exceeding the critical field and/or temperature of the tip this limitation can be overcome.

The most promising application for superconducting tips is the spin polarized tunneling. The superconducting excitation spectrum can be Zeeman splitted in a magnetic field resulting in energy shifted spin polarized coherence peaks [58]. As tip material a type II superconductor with a sufficiently high critical field or an enhanced critical field due to size effects is required. In planar tunneling junctions thin superconducting films were used together with an in plane applied magnetic field. The superconductor has to have a low spin-orbit-coupling and a reachable critical temperature. Metallic tips dipped in V or bulk V<sub>3</sub>Si are promising candidates.<sup>4</sup> As a result selective spin polarized tunneling at low biases and low temperatures becomes feasible.

Even more powerful than the imaging modes and the possible atom manipulation is the tunneling spectroscopy. For the most common  $I/V$  and  $dI/dV$  spectroscopy the bias is swept and the current as well as the  $dI/dV$  signal are recorded simultaneously using a lock-in technique. The feedback remains open to keep the tip-sample-distance constant. The bias is modulated with a small AC signal. The  $dI/dV$  is proportional to

---

<sup>3</sup>+600 V to the tip with a current of typically 20  $\mu$ A for 20 min. The tip apex might melt locally.

<sup>4</sup>With a tungsten tip dipped in a Pb(111) sample the critical field could be enhanced to 1.75 T compared to the bulk value of 80 mT (at 4.2 K). But Pb is a strong coupling superconductor not suitable for the desired experiment.

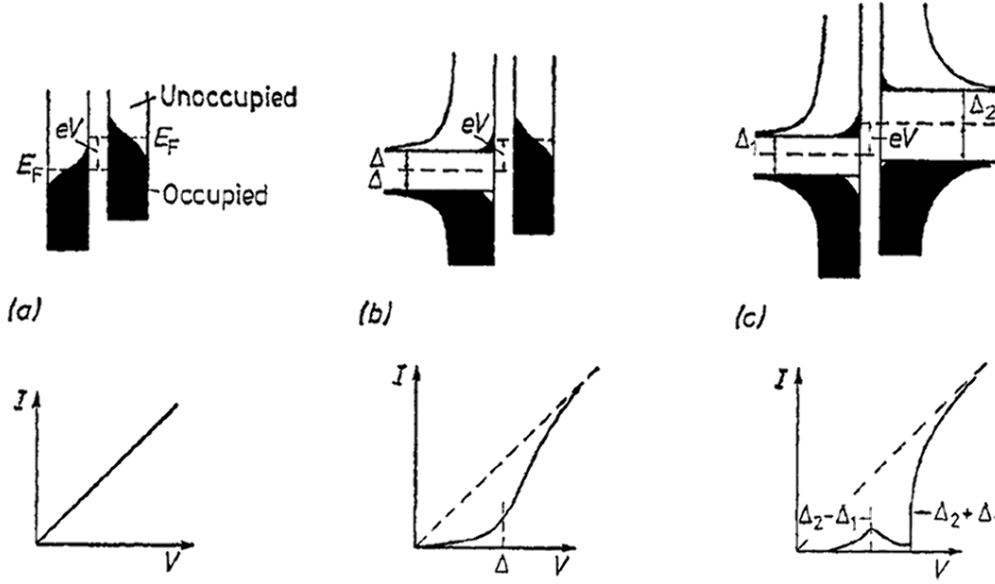


Figure 2.2: I-V characteristics and their origins for (a) metal-metal (b) metal-superconductor and (c) superconductor-superconductor tunnel junctions at finite temperatures. (Reproduced from E.L. Wolf [29].)

the local density of states in the small voltage regime as derived from equation 2.4.

$$\frac{dI}{dV} \propto \rho_{\text{sample}}(eV)\rho_{\text{tip}}(0) \quad (2.5)$$

Figure 2.2 illustrates the current obtained for three different types of junctions: two normal metals, normal metal-superconductor and superconductor-superconductor at finite temperatures below  $T_c$ . For  $T = 0$  the superconducting density of states has the form

$$\rho(E) \propto \begin{cases} \frac{|E|}{\sqrt{E^2 - \Delta^2}} & \text{for } |E| > \Delta \\ 0 & \text{for } |E| < \Delta \end{cases} \quad (2.6)$$

where  $\Delta$  is the superconducting energy gap. At finite temperature the spectra are thermally broadened as illustrated in the figure. The derivative  $dI/dV$  of real and typical cases of the two latter can be found in figures 3.9 on page 36 (2.2(b)) and 3.13 on page 41 (2.2(c)).

Beside the  $dI/dV$  spectroscopy there are many more spectroscopy modes like  $z(V)$  for image potential states,  $I(z)$  for the work function or  $dI/dV$  along a line or even maps to resolve spatial variation of electronic features. Even full spectroscopic imaging with

complete  $I/V$  and  $dI/dV$  spectra for each image point (highly long term stable systems required) becomes more and more popular. It provides additionally to the local *periodic* electronic properties, too.

So far only elastic processes without energy loss have been considered. But there are many important inelastic processes that have an impact on the tunneling current. The second derivative  $d^2I/dV^2$  (the derivative of the conductance) describes the inelastic contribution. Since inelastic processes are mostly manybody interactions they are usually less probable. The instrumental requirements concerning external vibrations are generally higher ( $< 0.5$  pm) than for other spectroscopy modes.

The most common application for this type of spectroscopy is the detection of vibrations and phonons. (Vibrations in crystal lattices are called phonons in contrast to vibrations in molecules, clusters or atoms.) Molecular vibrations have been studied by Stipe et al. who achieved chemical sensitivity by probing the carbon-hydrogen stretch mode in (partially deuterated) acetylene [59, 60]. Recently Gawronski et al. published a highly debated paper about phonons in gold and copper crystals [61]. Apart from that A. Heinrich et al. measured spin excitation with inelastic electron tunneling spectroscopy [13]. They observed the spin flip of single Mn atoms decoupled from the substrate.

I want to mention another very mighty but less known spectroscopy mode that adds  $k$ -resolution to the STM: Fourier transform scanning tunneling microscopy/spectroscopy (FT-STM).

The method has been described by Petersen et al. [62] who used it to determine the two-dimensional Fermi contour of surface states via a Fourier transform of STM images. The parabolic dispersion of the Au, Cu, Ag etc. (111) surface states follows the free electron model

$$E(k_{\parallel}) \sim \frac{\hbar^2 k_{\parallel}^2}{2m^*} \quad (2.7)$$

where  $m^*$  is the effective electron mass.

What is seen in the STM are long range LDOS oscillations (Friedel oscillations) around step edges or impurities that screen the local disturbance and fall off with  $r^{-2}$  on a surface

$$\Delta\rho(r) \propto \frac{1}{r^2} \cos(2k_F r + \Phi) \quad (2.8)$$

where  $k_F$  is the Fermi wave vector and  $\Phi$  the phase shift. The observed oscillations are not true Friedel oscillations. They would contain all frequencies from 0 to  $2k_F$  resulting in a solid disk instead of a ring in the FT image. In the STM energy resolved Friedel

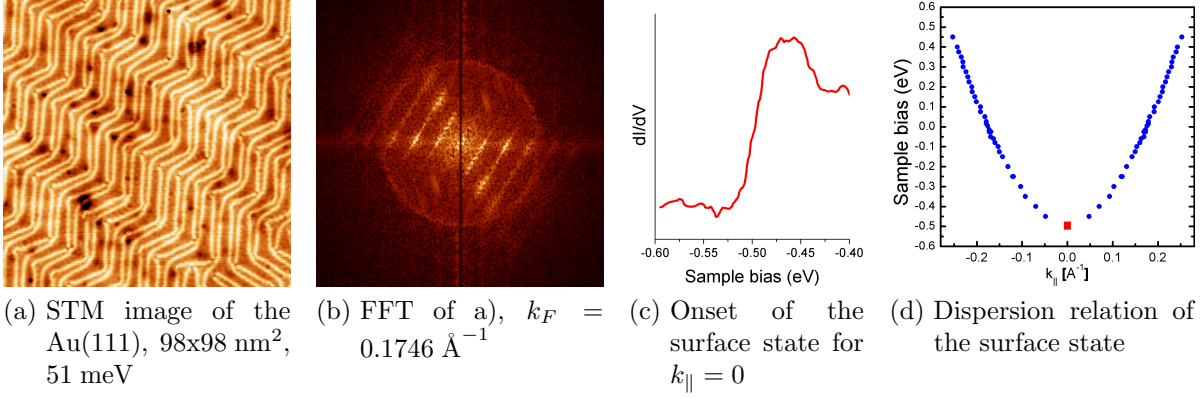


Figure 2.3: Determination of the dispersion relation (of the Au(111) surface state) with Fourier transform STM.

oscillations with  $q = 2k_F$  are visible.

The main steps to the dispersion relation are illustrated in figure 2.3 for the example of the surface state on Au(111):

1. STM images or  $dI/dV$  maps are acquired at different sample biases. The terraces should be large especially for the low  $k_{\parallel}$  contributions just above the onset of the surface state. The number of image points needs to be a power of 2 for the FFT.
2. The image is Fourier transformed. Applying the 2D-FFT to a (real space) STM image leads to the complementary image in  $k$  space displaying the two dimensional Fermi contours. Radial averaging of the FFT image helps to determine  $k_F$ . The herringbone reconstruction can be seen in the FFT image as well.
3. The onset of the surface state is determined from standard  $dI/dV$  spectroscopy where the steepness is a measure for the lifetime [63]. The onset can be seen as a red square for  $k_{\parallel} = 0$  in the dispersion relation in figure 2.3d.

Similar results can be obtained with  $dI/dV$  spectra along a line perpendicular to a step edge [63, 64]. Both methods of FT-STM are superior to photo emission spectroscopy in the sense of spatial resolution, the speed, the simplicity and the probing of occupied and unoccupied states. A disadvantage is the limitation to s and p type contributions in the Fermi contour.

Besides its high capabilities STM has some limitations:

- It lacks chemical sensitivity. For exceptions see e.g. [59, 65].

- Insulators can only be studied as thin films on conducting substrates. Semiconductors need high doping levels at low temperatures. Tuning fork STM/AFM combinations overcome this problem [66]. They offer an even higher resolution since they are not limited to the DOS [52].
- The surface needs to be clean. Although tunneling in air or electrolytes is possible, UHV conditions are required to keep the samples free of unintentional adsorbates and/or diffusion must be frozen at low temperatures.
- The tip apex is unknown but must present a reproducible and stable electronic behavior.
- The tunneling contact is very sensitive to external vibrations.

All these restrictions require a sophisticated experimental environment that will be described in the following chapter.

## 3 Experimental

To get the microscope running and to achieve sub Kelvin performance was the main experimental part during my thesis.

The system was built up by P. Messina and later by G. Wittich [67]. When I started the microscope could operate at a minimum temperature of 2.7 K, had a vibrational noise of dozens of pm depending on the daytime and condition of the microscope and the electronic noise was by far higher than what one expects for a low temperature STM. This situation was highly unsatisfactory and was tackled (point by point over time and not necessarily in the order) as I will describe in the following sections.

### 3.1 General setup of the microscope

The subK STM is an STM in a  $^3\text{He}$  Joule-Thomson cryostat with in-situ UHV sample preparation and transfer in the STM. The base pressure is  $5 \cdot 10^{-11}$  mbar. The vacuum chamber has three main parts: a preparation chamber with a sputter gun, sample heater and cooler, evaporators, an Auger electron analyzer and leak valves. This gives the possibility to prepare clean metal and semiconductor surfaces with a variety of adsorbates and thin films. The second chamber is the main chamber with a sample storage, access to a load lock and wobble-stick transfer from the preparation chamber to the third chamber - the STM tube that hangs freely inside the cryostat.

The superisolated  $^4\text{He}$  bath cryostat hangs below the main chamber and can be loaded from the top with a 2 m manipulator. Two radiation plugs can be put in the STM tube to avoid room temperature radiation to the sample. The cryostat has a 14 T superconducting solenoid magnet<sup>1</sup> with a 78 mm bore. 16 T are achievable if the  $^4\text{He}$  bath is pumped to the  $\lambda$  point at 2.2 K.

For maintenance at the STM the cryostat can be lowered from the sixth to the fifth floor of the building with a forklift. In the fifth floor is everything needed for the gas

---

<sup>1</sup>Cryogenic, London, UK

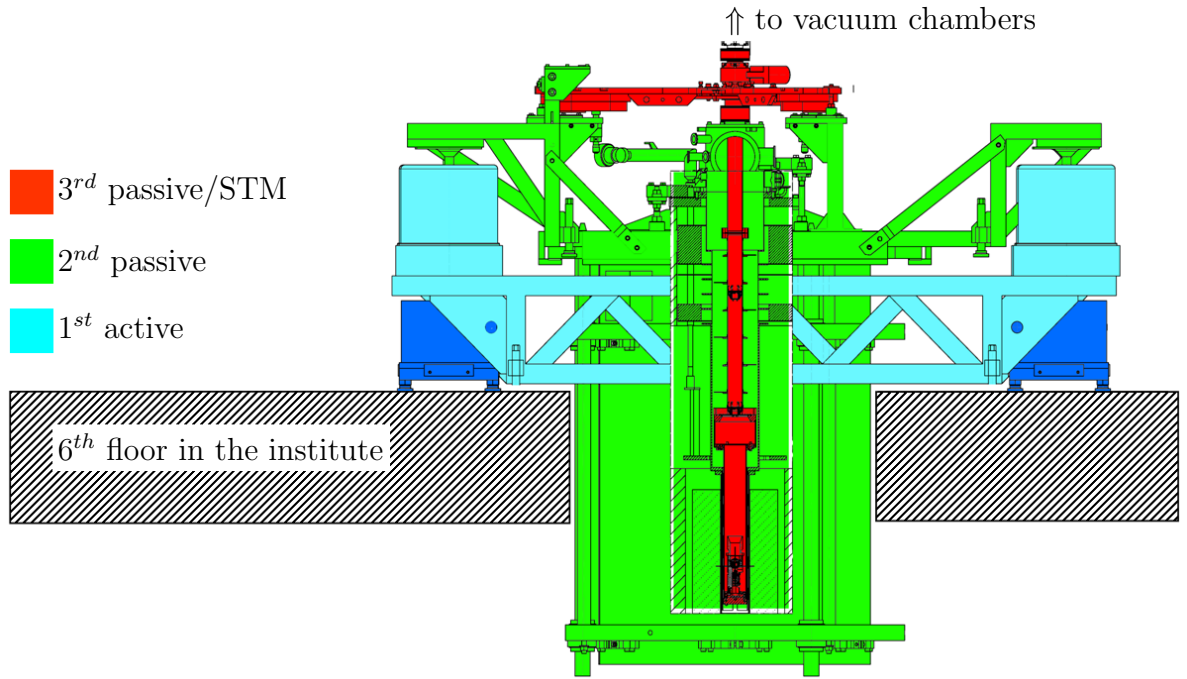


Figure 3.1: The three vibration isolation stages of the system. Cyan: actively damped frame, green: passively damped frame with the cryostat and the vacuum chambers above it (not shown), red: the star (STM UHV tube with STM and lead weights)

handling: the  $^3\text{He}$  pump, the  $^3\text{He}$  reservoir, a liquid nitrogen cryo trap and most of the valves to run the cycle.

## 3.2 Improvement of mechanical stability

Mechanical stability is a key issue in any STM since the tunneling current depends exponentially from the tip sample distance (equation 2.3.  $z$ -noise  $dz$  will result directly in current noise [68].

$$dI \propto \exp\left(-2\sqrt{2}\frac{m_e}{\hbar}\sqrt{\Phi}dz\right) = \exp\left(-\frac{1.0225}{\sqrt{eV}\text{\AA}}\sqrt{\Phi}dz\right) \quad (3.1)$$

with  $\Phi$  being the average work function. As a rule of thumb 1  $\text{\AA}$  height difference create one order of magnitude in current. Vibrations of 10 pm will result in 20 % noise in current (from eq. 3.1).

Hence, careful vibration isolation is crucial. Here it is done via a three stage damping system. The first stage is an active one. The two following are passive isolators. The



second stage still carries all the vacuum chamber and the cryostat. The mass of approximately 1.5 t rests on four standard Newport I-2000<sup>2</sup> pneumatic isolators. They have a pronounced resonant frequency of 1.6 to 1.8 Hz and damp all the above frequencies very well. Many STMs situated on a reasonable floor (in the basement) and equipped with an eddy current damping have nothing but these dampers. Eddy current damping is not possible in microscopes with high magnetic fields so the third stage (called star) consists of three Newport CM-225<sup>3</sup> passive air dampers. They show a resonant frequency of 3.6 to 4.0 Hz. Their maximum load is 30 kg per isolator. Thus the maximum load including the aluminum frame of the star and the STM tube plus lead weights is limited to 90 kg. An overview is given in Figure 3.1.

Figure 3.2 shows the misery of the transmission of external vibrations to the STM and the stepwise improvement of the situation. Figure 3.2a shows the initial situation at day time. The vibrational noise was 60 pm at best, often worse. External vibrations were directly seen in the tip-sample distance. The STM head could be improved noticeably with stiffer springs for the sample-rotor and the z-slider. As a result the vibrational noise could be lowered. Reasonable measurements could still only be done between 10 pm and 5 am when external disturbances were small.

The by far best improvement was the installation of new active dampers. It was always clear that active damping is required in the 6<sup>th</sup> floor of the building especially for a pendulum-like system like the subK with an elevated center of mass. The first generation active dampers TS-200<sup>4</sup> did not work at all. Their feedback could not compensate the vibrations and the system easily went to resonant conditions.

The second generation of active dampers (AVI-400S/M<sup>5</sup>) did not show these resonances anymore. They start to damp above 4 Hz. The noise in the STM was still 7 pm at night with the stiffened STM head.

Unfortunately the ranges of the three damping stages were not complementary. The AVI-400S/M have a vertical transmission well above 1 for low frequencies in the subHz range up to 3 Hz. But any excitation of the system in the low frequency range will be transmitted to the STM since the passive stages have eigenfrequencies in the very same range (1.6 – 1.8 Hz and 3.6 – 4.0 Hz). Even worse, there are the building eigenfrequencies at around 3, 7 and 11 Hz. They are usually excited by the normal institute's life, the

---

<sup>2</sup>Newport, Irvine, USA

<sup>3</sup>Newport, Irvine, USA

<sup>4</sup>JRS, Zwillikon, Switzerland

<sup>5</sup>TableStable, Zwillikon, Switzerland

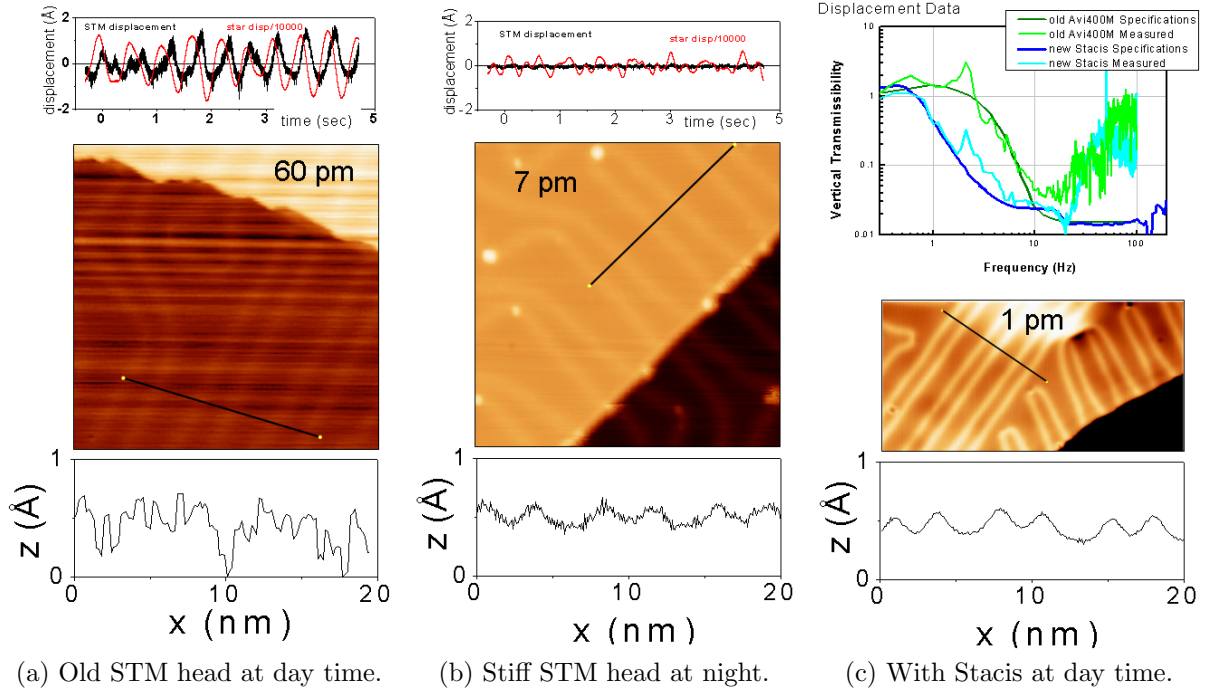


Figure 3.2: Improvement of the mechanical stability of the STM. The top row illustrates the transmission of external vibrations at the third damping stage (star) to the tip-sample displacement<sup>6</sup>. In the middle is a typical STM image at 4.2 K on Au(111). The herringbone reconstruction is clearly visible. The linescans at the bottom show the z-noise perpendicular to the reconstruction and off the fast direction. The new stiff head is less affected by external vibrations the z-noise is reduced from 60 – 200 pm down to 7 nm. The installation of the TMC Stacis active dampers allow z-noises lower than 1 pm.

road traffic, construction works and enhanced by strong winds (the lab is at the upper outer end of a long building) and earthquakes. Earthquakes are not so seldom as one might think. In the region of between Stuttgart and Basel (Switzerland) low magnitude earthquakes happen quite often and can be seen as long wavelength oscillations (subHz to few Hz range) for a few minutes.

The installation of TMC's Stacis 2100<sup>7</sup> brought the desired performance. The controller has in addition to the common feedback that reacts on external vibrations an additional feed forward. The feed forward predicts future disturbances resulting in a better isolation at low frequencies from 0.6 Hz. The interplay with the passive stages

<sup>6</sup>The current was measured and compared to the workfunction (calculated from  $I(z)$  data) to calculate the tip-sample displacement curves at the top of Figs. 3.2a and 3.2b.

<sup>7</sup>TMC, Peabody, USA

is much better. The noise flattens especially in the slow direction of a scan and for spectroscopy.

The only disadvantage is the acoustic noise created by the piezo actuators in the range of 300 to 700 Hz. They do not act as passive isolators as the earlier systems did for medium and higher frequencies but do even create noise. The structure-borne sound is damped by the two following passive stages. The airborne sound<sup>8</sup> inside the soundproof hutch for the microscope is a more severe problem since the STM is acoustically very sensitive. Apparently the gas pressure in the  $^3\text{He}$  volume of the cryostat plays a major role here. The sound propagation in the helium gas is enhanced for gas pressures starting to disturb from about 0.5 mbar but a certain gas pressure is required in order to maintain the thermal contact of the STM to the  $^4\text{He}$  bath. Pressures around 0.1 mbar are a very good compromise to fulfill both requirements<sup>9</sup>.

All these measures provide the possibility to measure without any external disturbances. But the Joule-Thomson cycle requires a rotary pump and the original decoupling for the 100 mm diameter pumping line was not sufficient. All lines have to be helium leak tight stainless steel. (An external home-built sorption pump immersed in a transport vessel was tested but turned out to be insufficient for the high gas loads.)

The modified pumping line was thinner (40 mm) without any loss in performance and more flexible in comparison to the stiff 100 mm tubing. In addition the line was attached to the actively damped frame with an ultra flexible metal tube to the passive frame. From the active frame the line was connected to a rubber supported heavy mass and later mounted directly on the floor. This provides the desired vibration isolation for tunneling with the pump running.

While external disturbances may be minimized internal sources are difficult to control. There are mainly two: boiling helium and the magnet. Boiling helium creates a resonance above 100 Hz shifting with the filling level in the cryostat. The helium recovery metal corrugated tube created resonances and made the system dependent on other experiments running in neighboring labs. The solution was to use only the topmost exit of the cryostat with a long soft silicon tube. Standing waves that were created when using lower exits of the cryostat can be avoided and the 10 m rubber tube decouples from the institute recovery's resonances without wasting helium.

Running the magnet in STM turned out to be more difficult. The strong fields bridge

---

<sup>8</sup>Airborne noise can be identified easily since it does not change from stage to stage.

<sup>9</sup>Unfortunately the breakdown voltage according to Paschen's law [69, 70] has a minimum of  $\sim 150$  V in this helium gas pressure range.

the first and also the last damping stage, and induce a temperature rise in the STM head. How can that happen?

- The solenoid magnet has a considerable stray field that couples to the steel reinforcement in the concrete of the 6<sup>th</sup> floor. The magnetic field bridges the active damping stage and acts as a low pass causing more low frequency vibrations in the system.
- Induced eddy currents in the metallic parts of the STM (tube) heat the microscope by 1 or 2 K while ramping the field. With a constant magnetic field the temperature settles rapidly, only the increased helium boil off from the superconducting switch may disturb as long as the magnet is not used in the persistent mode. The (axial) field inside the bore is homogeneous enough that small vibrations (mostly vertical) do not result in eddy currents.
- The most severe problem is the bridging of the last damping stage at high fields. Usually the STM tube hangs freely inside the cryostat with a gap of approximately 1 mm on each side to the cryostat's inner wall. Until fields of 5 T it is with some efforts possible to align the STM tube. Unsuitably some parts of the STM tube are found to be ferro-magnetic: The UHV feedthroughs have nickel pins, the gold plated pins at the STM contact plates have a nickel diffusion barrier, too. The used stainless steel is slightly ferro-magnetic and the weldings are even more ferro-magnetic<sup>10</sup>. In addition all the standard stainless steel screws turned out to be permanently ferro-magnetic after they have been exposed to high fields.
- Really worrying is a spring that holds the scan piezo with the tip inside the sapphire prism of the coarse approach. It was taken from a standard banana connector and is ferro-magnetic, too. This spring is most likely the part that makes the scan position drifting over half the accessible range from 0 to 8 T what requires careful planning to probe the very same place at different magnetic fields.

All these constrictions limited the microscope's performance in high magnetic fields. Some are or will be abolished soon. Measurements up to 8 T are already possible. However, to decouple the chamber from the steel reinforcement concrete requires a different location of the system. Then experiments that are not possible so far become accessible.

---

<sup>10</sup>Only austenitic stainless steels are used for the STM tube. 1.4429 for the flange and 1.4301 for the tube parts (both  $\mu_r \sim 1.05$ ). In the heat affected zone of the welding ferrites may precipitate. These ferrites are bcc and magnetic. [71]

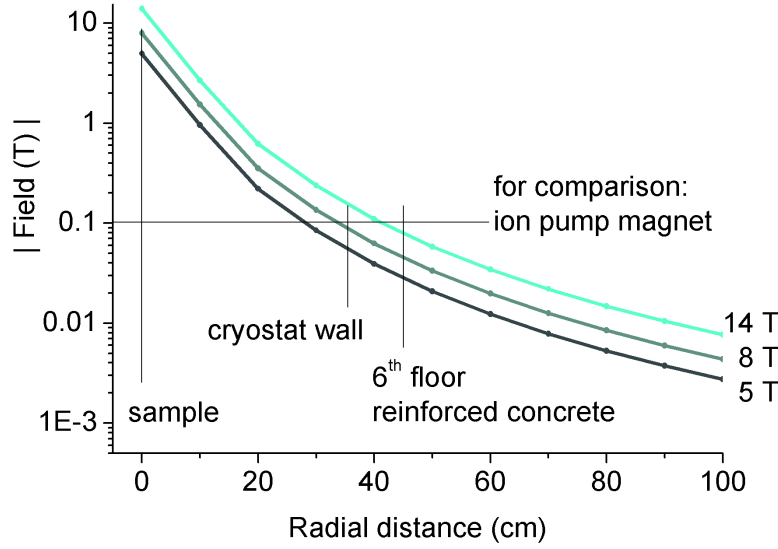


Figure 3.3: Radial stray field of the solenoid superconducting magnet. The field close to the cryostat is of the same order of magnitude as a strong ion pump magnet (100 mT). For vibrations the magnetic field acts as a low pass bridging the active damping stage.

One example would be the observation of the spin split surface state in Au(111)[72, 73] that requires beside low temperatures and high energy resolution a magnetic field of at least 10 T.

As a final remark I'd like to mention the vibration measurements. Airborne sound can be measured with a microphone. For structure-borne noise there are a couple of vibration sensors available. In the subK two VA-2<sup>11</sup> piezo-electric accelerometers are used to monitor the vibrations of the two passively damped frames all the time together with an Agilent digital FFT scope<sup>12</sup>.

These devices can display acceleration, velocity or displacement. Since they are piezo ceramics with an inertial mass they measure acceleration ( $k \cdot x = m \cdot a$ ) internally and calculate the other two. It came out that the active dampers show pretty high transmissions when measured in acceleration mode while they seem to work perfectly in displacement mode measurement. This is understandable considering that they do not have any passive high frequency damping. The better performance of the STM with the Stacis 2100 justifies the verification of the dampers' functioning in displacement mode.

Another critical point in vibration measurements is the limited sensitivity of the sensors used. Even for the VA-2 there are huge difference of one order of magnitude between

<sup>11</sup>VA-2, JRS, Zwillikon, Switzerland

<sup>12</sup>Infinium 54831D MSO, 2 Gsamples/s, 600 MHz, Agilent, Santa Clara, USA

the serial numbers 17/18 and 60/62 respectively. While 17 and 18 are able to measure any disturbing noise in the third stage the 60 and 62 have an internal multiplexing that results in a higher baseline noise and worse sensitivity. A comparison with many international labs (IBM Almaden, Berkeley, Cornell, MIT and NIST Maryland) showed that many of them measure the frequency dependent sensitivity of their vibration sensors[74]. True geophones can fill the gap but are usually not required if there is no impact on the STM.

### 3.3 Low temperatures

When I started working at the system the minimum temperature was only 2.7 K. There were a few ideas what might go wrong but warming up from liquid helium to room temperature needs one to two weeks<sup>13</sup>. Together with the repair (one more week), baking the UHV part, careful testing and finally cooling down with liquid nitrogen and liquid helium at least three usually four weeks are required. So any change in the STM, the cryostat or wiring must be well deliberated and carefully planned. Sudden changes in the cryogenic part of the system are just impossible.

Over time it became more clear in what operating modes the cryostat<sup>14</sup> can be operated and how lower temperature regimes become accessible. Along the way there were (and still are) many counterintuitive and often contradicting results. Now there are mainly four different operation modes along with many issues of the cryogenic parts which will be explained:

- 4.2 K <sup>4</sup>He bath with optional heater
- 2.7 K <sup>3</sup>He Joule-Thomson cycle in continuous and single shot mode
- 1.3 K <sup>4</sup>He cycle
- 0.8 K <sup>3</sup>He cycle in single shot mode with "1 K pot"

---

<sup>13</sup>It is possible to blow out remaining liquid helium with room temperature helium gas. To vent the isolation vacuum of the superisolation with 100 mbar of helium gas (30 mbar overpressure valve required) leads to rapid warming within one or two days. Anyway, although the cryostat's manufacturer agreed on this procedure, it is difficult to pump the helium from the isolation vacuum. A reduced hold time and a noisier environment from the higher boil off enhanced by Taconis oscillations [75] can be avoided with multiple dry nitrogen gas flushings.

<sup>14</sup>Cryovac, Troisdorf, Germany

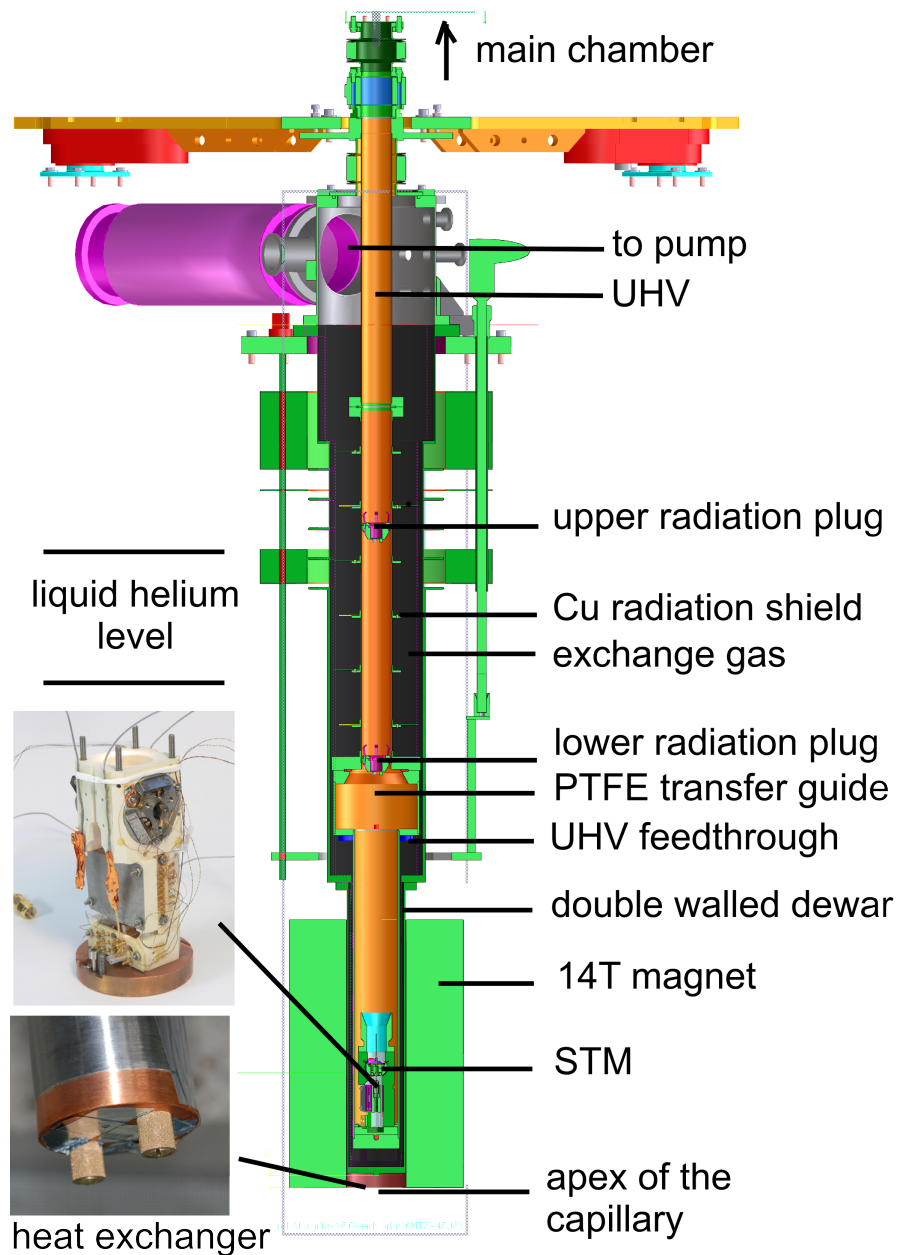


Figure 3.4: Insert of the cryostat with the  $^3\text{He}$  part, the UHV STM tube and the superconducting magnet. The insets show the STM without the Cu cone on top (upper) and the heat exchanger at the bottom of the STM tube (lower). The cryostat has been omitted for clarity.

The very first operation mode, the 4.2 K  $^4\text{He}$  bath cooling is the easiest and the most often used but somehow most trivial one. The temperature can be varied by the number of radiation plugs in the STM tube: 4.2 K with two, 4.3 K with one, 7.0 K without radiation plugs. If the STM tube's UHV gate valve is opened and light shined in the STM tube around 12 K can be achieved. But the higher the temperature, the higher the boil off and the corresponding noise. All these bath cooling operation modes require a minimum of 0.1 mbar of helium exchange gas in the rough vacuum part of the cryostat to couple to the liquid helium bath. Without exchange gas the temperature can even rise further.

To cool down a sample from room temperature it takes less than one hour for 7 K and around four hours for 4.x K. Thus, for fast sample characterization it is not required to put both radiation plugs and wait such long times for drift-free thermalization.

In principle temperatures higher than 4.2 K could be obtained via low exchange gas pressures [76] and/or the amount of radiation in the STM tube. This won't be very convenient since only certain temperatures were accessible and thermalization (especially cooling down) took a lot of time. For the variable temperature option a 42  $\Omega$  foil heater<sup>15</sup> has been implemented at the bottom of the STM tube, not in the UHV but in the exchange gas part. The temperature can be selectively tuned up to a few tens of Kelvin with mK precision. The resulting thermal drift in the nm-range fades rapidly after the temperature is settled.

The second operation mode (what the cryostat is built for) is to run the  $^3\text{He}$  Joule-Thomson cycle:  $^3\text{He}$  gas is compressed, precooled and expanded from high to low pressures through an orifice isenthalpically[77]:

The  $^3\text{He}$  gas is taken from a 50 l reservoir and pumped with 65 m<sup>3</sup>/h sealed rotary pump<sup>16</sup> through two serial liquid nitrogen cryo traps<sup>17</sup> in a circle to clean the gas for about 20 min before putting in in the cryostat. Apparently all the rotary pumps have a gas ballast switch. In the  $^3\text{He}$  version of the pump this gas ballast is closed. Not - as one might think - permanently but overpressure valve like with a spring. Above 2 bar all the  $^3\text{He}$  is lost and exchanged with air<sup>18</sup>.

---

<sup>15</sup>ThermoFoil flexible Kapton heater, Minco, Minneapolis, USA.

<sup>16</sup>Trivac D 65 B two stage rotary pump, Oerlikon-Leybold, Pfäffikon, Switzerland.

<sup>17</sup>H6-103 liquid nitrogen cryo trap, Oxford Instruments, Oxfordshire, UK. The overpressure valves (to air) were exchanged to in-line adjustable overpressure valves. These valves were glued with Torrseal that cracked and opened a leak. Teflon tape provided low temperature stable joints.

<sup>18</sup>The prices for  $^3\text{He}$  were stable for a long time around 150 Euro/l. In late 2008 the price rose to more than 800 Euro/l and dropped in 2009 to around 400 if the suppliers could deliver at all.



After the gas has been cleaned in the cryo traps, the valve to the cryostat will be opened. The gas is precooled in a long copper tube in the  $^4\text{He}$  gas above the liquid helium bath to use the enthalpy of the  $^4\text{He}$  gas instead of boiling off more liquid. In the liquid helium there is a sintered metal heat exchanger that acts as a hydrogen trap to avoid clogging (at the apex) of the capillary.

This clogging used to be a severe problem. Initially it was attributed to hydrogen since the capillary opened upon warming up to more than 20 K when the cryostat runs empty. This hydrogen was supposed to stem from the pump's oil cracking products. Diffusion in Viton gaskets can be excluded since only stainless steel VCR lines with metal gaskets and all metal diaphragm valves<sup>19</sup> are used. Later the clogging could be avoided by moving the nitrogen cryo traps from the fifth floor closer to the cryostat in the sixth floor and by closing the above mentioned leaks in the cryo traps overpressure valves.

In the bottom part inside the cryostat the capillary leaves the liquid helium bath and enters the double walled dewar that separates the  $^4\text{He}$  bath from the  $^3\text{He}$  part thermally. It continues to spiral down. Here the material is Cu-Ni. The gas should be liquefied by backflowing gas before it expands at the very apex. A part of it will be collected as liquid at the bottom of the double walled dewar, the rest will be pumped with the rotary pump and reinjected in the cryostat. The temperature should go down to 0.5 K while the cycle is running.

So far the theory. But the temperature in the subK is only 2.7 K at the sample while running the cycle in continuous mode. To check the behavior additional Cernox<sup>20</sup> sensors have been placed at the STM beside the existing one at the rotor/sample: two outside the UHV in the  $^3\text{He}$  volume: at the bottom of the STM tube and one at the last radiation shield where all the cables are anchored. Two more inside the UHV: one at the copper base plate and one at the Shapal STM body. The base plate sensor was later moved to the copper transfer cone on top of the STM body.

The result is shown in figure 3.5. The deviation of the sample temperature from the  $^3\text{He}$  gas temperature is striking. The reason was not clear at that time. It was thought that hot cables may introduce heat from the room temperature parts. Additional low temperature cable filters<sup>21</sup> did not improve the situation and have been removed after-

---

<sup>19</sup>HM20 UCV UHP, Ham-Let, Lindfield, UK

<sup>20</sup>Lakeshore Cryotronics, Westerville, USA

<sup>21</sup>Low temperature filter design from C. Debuschewitz (skin effect copper powder filters) [78] or H. le Sueur (meander filter)[79] was considered but is not required. Electron and phonon temperature do not deviate relevantly above 300 mK.

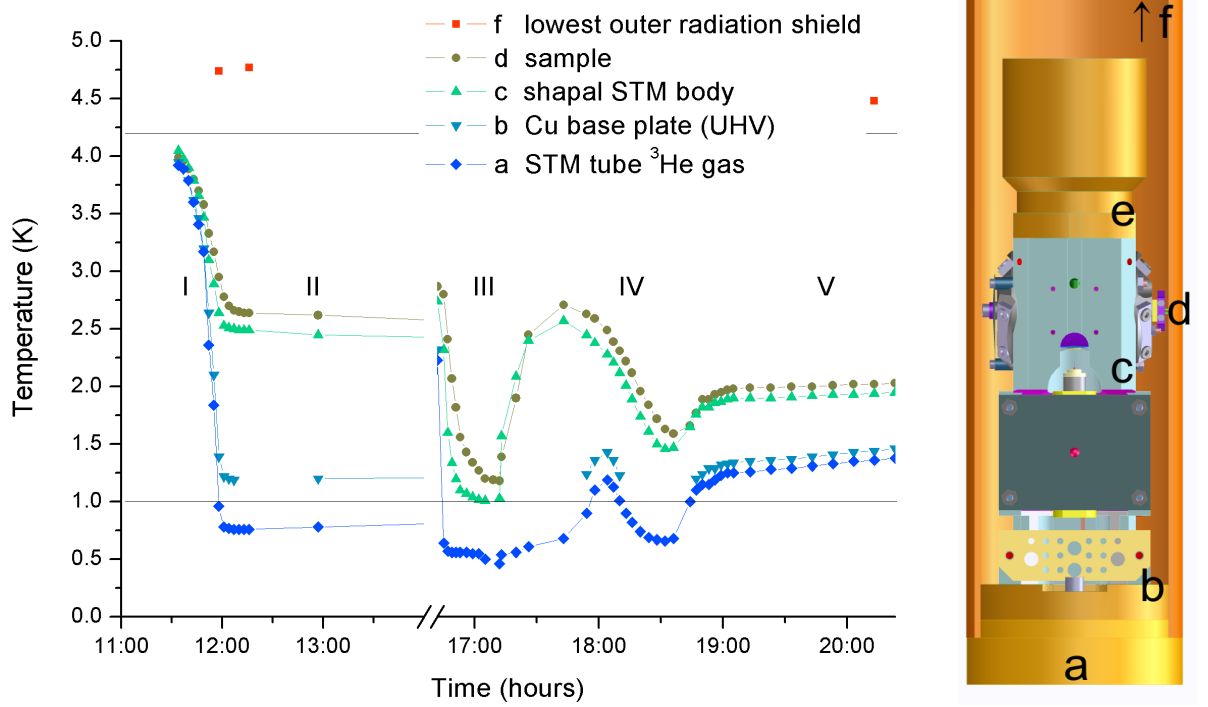
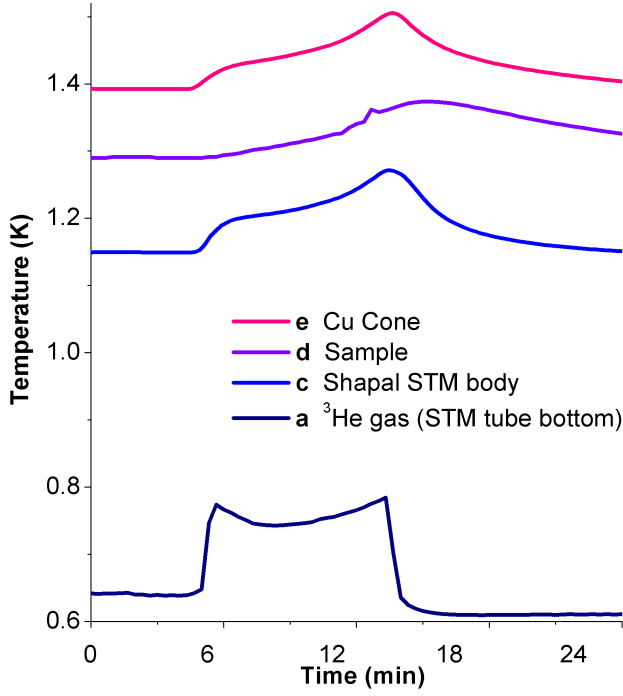


Figure 3.5: Temperatures at different positions of the STM (right) while running the Joule-Thomson cycle with  $^3\text{He}$  gas.

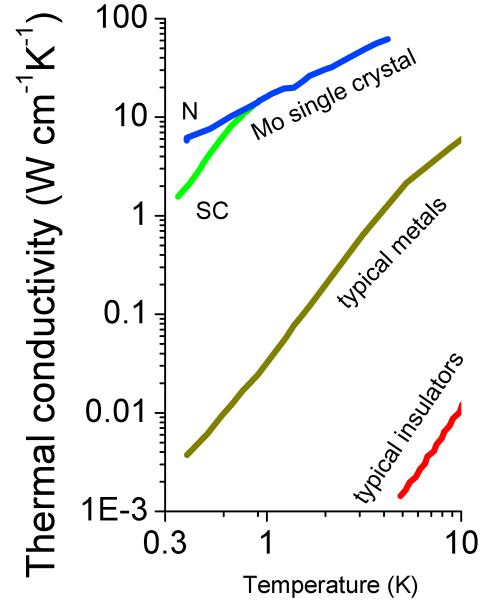
**a** Bottom of the STM tube directly in the  $^3\text{He}$  gas **b** Cu base plate to mount the STM inside the STM tube **c** Shapal STM body **d** Sample/rotor. **e** Cu cone to guide during the sample transfer **f** lowest radiation shield 45 cm above where all the cables are anchored (not shown). **b-e** in UHV **a**, **f** in  $^3\text{He}$  gas.

**I** The cycle starts with rapid cooling down from 4.2 K. **II** 2.7 K in continuous mode. **III** Pumping the pressurized gas from the capillary and sudden pumping at the liquified  $^3\text{He}$  leads to min 0.46 K in the cryostat. **IV** Again cooling down in single shot mode with more gas in the cycle. The minimum temperature is higher than in III because the waiting time before opening the pumping line was shorter leading to worse precooling of the incoming gas. **V** Steady state in single shot mode without any pumping. 2 K +20 mK/h at the sample for 5 h.

The difference between the positions is obvious: The lowest radiation shield is always around liquid helium temperature as it should be. The Cu base plate and the  $^3\text{He}$  gas follow each other closely. Their temperature is defined by the vapor pressure curve for  $^3\text{He}$  (max. 50 mbar after several hours). The sample and the STM body have similar temperatures but far above the gas temperature. The difference is appr. 3 K for the continuous mode and appr. 1 K in the single shot mode when the heat load from incoming gas is absent.



(a) Reaction on a sudden temperature change in the  $^3\text{He}$  gas in single shot mode (same labels as in figure 3.5).



(b) The values for superconducting and normal Mo (single crystal) differ only by a factor of 5. Typical polycrystalline metals like Cu or brass have intermediate and insulators (AlN, PTFE) low conductivities.

Figure 3.6: Thermal conduction inside the STM (a) and thermal conductivities (b). Values for (b) taken from [81, 82]

wards. The last radiation shield where all the cables are anchored is steadily at liquid helium temperature as long as a tiny bit of exchange gas is present.

Later the bad thermal conductivity of the shapal (AlN based machinable glass ceramic) STM body was considered as the reason for the difference. Indeed the thermal conductivity drops by several orders of magnitude from 10 to 1 K<sup>22</sup> but so does the thermal capacity.

Let's look on the response to a sudden temperature change in the  $^3\text{He}$  gas operated in single shot mode (what has not been done so far): The UHV parts show the above mentioned offset to the gas temperature (see figure 3.6a). But while the STM body and the Cu cone react fast, the sample reacts very inertly. This was first attributed to the lower thermal conductivity of molybdenum sample holder below its superconducting

<sup>22</sup>Low temperature thermal conductivity data is not available for Shapal but only for similar AlN based ceramics.[80]

transition temperature of 0.9 K. But the single crystal thermal conductivity values (see figure 3.6b) do not differ more than half an order of magnitude from each other (polycrystalline molybdenum will conduct less) and the STM temperatures were always well above molybdenum's  $T_C$ . The better explanation gives the weak connection of the sample inside the rotor via the six piezostacks point-contacts. A loose or broken rotor spring worsens the conductivity further.

What tells even more about the situation is the fact that the cone is hotter than the sample and the STM body. Cables are not attached to the cone. So radiation is the only explanation. It scales quartically with  $T^4$ .

$$\dot{Q}[W] = 5.67 \cdot 10^{-12} A[cm^2](T_1^4 - T_2^4) \quad (3.2)$$

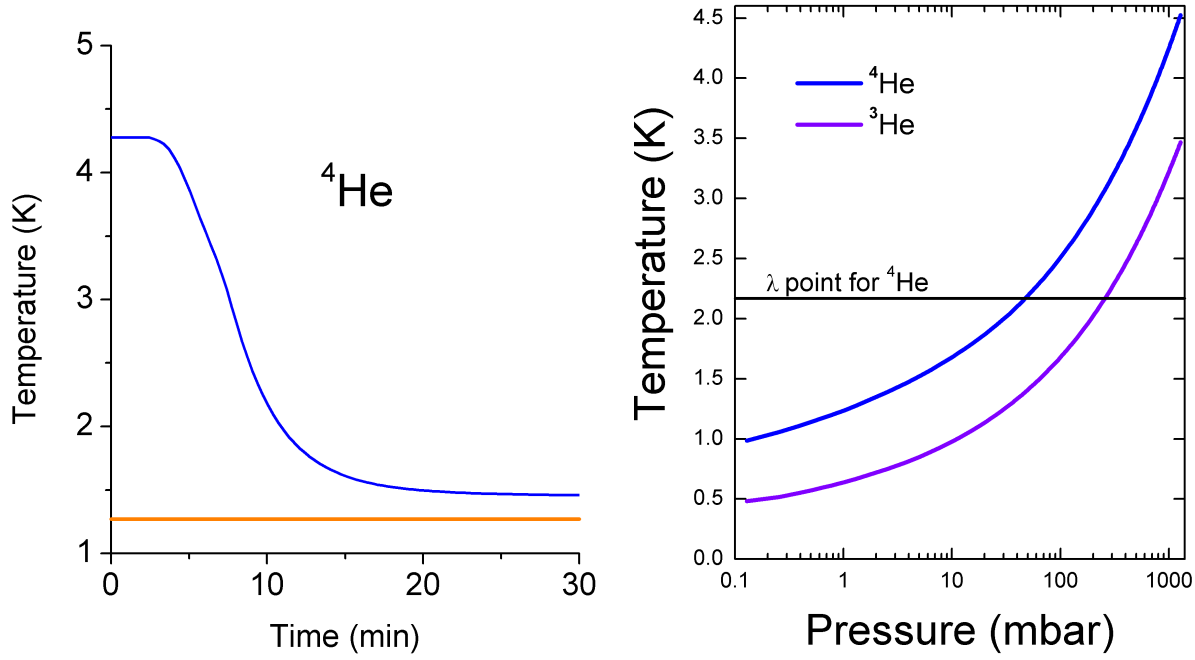
Any part hotter than 100 K would cause a considerable heat transfer. There was a huge  $\varnothing 60$  mm x 120 mm PTFE part 20 cm above the sample. It might have been the radiation source and can explain the degradation over days in base temperature observed in the  $^4\text{He}$  gas Joule-Thomson cycle. But this part was exchanged recently and did not improve the situation.

At the same time the Cu cone on top of the STM body was thermally anchored to the cold Cu base plate below the Shapal body. This change increased the sample temperature from 4.2 K to 4.6 K. The only possible explanation again is radiation. Apparently the removable radiation plugs inside the UHV tube are insufficiently anchored. The idea was to make the radiation plugs from copper or bronze instead of stainless steel and PEEK. Their surface should be polished and not sand blasted.

Pressing down the radiation plugs with the vertical manipulator for 20 min helps to thermalize faster and to cool the sample from 4.6 K to 4.2 K. Only very recently the source of this particular problem could be eliminated. It was a tiny misfit in the angles at the bottom of the radiation plugs. A small amount of light could pass if the plug was not well pressed. Changing this angle solved the problem. The sample is now routinely at 4.2 K with only one radiation plug and cools down in less than half an hour from room temperature.

To run the Joule-Thomson cycle with  $^4\text{He}$  gas is by far easier. Everything can be controlled from the sixth floor and only a gas bottle and a pump are needed. Clogging of the capillary can be avoided by a liquid nitrogen cryo trap.

The base temperature was 1.32 K depending on how long the system (and the ra-



(a) Temperature evolution at the sample while running the Joule-Thomson cycle with  $^4\text{He}$  gas in continuous mode with roots and rotary pump. 1.58 bar capillary gas pressure, 0.4 mbar at the top of the cryostat, two radiation plugs.  
 (b) Theoretical vapor pressure curves for both helium isotopes.  $^3\text{He}$  has a higher vapor pressure at a given temperature due to its lower mass.

Figure 3.7: The final temperature at the sample (left) is not only determined by the vapor pressure curve (right) but depends on how long the system could thermalize after the last sample transfer. After one day [two days, one week] the base temperature is 1.7 K [1.4 K, 1.32 K (orange line)].

radiation plugs!) could thermalize after the last sample transfer. This mode allows fast temperature changes over a wide range. Especially temperatures between 3 and 4.2 K are hardly accessible with  $^3\text{He}$  cooling in the single shot mode. (Above 3 K the  $^3\text{He}$  evaporates quickly and the temperature will jump to 4.2 K.)

Liquefaction of  $^4\text{He}$  was not successful but the improved pumping line (see page 23) allowed to run the cycle in continuous mode. For  $^4\text{He}$  the specific heat falls with  $C_V \sim T^3$  and below 2.17 K the suprafluid helium creeps up the walls of the double walled dewar, heats up to higher temperatures and evaporates quickly. The thermal conduction of the thin suprafluid helium film is the biggest heat source in this configuration.

The pressure in the capillary is independent of the amount of gas inserted from the external gas bottle. It always follows the vapor pressure curve according to the temperature in the outer helium bath. Pumping the outer bath reduces the bath's and consequently the capillary's temperature leading to a new equilibrium pressure in the

capillary (the same as the outer bath!). Below the  $\lambda$  point (4.2 K) in the outer bath the helium should become suprafluid. The flow  $\dot{V}$  is according to Hagen-Poiseuille

$$\dot{V} = \pi R^4 \Delta p / (8 l \eta) \quad (3.3)$$

with  $R$  the tube's inner diameter,  $\Delta p$  the pressure difference and  $l$  the tube's length. The flow should change drastically since the viscosity  $\eta$  drops dramatically below the  $\lambda$  point [83]. This transition was never observed with the flow meter or pressure/temperature sensors since condensing of incoming gas when starting the cycle results always in a huge flow through the flow meter that has no correlation with the flow through the apex of the capillary. Pumping the outer bath did not improve the base temperature when the cycle was run with  $^4\text{He}$ .

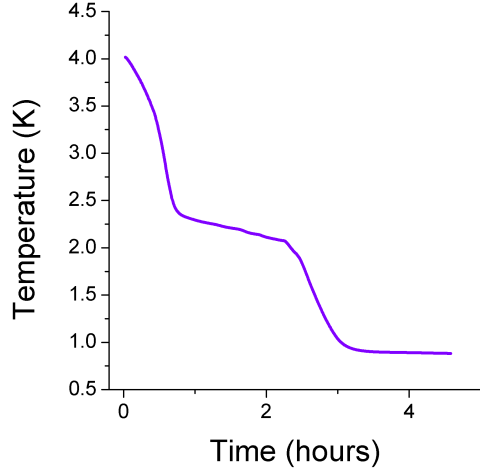
The  $^4\text{He}$  becomes suprafluid in the bottom part of the capillary where it is decoupled from the outer bath by the double walled dewar and cooled by the backflowing expanded gas. This cooling below the  $\lambda$  point is independent of the precooling in the outer bath. This explains also the difference in flow between the two isotopes.  $^3\text{He}$  does not reach its suprafluid state (2.6 mK) and has a one order of magnitude lower flow rate. Consequently the cooling power that is already lower for  $^3\text{He}$  is diminished further by the weak flow of only a few tens of sccm (1 mbar  $\cdot$  l/s equals 55.2 sccm). The flow rate for  $^4\text{He}$  is a few hundred sccm in steady state operation. It can appear much higher as long as gas is liquefied in the capillary. The similar system in IBM Almaden has a flow of 400 sccm for  $^3\text{He}$  being much higher than the flow in the subK. They can not work with  $^4\text{He}$  gas since the flow would be too high.

When the cycle is operated with  $^3\text{He}$  pumping the outer helium bath acts like an additional 1 K pot. The problem could already be seen in figure 3.5 on page 30 where in the continuous mode (II) the heat load from the incoming gas is too high. Figures 3.8a and 3.8b illustrate the effect of pumping on the outer bath while running the cycle with  $^3\text{He}$ .

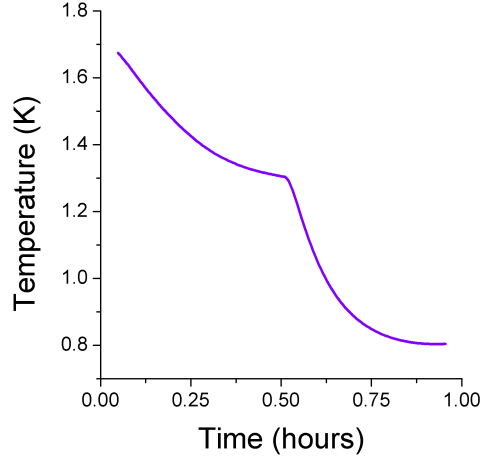
Apparently the incoming  $^3\text{He}$  is not sufficiently precooled and consequently not condensed in the capillary what requires less than 3 K at 1 bar. There was a small known heat leak in the double walled dewar that couples the CuNi capillary to the outer helium bath and could prohibit the liquefaction<sup>23</sup>. But most probably the backflowing gas pressure is just too low due to the wimpy flow. Less pumping power would improve the heat exchange but increase the base temperature.

---

<sup>23</sup>It has been exchanged recently but not tested with  $^3\text{He}$  yet.



(a)  $^3\text{He}$  cycle and helium bath pumping started at the same time. After 2 hours the outer bath is cold enough to liquefy  $^3\text{He}$  in the capillary. The temperature drops to 0.8 K.



(b) Here the outer bath is pumped first and in the middle of the graph the  $^3\text{He}$  cycle was started.

Figure 3.8: Sample temperatures while running the Joule-Thomson cycle with  $^3\text{He}$  and pumping the outer  $^4\text{He}$  bath below 50 mbar. The base temperature is the same in both cases.

Since pumping the outer bath requires roughly 40 % of the liquid to cool down to 2 K reducing the standard maximum holding time from four to two days and because pumping the outer bath takes a few hours the capillary will be widened in the very near future.

Another point of discussion and confusion is the thermometry. Calibrated Cernox<sup>24</sup> sensors in SD package are used. They are specified from room temperature down to 0.3 K with less than 0.5 % error at 4 T and only a few percent at 10 T. They are negative temperature coefficient resistors and the recommended excitation for the four point measurement is 10 mV (63  $\mu\text{V}$ , 20  $\mu\text{V}$ ) for temperatures higher than 1.2 K (0.5 K, 0.1 K).

The readout took place via a home-built device with 10 mV excitation for all temperatures. The polarity is constant over time. Later a Lakeshore 340 temperature controller was used. It provides a thermal compensation that changes the polarity to compensate for temperature differences and the resulting Seebeck effect among the 4 leads. There is a temperature induced bias of a few  $\mu\text{V}$  on the leads leading to wrong temperature

<sup>24</sup>CX-1030-SD-HT-0.3, Lakeshore Cryotronics, Westerville, USA

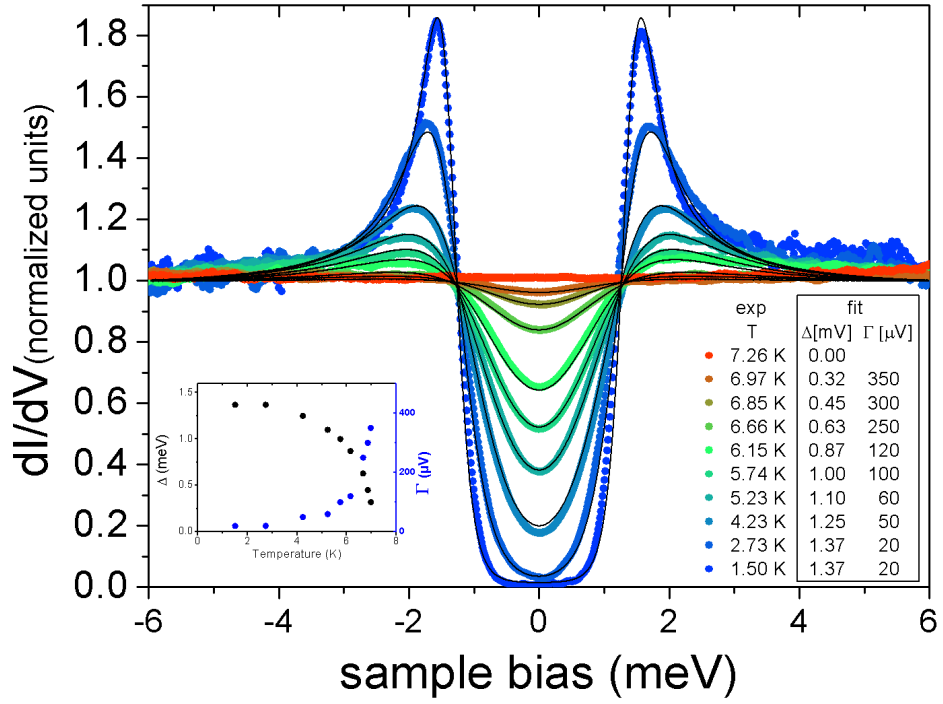


Figure 3.9: Tunneling spectra with a superconducting Pb tip on Rh(111) to verify the sample temperature from 7.26 K (red) to 1.5 K (blue). The BCS fits (black lines) match the measured data points perfectly. The inset shows the evolution of the fitting parameter  $\Delta$  and  $\Gamma$  according to eq. 6.5 with temperature. Modulation was 50  $\mu$ eV



readings in the order of  $\pm 1$  K with excitations lower than 10 mV. But the thermal compensation gives noise in the tunnel junction and thus can not be used when tunneling. In the end higher excitations than recommended are used and as shown in figure 3.9 the temperature reading is correct. And due to the negative temperature coefficient of the sensor the heat dissipation remains small<sup>25</sup>.

### 3.4 Enhancement in energy resolution

The theoretical energy resolution of an STM is determined by the thermal broadening and the bias modulation from the lock-in amplifier[89]:

$$\Delta E \approx \sqrt{(3.2k_B T)^2 + (2\sqrt{2}eV_{mod, RMS})^2} \quad (3.4)$$

Note, that the addition of both terms is only a simplification. The contribution of the ac signal is a cycloid with the zero point at  $\pm V_{mod, peak\ to\ peak}$ . The Fermi broadening is determined only by the tip temperature and the prefactor depends on the experiment. For inelastic processes it is 5.5 instead of 3.2.

Figure 3.10 illustrates the influence of the lock-in modulation at different temperatures on the resolution. The lower the temperature the smaller the bias modulation has to be. At 1 K 100  $\mu$ eV would already diminish the resolution. In any case the theoretical limit can only be reached if all other noises disturb less than the thermal broadening. This concerns vibrations in the tip-sample distance (see section 3.2) as well as and even more important electronic noises. Their impact differs on the spot:

**xy-noise** is by far less disturbing than **z-noise** due to the exponential current dependence of  $dI/dz$  (see equation 3.1). At a gain of 5  $\text{\AA}/\text{V}$  at low temperatures 1 mV electronic z-noise translates to 0.5 pm of vibrational z-noise. Since the vibrational noise is below 1 pm the z-out of the electronic has to provide a stability better than 1 mV. This turned out to be a problem with the old home-built electronics. It was developed by A. Schneider and its software was equipped with many useful features for the daily use in STM. Anyway, the change to the Createc system<sup>26</sup> brought the desired stability in z.

<sup>25</sup>The sensor resistance increases with decreasing temperature. At a constant excitation of 10 mV the heat dissipation (sensor self heating) decreases with decreasing temperature.

<sup>26</sup>LT-STM Electronics, SPS-CreaTec, Erligheim, Germany

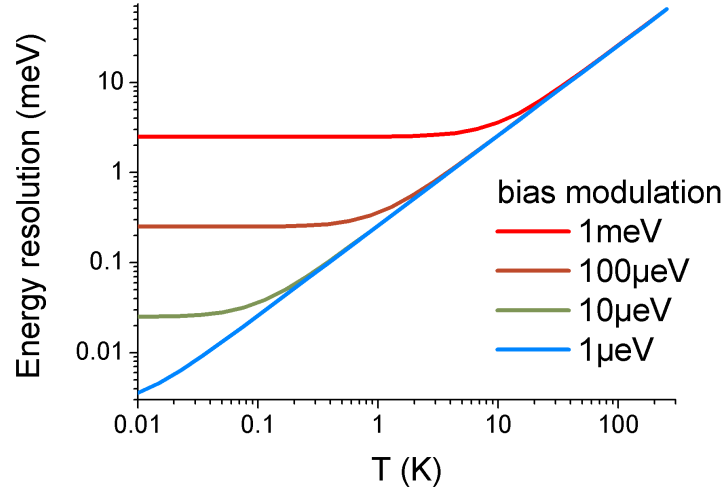


Figure 3.10: Theoretical energy resolution in scanning tunneling spectroscopy for different bias modulation energies. The linear asymptote denotes the temperature of the tip, the horizontal lines the modulation influence in equation 3.4.

Among all the others the current and bias cables are the most crucial. **Current** noise limits the ability to measure at very low currents but does not influence the energy resolution. For STS and topography it can easily be averaged out. In the subK the current noise is around 1 pA at the analog to digital converter. Depending on the feedback settings this noise level allows to measure at currents down to 5 pA (I-V-Converter<sup>27</sup> gain  $10^9$  V/A) what is slightly above the theoretical limit of the Nyquist noise

$$\bar{I} = \sqrt{\frac{4k_B T}{R} \Delta f} = \sqrt{\frac{4k_B 300 \text{ K}}{50 \Omega} \cdot 1.2 \text{ kHz}} \approx 0.6 \text{ pA} \quad (3.5)$$

or the specifications of the I-V-Converter ( $4.3 \text{ fA}/\sqrt{\text{Hz}}$  at a bandwidth of 1.2 kHz). A  $100 \Omega$  resistor in front of the current ADC reduces the noise additionally.

The **bias** used to have a huge 50 and 150 Hz noise<sup>28</sup>. 100 Hz and multiples that usually originate from rectifier power supplies were not present after the ion pumps got a home-built controller without ripples. The original Varian power supply<sup>29</sup> had a rippling of 35 V at 7 kV creating a mechanical vibration inside the ion pump plus electronic noise.

The reason for the 50 Hz are mostly ground loops that catch the 50 Hz from the

<sup>27</sup>DLPCA-200, Femto, Berlin, Germany

<sup>28</sup>Computer screens are well known for 150 Hz problems. The USB connection from the PC to the Createc STM electronics is optically decoupled and the PC plus the screens should not be connected with a separation transformer.

<sup>29</sup>MidiVac, Varian Vacuum Technologies, Leini, Italy

normal grid. Careful star-like grounding of the chamber and all controllers etc. can avoid ground loops to a certain extend[90, 91].

The subK had several ground loops. To get rid of them it was necessary to disconnect the system from all electric connections and the common ground of the institute until only a  $> M\Omega$  resistance to the common ground remained. Then the required cables were connected one by one. All devices are driven via single phase isolating transformers<sup>30</sup> and grounded star-like via the chamber's central grounding point.

As a rule of thumb there should not be more than 20 m $\Omega$  between any parts of the electric installation. If 16 mm<sup>2</sup> cables (thick rubber isolated copper cables) are used they have a resistance of 1 m $\Omega$ /m without any contact resistance. So special care has to be taken to ensure the low-resistive connection since the control rack is more than 5 m away from the STM chamber. The cable shoes have to be properly squeezed and well screwed.

In addition it was necessary to disconnect the STM from the gas handling in the fifth floor, the cooling water and all the peripheral devices that are not driven via a separation transformer. For this reason a ceramic break was installed for the <sup>3</sup>He capillary and the pumping line was separated with a plastic joint or removed if possible.

Despite all these measures the Createc electronics provides a rather noisy bias out with a shifting thermal offset of  $\pm 3$  mV varying with the room temperature and the incident solar radiation. This is not a unique problem of this lab but was reported by all the groups using the very same electronics. A normal 300 Hz bias filter was not sufficient to reduce the bias noise and got support from a battery driven eight-node 10 Hz filter<sup>31</sup> before the lock-in modulation was added. For fast spectroscopy the resulting offset is rather high due to the delay of the filters but can be compensated in the data evaluation. The version 3.0 of the Createc software AFMSTM has a software correction for the bias offset that does not solve the thermal drift problem and contains new bugs.

Let's summarize: z is stable, small noises in current do not limit the resolution and bias is now rather clean as well. Nevertheless it was impossible to measure a superconducting gap. Measurements on Pb(111) as well as Pb/Cu(111) did show clean surfaces and atomic resolution (see figure 3.11). Unfortunately spectroscopy did show a broad and flat gap where one would expect a rather deep and narrow superconducting gap at 4.2 K.

The issue was discussed with many low temperature STM groups worldwide. One

---

<sup>30</sup>KSTF 500 VA and later upgraded to KSTK 1500 VA due to quality problems with the thermo-fuses in the KSTF. Ismet AG, Villingen-Schwenningen, Germany

<sup>31</sup>Transmission:  $\sim 1$  at 10 Hz,  $5 \cdot 10^{-3}$  at 20 Hz,  $< 3 \cdot 10^{-4}$  above 30 Hz.

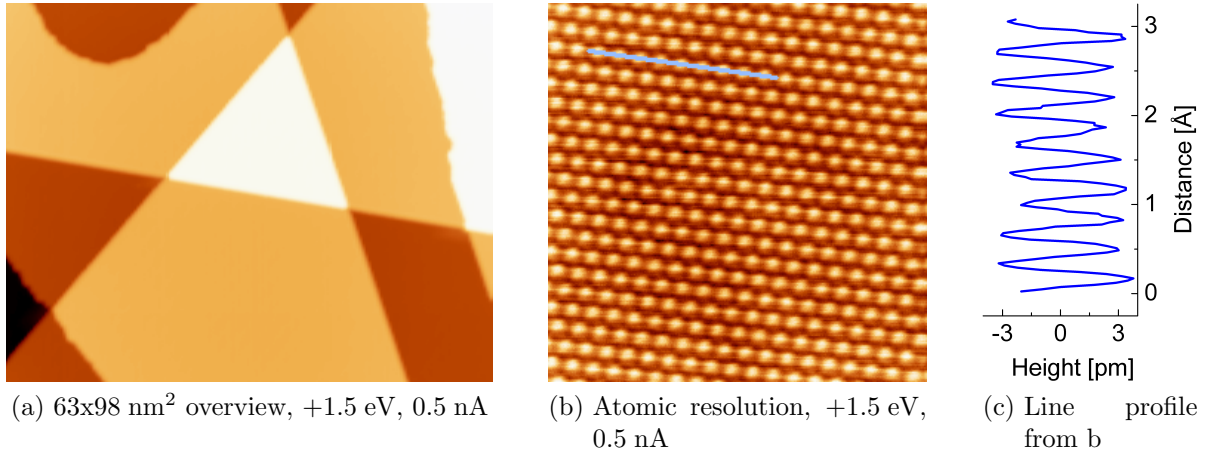


Figure 3.11: 500 monolayer Pb on Cu(111) at 4.2 K. All data is unprocessed except a plane subtraction.

possible reason would be a hot tip of around 12 K (see equation 3.4 and figure 3.10). It would result in a similar observation. But the temperature was stable at 4.2 K. Thermal problems via radiation etc. could be excluded. Finally the group of A. Heinrich in IBM Almaden gave a promising hint: Radio frequency noise. The problem is well known in the superconductor's community [89, 92] but is still underestimated in many STM groups approaching  $\mu\text{eV}$  resolved spectroscopy. As a result of the consultancy from IBM the radio frequency filtering was checked carefully and the filters improved.

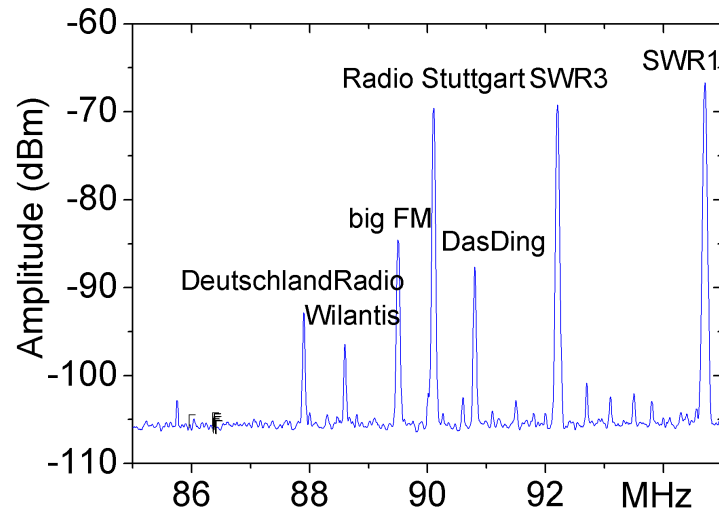


Figure 3.12: FFT of the radio signal coming **out** of the cryostat (bias feedthrough) when the current feedthrough was still floating.

These filters existed already at the cryostat for all the feedthroughs (bias, current, z and all multipin feedthroughs). They consist of an all metal housing with an separation wall<sup>32</sup> with  $\pi$  & C filters<sup>33</sup> in the middle and an optional resistance at the air side of the housing [93–95]. The housing for the filter was changed from an aluminum die-cast case sealed with copper foil to a fully soldered tinfoil box. The grounding cables for the filter boxes were reinforced to 16 mm<sup>2</sup>, soldered instead of screwed on the filters and directly connected to the central grounding point of the chamber. As a result the bias noise improved slightly but the broad gap survived unimpressed by all the changes.

So far the performance of the filters was checked with an oscilloscope. The electronic signals after the filters are clean. But nobody ever checked what comes **out** of the cryostat. To everybody's surprise one could find all the radio frequency signals at the bias connection of the cryostat: Cell phone frequencies (0.9 and 1.8 GHz as well as radio-broadcasting around 100 MHz (see figure 3.12) could be found.

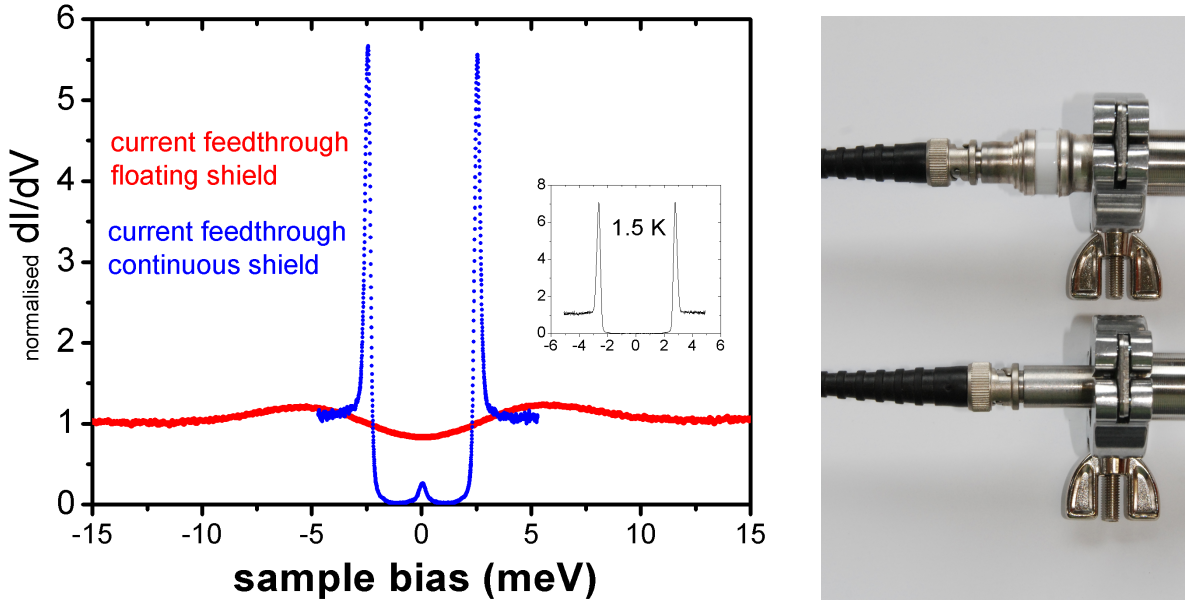


Figure 3.13:  $dI/dV$  with a Pb tip on Pb(111) at 4.20 K ( $V_{mod} = 50 \mu\text{eV}$ ) with floating (red, upper inset) and grounded (blue, lower inset) shield for the current feedthrough. The peak in the middle results from  $\Delta_1 - \Delta_2$  what is at zero for equal materials in SS junctions. It disappears at lower temperatures (see inset).

The reason turned out to be the floating shield feedthroughs<sup>34</sup> for bias, z and current

<sup>32</sup>Normal double sided PCB board was used.

<sup>33</sup>EMI/RFI surface mount  $\pi$  & C filters, 470x series, Tusonix, Tucson, USA. Typical losses are 15/55/70 dB at 10/100/1000 MHz.

<sup>34</sup>120XBF016-1, Trinos Vakuum-Systeme GmbH, Göttingen, Germany

. These ceramic rings could be sealed with conductive aluminum tape<sup>35</sup> and some surrounding copper sleeve. Good grounding of the aluminum tape with the copper is crucial. Figure 3.13 proves the effectiveness of this provisional solution until the next opening of the cryostat when the feedthroughs could be exchange by grounded shield ones.

### 3.5 Approach control and sample transfer

To exchange the sample in the STM inside the cryostat it is necessary to withdraw the tip a few mm. This avoids unintended tip crashes while pressing down the sample with the vertical manipulator when opening the bayonet lock. Since any direct observation e.g. with an optical microscope is impossible another way to control the approach is needed. Capacitive coupling provides the required precision and can be implemented by the lock-in amplifier.

The bias at the sample is modulated in the same way as for STS. The tip takes up the alternating electrical field depending on the distance. This scenario can be explained by a simple capacitor model where the tip and sample represent the two electrodes. The alternating current through a capacitor is defined as

$$i = \frac{du}{dt}C \quad (3.6)$$

with the capacitance in vacuum determined by the area and distance between the electrodes

$$C = \varepsilon_0 \frac{\oint_A \vec{D} d\vec{A}}{\int_S \vec{E} d\vec{s}} \quad (3.7)$$

Given a constant area the current is indirectly proportional to the distance in the first approximation (with a constant offset due to cable crosstalk etc.).

Each sample has its own value for the lock-in signal mainly depending on the height of the single crystal inside the sample holder for the same lock-in parameters. Once this value is known (46.0 in the example in figure 3.14) the proximity of the surface (43.0) can be approached extremely fast and reliably. Tunneling is reached then usually within a few hundred controlled steps in less than 3 min.

The capacitive coupling can be used for the sample transfer from and in the STM,

---

<sup>35</sup>AT521, Advance Tapes, Leicester, UK

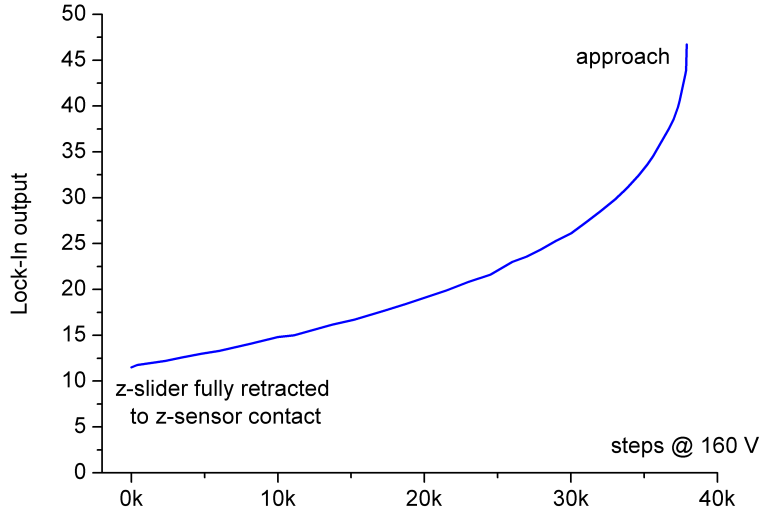


Figure 3.14: Lock-In signal for the approach from the fully withdrawn state to the metal surface; settings: 10 mV osc., 10 mV sens., 300 ms time constant,  $-135^\circ$  phase, 840 Hz, 7.1 K, 160 V sawtooth piezo excitation

too. Without sample the lock-in value drops from around 10 (tip fully retracted) to 6 indicating a proper hand over from the STM to the vertical manipulator and vice versa. This is extremely useful since the sample transfer posed many problems. G. Wittich changed the sample locking mechanism from a screw type to a bayonet ( $60^\circ$  rotation from open to close) before he left. This very good idea (see [67] page 34/figure 3.17) needed some improvements:

- The sample holder has to be polished. All sharp edges in both directions (in and out) need to be rounded ( $r > 1$  mm). Otherwise the sample blocks in the bayonet and can not be taken out from the STM anymore and the cryostat has to be opened for sample transfer.
- The bayonet arms at the sampleholder have to be considerably thinner than the bayonet openings in the STM otherwise the cryostat has to be opened.
- The CuBe springs in the bayonet have to be bent in way that they do not wrap up when closing the bayonet.
- Initially the rotor was able to perform a  $180^\circ$  rotation, turning the sample surface to the tip (down) or up. Unfortunately, the rotor position can not be determined exactly, the only indication were the two final contacts. For a controlled sample transfer the central pin of the sampleholder needs to be exactly vertically aligned.

As a consequence the rotor motion was limited to a few degrees to have the sample central pin always well aligned for the transfer. This still offers the possibility to change the tunnelling area on the sample macroscopically which is necessary since there is no additional xy coarse motor. Otherwise the central pin can break during the transfer.

- Any force during the sample transfer has to be avoided. The stepper motor that drives a worm gear for the vertical manipulator can apply too much force on the STM in particular on the rotor leaf spring that tends to brake.

### 3.6 Transfer chamber

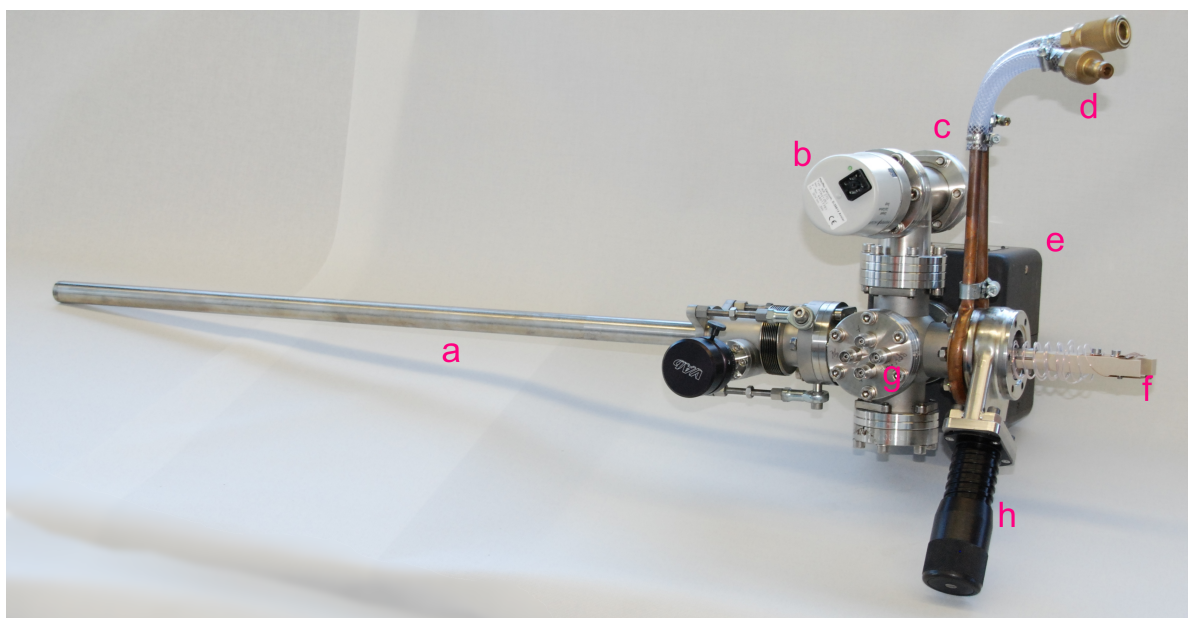


Figure 3.15: Transfer chamber for UHV sample transfer. **a** gear rack (Zahnstange) **b** cold cathode **c** hydrogen getter pump **d** water cooling **e** ion getter pump **f** manipulator head with self retracting CuBe cables to **g** BNC feedthroughs **h** UHV gate valve

The subK STM is a highly specialized machine for low temperature STM and STS measurements. In order to use a big share of the machine time for measurements it is not recommended to try to learn new preparation methods or attach complicated devices to the main chamber.

To enhance the possibilities of the system a portable UHV transport chamber has been built. The main objective was to prepare surfaces with large non-evaporable molecules



in the electro spray ion beam deposition lab(ESI)[96, 97] in the 4th floor of the institute and to bring them to the 6th floor in the subK STM. Apart from that the transfer head can be exchanged and fitted to any other system. So a versatile vacuum suitcase for sample transport from the ESI to other labs has been constructed.

The sampleholders of the two systems are not compatible. Thus, a design that does not require any handover in the ESI chamber has been chosen. Standard surface preparation can be done in the subK STM preparation chamber. Then the whole sample holder will be put in the transfer head. The gear rack (**a** in figure 3.15) is retracted, the chamber closed, unmounted from the STM chamber and moved to the ESI chamber. In the ESI lab the gear rack with the sample will be extended and the ion beam aligned to the sample. After the deposition the sample can be brought to the subK STM without breaking the vacuum.

The transport chamber is similar to the ones described by Firpo[98] and S. Olthoff[99]. The main components are as shown in figure 3.15:

- a standard DN CF40 double cross as central part, one flange water coolable via a copper tube with heat sink paste
- VaB 700 mm travel length gear rack (ZT-40-700J)
- home-built PEEK<sup>36</sup> manipulator head with electrical contacts to the sample (via the thermocouple contacts) and to a 5 mm aperture in front of the sample.
- two home-built copper-beryllium extendable spiral wires with PTFE insulation<sup>37</sup>
- 4-fold coaxial feedthrough
- VAT Mini-UHV gate valve with Viton<sup>38</sup> sealing
- Pfeiffer cold cathode IKR-270
- Saes getters SORB-AC hydrogen and active gas getter pump
- Varian StarCell VacIon20 ion pump
- MiniVac ion pump controller with home-built battery driven power supply (not shown in figure 3.15)

---

<sup>36</sup>polyetheretherketone (PEEK) has been chosen to avoid short circuits. It is bakeable up to 250°C.

<sup>37</sup>The idea with the spiral cables came from M. Moreno, UA Madrid, Spain

<sup>38</sup>250°C bakable

All parts are standard parts and the whole chamber is fully bakeable up to 250°C. After baking to 180°C and degasing of the hydrogen getter (21 V, 2 h) pressures of  $1 \cdot 10^{-11}$  mbar have been reached.

In both systems the ESI and the subK there are buffer chambers with small turbo pumps. In the case of the ESI good vacuum is required since the deposition takes a couple of hours. While baking the buffer chamber the transfer chamber is water cooled at the bottom flange and air cooled with fans (max.  $3.5 \cdot 10^{-11}$  mbar). After the bake the turbo pump can be closed and the buffer chamber is pumped via the main ESI chamber. This leads to better vacuum in the low  $10^{-10}$  mbar range.

In the subK an additional home-built LN<sub>2</sub> cryo trap on a CF40 flange helps to reduce the pressure by half an order of magnitude. Baking is here not necessary. The handover takes less than a minute in the  $10^{-9}$  mbar range.

As an example the spin transition molecule  $[Fe(bbp)_2]^{2+}[100]$  has been deposited without the  $BF_4^-$  counterions from its solvent acetonitrile on a clean nanomesh free of debris (see chapter 4).

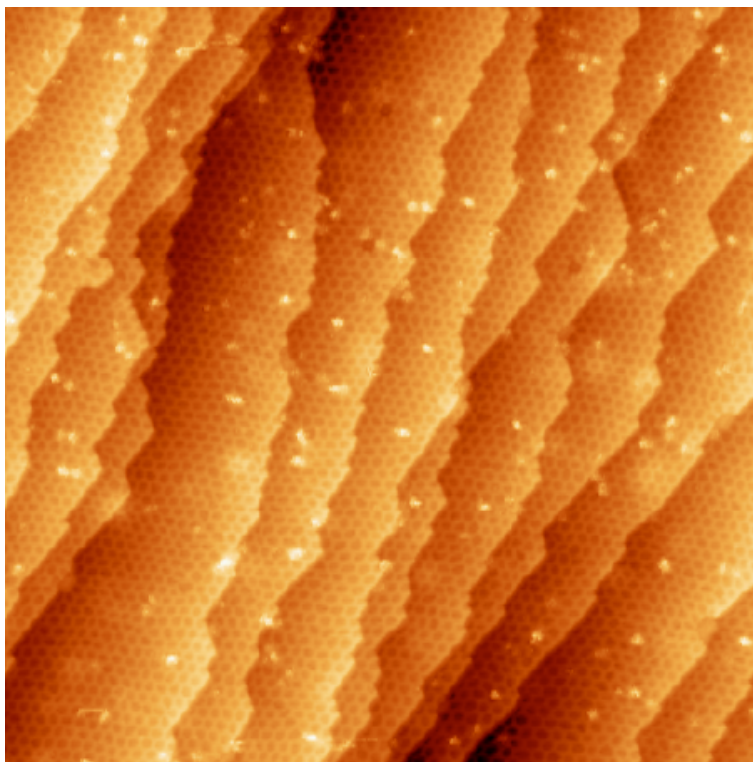


Figure 3.16:  $197 \times 197 \text{ nm}^2$  STM topography of the hBN/Rh(111) after 150 min deposition of  $[Fe(bbp)_2]^{2+}$  at 4 pA ion beam; sample bias 1.00 V,  $1.7 \cdot 10^{-11}$  A tunneling current

### 3.7 Possible future improvements

Certainly there are many ideas for future improvements of the system:

- Use only non-ferromagnetic materials for all parts close to the STM: feedthroughs, wires, springs, screws etc.
- Remove the shapal STM body and use an all bronze STM body for better thermal anchoring.
- Widen the capillary and run the cycle with more  $^3\text{He}$ .
- Replace the outer radiation shields with polished gold plated copper.
- Implement a planar tunnel junction (Nb-I-Nb) close to the sample as RF detector.
- Decouple the  $^3\text{He}$  pumping lines like it has been done for the  $^4\text{He}$  pumping lines for continuous mode and move all controls and valves for the cycle from the fifth to the sixth floor.
- Add a liquid helium cryo trap to avoid clogging of the capillary.

To summarize, the system achieved sub Kelvin performance. The temperature decreased from 2.7 K to 0.8 K. The vibrational noise could be reduced from 60 pm to <1 pm and - most important - the energy resolution improved from 10 meV to less than 200  $\mu\text{eV}$ .



## 4 The boron nitride nanomesh

Boron nitride is a wide band gap material [101, 102] with some striking similarities to carbon[103]. Boron is one element to the left of carbon in the periodic table. It has one electron less and is significantly less electronegative. Nitrogen on the right has one electron more and a higher electronegativity than carbon. They are isoelectronic with at least local dipole moments in the boron nitride where the bonding contains a certain ionic component. This ionicity drives the BN to be insulating with a band gap of  $\sim 5$  eV. Carbon exists in several  $sp^2$  or  $sp^3$  hybridized allotropes including graphite, diamond, fullerenes, nanotubes and graphene. Similar structures are known for boron nitride: The bulk material exists mainly in the hexagonal ( $sp^2$ ) and the cubic ( $sp^3$ ) modification.

The h-BN is similar to graphite ("white graphite"). It consists of layers that are comparatively weakly linked and that can move against each other. H-BN bulk material is used as a lubricant e.g. at high temperatures in oxidizing atmospheres where carbon can not be used. Since there are no water molecules involved in the gliding process it can be used in vacuum and space applications.

The cubic boron nitride is a diamond-like polymorph. It has a high (phononic) thermal conductivity and is very hard although softer than diamond. It is used as an abrasive in grinding and cutting tools for steel because BN is insoluble in iron (in contrary to diamond that forms carbides)[104].

Beside the bulk materials there are boron nitride fullerenes[105, 106] and nanotubes[107] that have been studied over the last 15 years. The graphene-like analog is a single (surface supported) layer of  $sp^2$  bonded boron nitride[108, 109].

The first scientific reports go back to the mid 1990s. At that time it was believed to be a potential candidate for ultralarge scale integration (ULSI) by IBM and Siemens[113]. The group of Nagashima in Japan investigated both graphene (they called it monolayer graphite)[114, 115] and boron nitride monolayers [116–118] as well as graphene on hBN/Ni(111) multilayer systems[119–121].

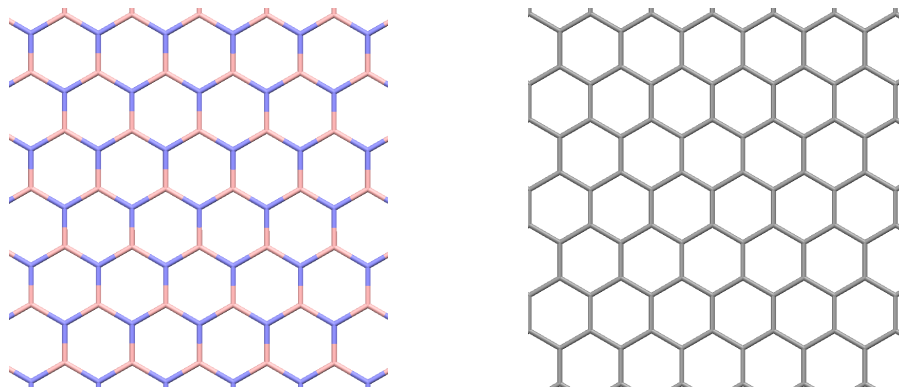


Figure 4.1: h-BN on the left and graphene structure (right) [110–112]

After this initial interest it took a few years to rediscover the boron nitride nanomesh in the group of Osterwalder in Zürich mainly by Auwärter [122–124] and finally Corso[21]. This work triggered many experimental and theoretical works what will be shown later.

## 4.1 Advantages of the nanomesh

But why is the nanomesh so important? What are its advantages compared to similar systems?

The first answer is simple: because it acts as a **template** on the nanoscale [125–127]. The periodicity of the h-BN cavities on Rh(111) is 3.2 nm providing a desired templating effect for a bottom up approach. Many adsorbates like  $C_{60}$ [21] or Co-clusters[128] are known to be trapped in the cavities of the nanomesh. In addition it is very inert and can stay several days in UHV without any contamination. It also survives high temperatures up to 1000°C.

Secondly it is **insulating**. Insulators are crucial in electronics in general. One initial idea was to use it as a replacement for the gate oxide in transistors. But the low dielectric constant of  $\approx 4$  (similar to  $SiO_2$ ) cannot compete against modern Hf-based high- $\kappa$  materials ( $\kappa \approx 25$ ). Nevertheless the boron nitride nanomesh could find its place in the investigation of adsorbates with STM. In STM conducting substrates usually metals are required for the tunneling current. To put ultrathin insulators on the substrate is a widely used technique[129]. Besides salts like KCl, NaCl or  $CaF_2$ [9–11, 130–132] oxides( $Al_2O_3$ ,  $MgO$ )[20, 133–140] and nitrides[141] are often used. The single BN layer provides a reliable mean to decouple the adsorbate electronically from the metal surface.

And finally it is **easy to prepare** (see next section) - by far easier than most other insulators that often form patches or islands of different heights. The boron nitride nanomesh grows defect free monolayers over wide ranges reproducibly and is very inert. It is stable in aqueous solutions and under ambient conditions [142–144].

## 4.2 Preparation of the nanomesh

The sample preparation is done via a chemical vapor deposition (CVD) process: the thermal, transition metal-catalyzed decomposition of borazine ( $\text{HBNH}_3$ ) precursor gas.

First, one obtains a clean Rh(111) surface from a rhodium single crystal<sup>1</sup> by successive cycles of  $\text{Ar}^+$  sputtering (1.0 kV  $\text{Ar}^+$ -ion energy for 30 min and annealing (1070 K for 3 min) in UHV. A typical example is shown in figure 4.2. For new crystals the established conditions may be varied to higher sputter energies (up to 2.5 kV), hot sputtering at 1100 K and stepwise annealing with 10 K lower temperatures for each consecutive cycle. For high sputter energies above 1.5 kV subsurface argon bubbles appear[145]. They are typically 10 nm wide and 3 Å high and disappear in the last preparation cycle at lower sputter energies. Alternatively evaporated Rh can be used as substrate[146].

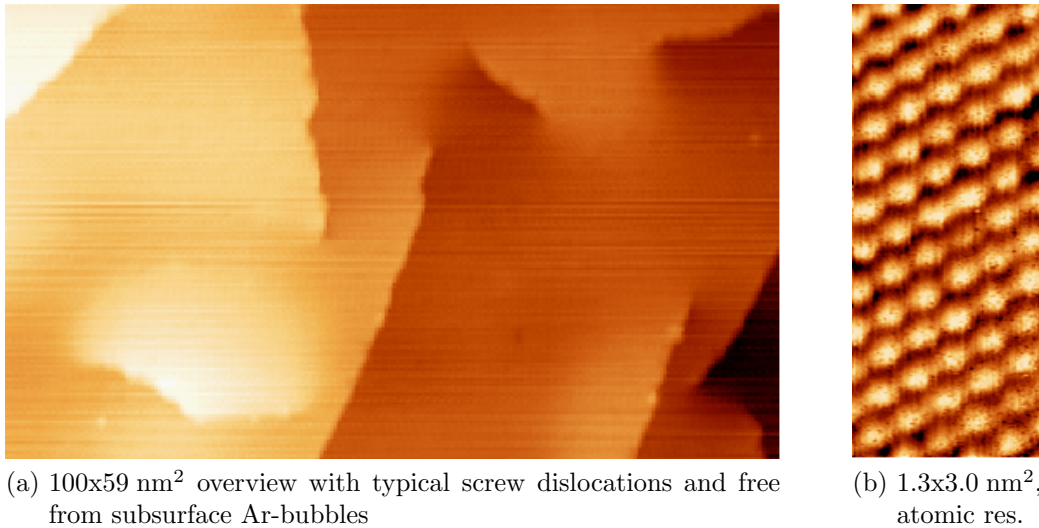
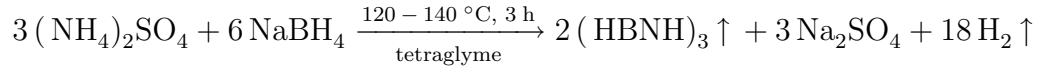


Figure 4.2: STM topographies of the general morphology of the clean Rh(111) surface, lattice constant 2.69 Å

<sup>1</sup>Rh(111) single crystal from Mateck GmbH, Jülich, Germany; miscut  $< 0.1^\circ$

The borazine precursor is the BN analog to the Kekulé structure of benzene: A sixfold ring with alternating boron and nitrogen atoms saturated with hydrogen. It is a colorless liquid with a slightly aromatic smell. Under inert gas atmosphere or in its own vapor pressure (250 mbar at room temperature) it is stable but slowly decomposes under hydrogen release[147] and the formation of small precipitates that contain BN and/or polymerized borazine. To avoid the decomposition the borazine should be kept cold and dark[124]. The precipitates do not disturb the CVD process and can be removed by condensation into a clean container.

Borazine can be synthesized from sodium borohydride and ammonium sulfate in tetraglyme solution[148, 149]:



The sodium borohydride is continuously added to the tetraglyme/ $(\text{NH}_4)_2\text{SO}_4$  solution. The borazine (boiling point = 55 °C, melting point = -58 °C) is condensed in one of three consecutive  $\text{LN}_2$  cooling traps and the hydrogen has to be pumped always below 5 mbar. The reaction yield varies between 30 to 70 % (typically 20 g per batch).

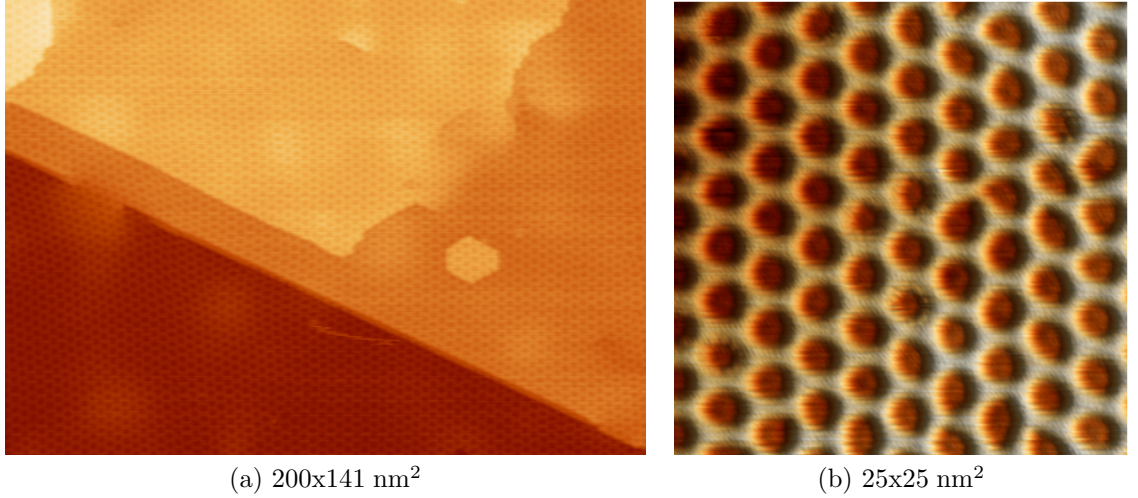
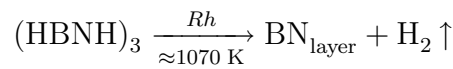


Figure 4.3: STM topographies of the nanomesh on Rh(111) illustrate the long range order as well as the 2 nm cavities and the 3.2 nm periodicity

Finally the Rh(111) is exposed to the borazine via a leak valve while keeping it at 1070 K.





The Rh acts at this juncture as a catalyst[150]. The minimum temperature required to crack the BN-bonds is approximately 980 K but above 1050 K the nucleation site density is lower. So high temperature and low flux during deposition allow best film qualities[151].

Doses of 40 L of borazine already form a complete BN layer ( $1 \text{ L} = 10^{-6} \text{ Torr} \cdot \text{s}$ ). By decreasing this dose, partial coverages become accessible. The fraction of the surface covered by the nanomesh is approximately the dose used divided by 40 L. Even for doses as low as 5 L, the coherent regions covered by the BN nanomesh are always quite large ( $>1 \mu\text{m}^2$ ).

Independent of the dose used only monolayers form for temperatures around 1100 K. In order to achieve multilayer growth temperatures of 1500 – 2300 K would be required[152]. This provides a very reliable procedure for the monolayer film growth.

Since borazine is comparably costly, researchers were looking for alternatives with cheaper precursors. One is the evaporation of boron in sub-ML amounts and ensuing thermal decomposition of  $\text{NH}_3$ . Or, another way: simultaneous dosing of  $\text{B}_2\text{H}_6$  and  $\text{N}_2\text{H}_4$  to hot transition metal surfaces[153].

### 4.3 The partial double layer model or how a Science paper can mislead

From the very early beginning of the investigations in h-BN layers on metals it never came into question that a continuous single layer of hexagonal boron nitride covers the surface [115, 116, 154, 155]. In 2004 Corso and Auwärter et al. from the group of J. Osterwalder in Zürich published a Science paper [21] claiming a double layer model on Rh(111). The group had already published quite a few papers on the topic [122–124, 156, 157]. They claimed that there are two layers of a *nanomesh*. The upper layer was supposed to be in contact with the rhodium at the hole positions of the lower layer. The STM images looked really convincing and supported the double layer model. I searched hard for the double layers and observed similar features from time to time. Insulating layers with true holes really exist[158]. Fortunately Prof. Osterwalder told that it turned out to be merely a double tip. The double layer model and the original STM image are shown in figure 4.4.

Anyway the idea of the double layer model triggered many experimental and some

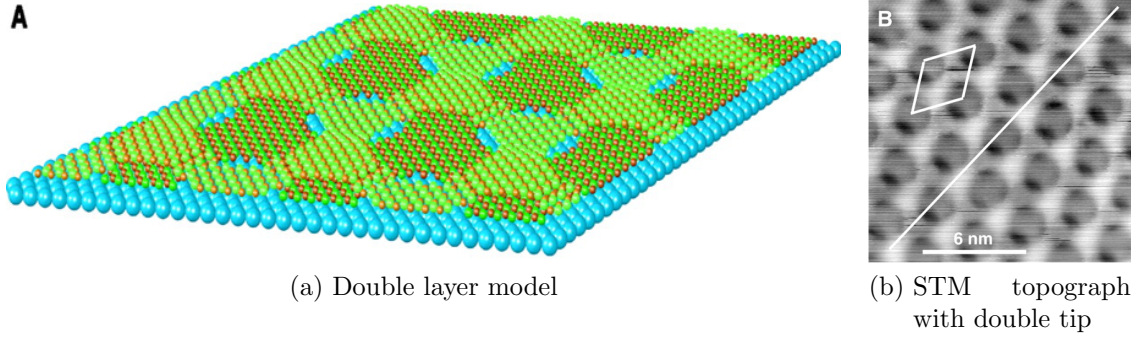


Figure 4.4: Model and STM topograph of the boron nitride double layer model proposed by Corso et al., both images reproduced from [21]

theoretical work mainly by Laskowski et al. [159, 160] to reveal the true structure. It took a while to convince everybody in the community that the single layer model is true for Rh(111), too. Nowadays the single layer model is generally accepted.

Merely the word *nanomesh* survived - although wrong - and is still used by many scientists because of its simplicity.

## 4.4 Structure of the nanomesh (on different substrates)

H-BN single layers form on a variety of transition metal substrates. Most studies have been done on nickel, rhodium and platinum that are 3d, 4d and 5d metals, respectively. A survey of studies containing experimental results on different surfaces is given in the following list. There are no reports about gold or cobalt as substrates yet.

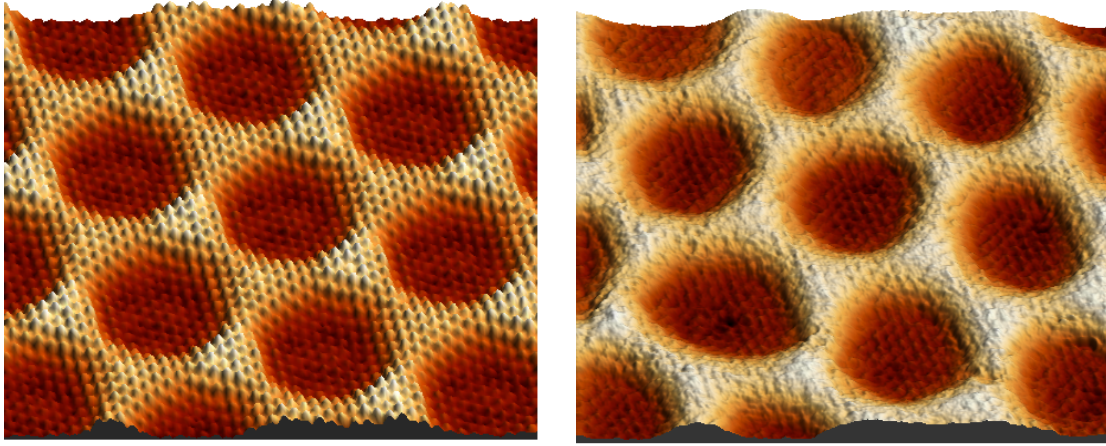
**3d** Cr(110)[161], Ni(100)[154], Ni(110)[162], Ni(111)[115–118, 122–124, 156, 163–166], Cu(111)[164]

**4d** Mo(110)[167], Ru(0001)[108, 155, 168–170], Rh(111)[21, 128, 142–144, 170–172], Pd(110)[173], Pd(111)[116, 174]

**5d** Re(0001)[175], Ir(111)[170], Pt(111)[116, 155, 170, 172, 176]

The h-BN grows commensurately and flat on those substrates with low lattice mismatch and hexagonal symmetry like cobalt<sup>2</sup>, nickel or copper (111) surfaces regardless of the chemical interaction. On the noble metal surfaces despite the lattice mismatch flat

<sup>2</sup>There are only theoretical predictions, no experimental proofs yet.



(a) Theoretical STM image, data calculated by Laskowski and Blaha[160] at  $-2$  eV,  $2$  Å above the surface  
 (b) Measured STM topography at  $0.12$  eV and  $1$  nA at  $4.2$  K

Figure 4.5: Comparison of calculated[160] and measured atomic resolution images of the nanomesh proving the corrugated single layer model. Note the abrupt change within one atom from cavity to ridge position that explain the split BN- $\sigma$  bands observed in UPS[21].

layers form (gold, platinum, silver). The interaction is too weak to form a corrugated layer. If the interaction gets stronger the h-BN layers tend to have a higher corrugation. The pits of the nanomesh become more pronounced in the row Ni(111)(flat) - Pt(111) - Ir(111) - Rh(111) - Ru(0001)(wide cavities)[170, 172].

To be more precise: The observed geometry on Rh(111) is the result of the competition of repulsive and attractive forces in the BN-metal substrate interface and the elastic strain in the BN and not simply the lattice mismatch. The lattice constant of the basal plane of h-BN is  $2.5$  Å for rhodium in the densely packed fcc-plane  $2.69$  Å ( $a_{\langle 110 \rangle} = a_{Rh}/\sqrt{2}$ ). This considerable mismatch leads to a superstructure of  $13 \times 13$  BN on  $12 \times 12$  Rh ( $13 \times 2.5$  Å =  $32.5$  Å  $\approx$   $12 \times 2.69$  Å =  $32.28$  Å). Now it becomes obvious that not all nitrogen or boron atoms can be in the same environment with respect to the rhodium atoms.

Three main positions can be distinguished for the boron and nitrogen atoms: on top of a rhodium atom, in a fcc-hollow or a hcp-hollow site[157]. According to reference [159] nitrogen is always repelled and boron always attracted. The repulsion for nitrogen is weakest on top of a rhodium atom. This is where the cavities are formed and the strongest hybridisation of the rhodium  $d_{z^2}$  orbitals and the BN  $p_z$  orbitals occurs. The

two other positions of the nitrogen (fcc, hcp) make out the ridges. The calculated equilibrium nitrogen-rhodium distances vary from  $2.18 - 2.72 \text{ \AA}$  depending on the position inside the unit cell.

The change from small to large N-Rh distances - what is observed as the nanomesh structure - happens very abrupt within one or two neighboring atoms (see figure 4.5). Most of the nitrogen atoms are either far or close to the rhodium what explains both the  $\sigma$ -band splitting seen in UPS[21] and the misleading tip effects with the partial double layer model.

Furthermore, the boron atoms (stable in fcc(cavity) or hcp-hollow sites) are always closer to the surface than the neighboring nitrogen atoms ( $2.04$  and  $2.18 \text{ \AA}$  for proximate atoms in the cavity). Most probably only the nitrogen atoms are visible in STM. The topmost rhodium layer relaxes with a corrugation of  $0.1 \text{ \AA}$  [177]. The symmetry of the structure seems to be six-fold at a first glance. If one looks in more detail it is not even three-fold but only a mirror-plane remains [159].

## 4.5 Apparent height

The apparent height of the h-BN on Rh(111) in STM is strongly bias dependent. The appearance of the cavities and ridges differ and do not correspond to the calculated values. This is partially due to different tips but can not explain the strong bias dependence. The comparison to calculated projected density of states by Laskowski et al. [160, 178, 179] explains many of the observed features. Figure 4.6 provides a qualitative summary of the topic. For more details concerning the DFT calculations see [178].<sup>3</sup>

The apparent height of the nanomesh is shown at the top of figure 4.6. The insets are STM topographies of the nanomesh to pristine substrate transition at  $0.2 \text{ nA}$  and indicated bias. The Rh(111) substrate height is set to  $0 \text{ \AA}$  and the cyan curve shows the relative height of the cavity of the nanomesh, magenta represents the ridges that surround the cavities.

The ridges appear around and below  $E_F$  as high as the substrate ( $+0 \text{ \AA}$ ). Beyond that region they appear higher. In a good approximation this corresponds to the DOS of the free standing single layer h-BN. The band gap is indicated by the magenta shaded rectangle. Inside the gap the electrons tunnel directly between tip and the metal substrate. Thus, the ridges are invisible. Only for tunneling outside the gap B and N

---

<sup>3</sup>Note that the DOS for the N and B  $d_z$  states are multiplied by 3 in the references!

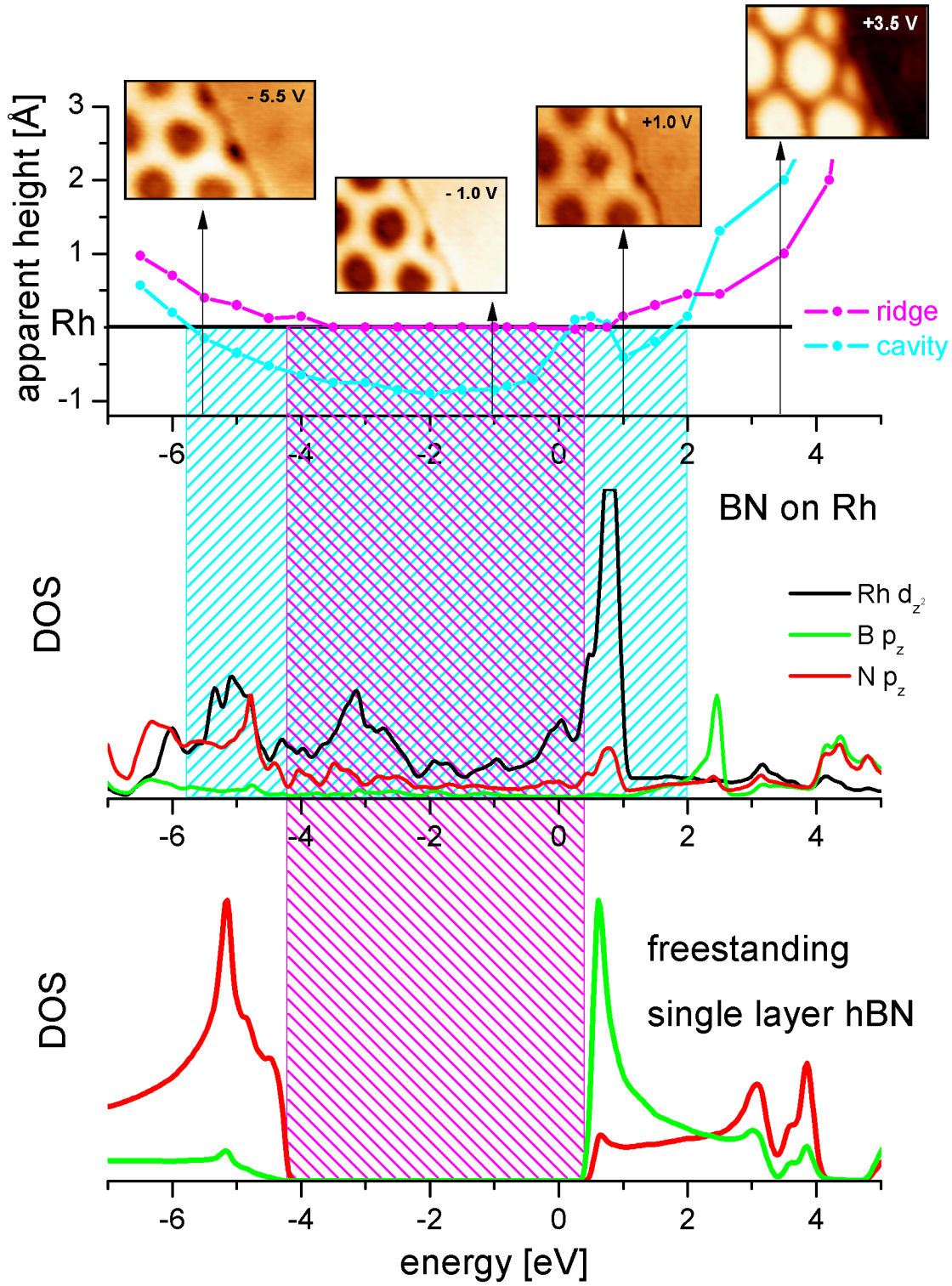


Figure 4.6: Comparison of the apparent height of the h-BN/Rh(111) (top) with the density of states calculated by Laskowski et al. [178] (middle and bottom). The insets are STM topographies of the nanomesh to pristine substrate transition at 0.2 nA and indicated bias. The Rh(111) substrate height is set to 0 Å and the cyan curve shows the relative height of the cavity of the nanomesh, magenta represents the ridges that surround the cavities. For more explanation see text.

$d_z$  states become accessible and the ridges appear higher than the substrate. Note, that this is only a very simple approximation diverting from the calculations by Laskowski et al. [178]. They give detailed DOS even for the two different ridge configurations (N-hcp, B-top and N-fcc, B-hcp) while here only the lower parts of the ridges are considered (N-fcc, B-hcp) for the apparent height curve.

This approximation does not hold for the cavities where the substrate and BN states strongly hybridise. Outside the band gap the BN states are accessible (similar to the previous paragraph) and the cavity regions appear higher than the substrate. Inside the band gap the BN appears *lower* than the substrate. The strong interaction shields the Rh  $d_{z^2}$  states except just above  $E_F$  (see also Figs. 3d, 11middle of [178]). This is where the ridges and the cavities differ from each other in the. Interestingly the cavities appear higher than the ridges above 2.5 eV (see inset at +3.5 eV).

## 4.6 Electronic properties/STS

The measured apparent heights indicate that at low bias the tunneling process is taking place through the BN nanomesh directly to the metal surface. This gives a first estimation of the band gap with a value  $\sim 5$  eV for the ridges and  $\sim 7$  eV for the cavities.

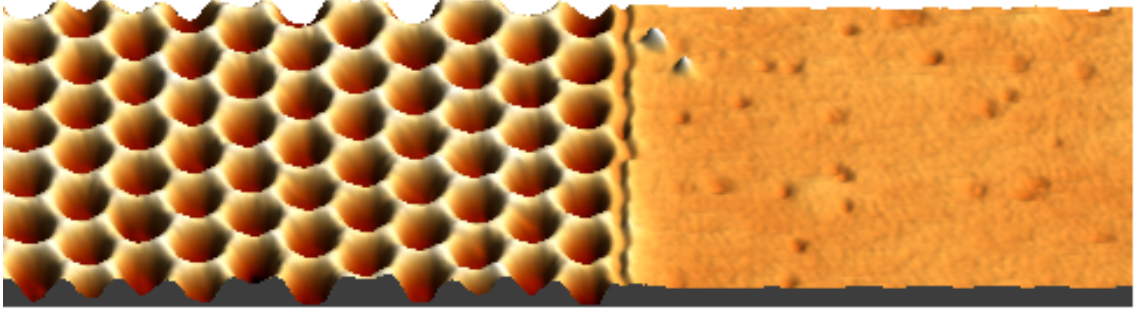


Figure 4.7: Partial coverage as a playground for scanning tunneling spectroscopy. Nanomesh on the left and pristine Rh(111) on the right.  $60 \times 20 \text{ nm}^2$ ,  $-1 \text{ eV}$ ,  $0.2 \text{ nA}$ .

By covering the rhodium surface only partially with the nanomesh one can probe the electronic properties of the h-BN monolayer and compare it with the pristine metal surface. Here 20 L of borazine were used to get a  $\sim 50 \%$  coverage. Fig. 4.7 shows the coexistence of regions covered by the nanomesh and the clean rhodium regions. The interface of the two regions is very clear and abrupt and takes place in the middle of a



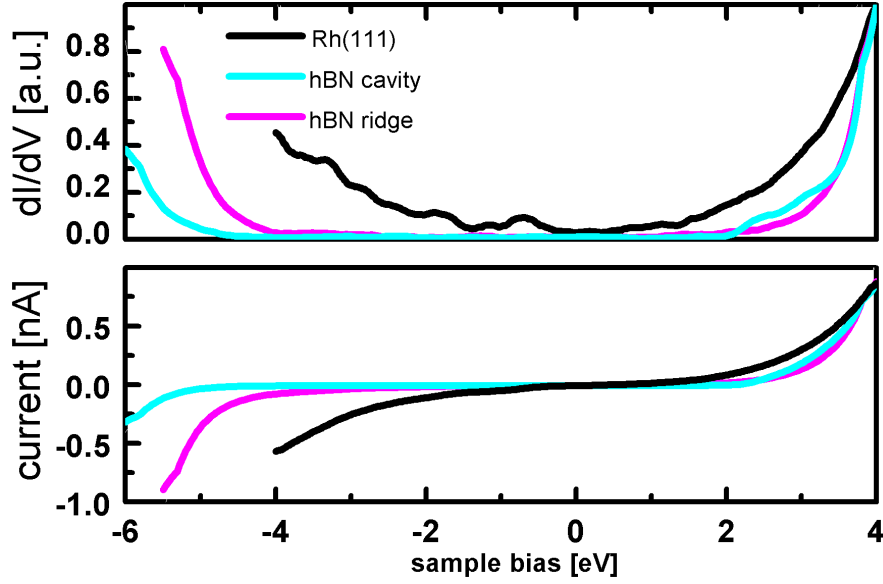


Figure 4.8: STS on the partial coverage nanomesh on Rh(111). UPS data[21] showed the splitting of the BN band in two components at -4.6 eV and -5.7 eV, which were associated with the parial double layer model. Real space resolved STS shows that the BN peak positions correspond to the energies where an appreciable increase of the local density of states can be observed for the ridges (low energy peak) and cavities (high energy peak), confirming that they can be attributed to these regions.

terrace while on other terraces the BN nanomesh growth is limited by a step edge or dislocation (not shown).

The insulating character is observed by means of STS on the nanomesh, which presents an electronic gap of 5 – 6 eV in the  $dI/dV$  - in clear contrast with the metallic behavior detected on the Rh(111) surface. This electronic gap is present on the entire nanomesh region, which proves that the nanomesh is indeed a continuous layer without real pores. This is also consistent with the atomically resolved STM images(see Fig. 4.5 on page 55).

The STS experiments were carried out at 4.2 K to extract the local electronic properties of the BN nanomesh. In order to obtain reliable STS data and to avoid tip artifacts, it is advantageous to have a reference for checking the STM tip configuration. Here the clean Rh(111) surface, which coexists with the BN nanomesh, can be used as such a reference and only tips showing a clear featureless metallic character were taken into consideration for the STS analysis.

The whole surface was mapped by means of differential conductance ( $dI/dV$ ) spectra measured with open feedback loop using a lock-in technique. STS data are always ac-

quired with initial tunneling parameters for which the nanomesh regions have a positive apparent height (see figure 4.6). The reproducibility of all spectra is checked by varying the initial tunneling current and hence the tip-sample distances and using microscopically different tips.

Both regions (cavities and ridges) show a marked wide band gap, which definitely discards the possibility of the existence of real pores and clearly demonstrates that the BN nanomesh is a continuous layer. Figure 4.8 shows STS curves acquired on the nanomesh and on the Rh(111) surface with exactly the same STM tip and using identical tunneling parameters before opening the feedback loop. The experiments revealed a clear decrease of the conductance at low biases for the nanomesh regions compared to the Rh(111) surface. From the  $dI/dV$  spectra shown in figure 4.8 band gaps of 5 eV for the ridges and of 6.5 eV for the cavities are obtained. These values are very reproducible for all tunneling conditions and are in very good agreement with the ones initially inferred from the apparent height measurements discussed above.

So one last question remains: Is the h-BN nanomesh **insulating**?

Depends on how to interpret the question. The free standing h-BN single layer (as well as the hexagonal bulk boron nitride) has a very clear band gap. So it can be called insulator without any doubt.

The transition metal supported single layer has a considerable adsorption-induced hybridisation between the metal's  $d_{z^2}$  and the h-BN  $p_z$  states within its band gap. This was calculated by Laskowski et al. and can be seen in the shielding of the rhodium  $d_{z^2}$  in the h-BN nanomesh cavities where the h-BN apparent height is lower than the Rh(111).

These gap states depend on the strength of the chemical interaction. For the cavities of the nanomesh on rhodium and even more pronounced on nickel the chemisorption is stronger than e.g. on platinum[180]. To call the single surface supported BN layer a classical insulator would probably go too far. More than one layer would be required. Anyway it acts as an effective decoupling layer that provides the possibility to study adsorbates **electronically decoupled** from the metal surface.



## 5 Cobalt clusters on h-BN

In order to test the decoupling capabilities of the h-BN nanomesh and to combine them with its templating effect, cobalt clusters were deposited using buffer layer assisted growth [181]. In this way, the nanomesh acts as a template selectively accommodating clusters of almost identical size on the cavities. With buffer layer assisted growth (BLAG) a highly ordered ensemble of Co clusters with a hexagonal 3.2 nm periodicity can be obtained on the BN nanomesh regions while a random distribution of Co clusters is found on the clean metal.

### 5.1 Buffer layer assisted growth

Though the growth of nanometer sized clusters has been possible since the past few decades it has always been a challenge to grow single isolated clusters of nanometer dimensions [182–184]. In addition the clusters should have a certain size distribution, in both height and diameter (aspect ratio) [185], and should be distributed over the complete surface and not gathering at defects or step edges.

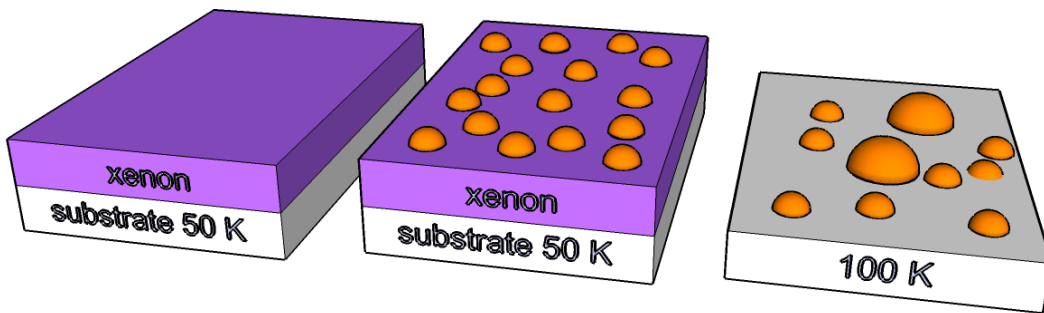


Figure 5.1: Schematic view of the buffer layer assisted growth. First xenon gas is adsorbed at the cold substrate. Then the metal is evaporated on the cold xenon buffer layer. In the final step the xenon is desorbed and the clusters sink on the surface.

There are several methods to grow clusters. For an introduction see the book of Milani and Ianotta [186]. Clusters can be grown directly on a substrate from evaporated materials or using molecular beam epitaxy. Furthermore they can be precipitated from solutions or formed in a micelle. The highest level of control provide cluster sources with quadrupole mass selection.

The experimental effort for buffer layer assisted growth is small compared to a sophisticated cluster source. It has been shown to be a method to grow isolated clusters independent of the substrate [187]. It avoids epitaxial growth that would depending on the substrate's lattice constant and symmetry lead to one of the three growth modes (Frank-van-der-Merwe, Stranski-Krastanow or Volmer-Weber). Wetting layers before island formation as seen for many Stranki-Krastanow systems (like Pb/Si(111)) do not occur. Buffer layer assisted growth avoids step decoration and does not leave traces from any agent, layer etc. from the preparation on the surface.

It was first described by Weaver and Waddill in 1989 [181, 187]. In contrast to soft landing of complete clusters on rare gas layers [188] the three steps of the process are the following as illustrated in figure 5.1:

1. The (clean) substrate is liquid helium cooled. Xenon gas is let into the UHV chamber via a leak valve where it adsorbs on the sample.
2. The desired metal can be evaporated on the xenon buffer layer and forms the cluster.
3. The sample needs to warm up to desorb the xenon buffer layer. The clusters sink on the surface.

The structure of the xenon buffer layer is temperature dependent. At very low temperatures of a few tens of Kelvin an amorphous xenon films forms. It orders according to the substrate at higher temperatures and desorbes depending on the layer thickness and the substrate interaction. Bulk xenon sublimates at 55 K.

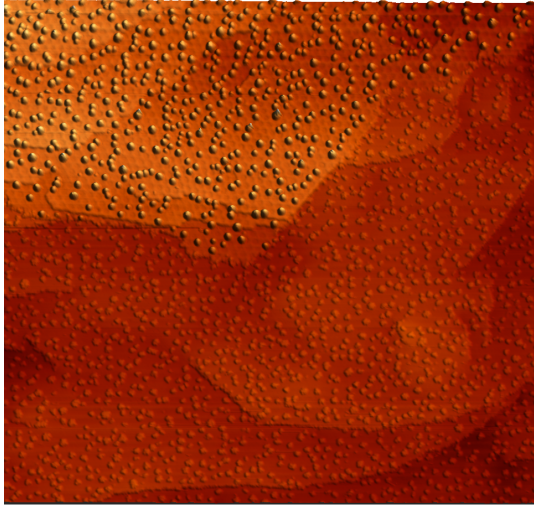
For the nanomesh a variable temperature photo emission study by Dil et al. [189] shows multilayer xenon below 63 K. Above 63 K monolayers remain for temperatures up to 72 K on the ridges and up to 82 K in the cavities. For the bare rhodium substrate there are no values in the literature. But there exist many studies on platinum, silver and many others [190–196]. On Ag(111) the second last and the last monolayer desorb at 62 K and 85 – 90 K respectively. On Pt(111) the last monolayer remains until 100 – 107 K due to higher binding energies. So in the Rh(111) case the desorption temperature should

be at least 100 K while the xenon around the cobalt clusters desorbs at correspondingly higher temperatures [197] leading to a soft landing process.

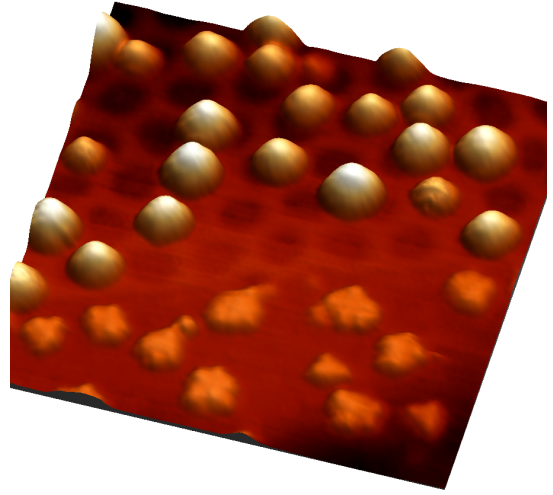
For the preparation of the BLAG the manipulator head can be cooled down to 37 K<sup>1</sup> while the type K thermocouple<sup>2</sup> inside the sampleholder shows 70 – 90 K. In any case multilayer growth of xenon on the nanomesh could be achieved indicated by a blueish to violet discoloration for high amounts of xenon (15000 L) although for the results in this chapter usually a dose of  $1 \cdot 10^{-7}$  mbar for 50 s (5 L) are used.

To tune the size distribution and cluster density there are besides post-depo annealing (that can lead to intercalation[169]) mainly two parameters: coverage and xenon layer thickness. Thicker xenon layers lead to bigger clusters with a wider size distribution. The reason for the bigger clusters on thicker xenon layers is not fully understood. It could be that the diffusion is enhanced or that the smaller clusters agglomerate during the buffer desorption process. A higher coverage leads to more clusters with a very narrow, mono-dispersed size distribution if low amounts of xenon were used.

The cluster size distribution and coverage are correlated. The density of clusters on the BN nanomesh can be controlled individually by the number of BLAG cycles. After one cycle with approximately two monolayers of xenon and 3 – 5 % of a monolayer of cobalt roughly one third of the cavities is occupied with a cluster (see figure 5.4a on page 66). Each consecutive cycle results in less additional filling. Filling factors up to 80 % could be achieved [128] (see figure 5.4b).



(a) 200x200 nm<sup>2</sup> overview shows uniform cluster distribution without step decoration. +1.5 eV, 1 nA.



(b) Cobalt clusters at the interface. They appear round and smooth, without facets on the nanomesh while they seem flat and irregular on the bare metal. +1.5 eV, 0.2 nA, 25x25 nm<sup>2</sup>.

Figure 5.2: STM topographs of cobalt clusters deposited on a partial coverage h-BN nanomesh (upper left in both images) and on the pristine rhodium substrate (bottom right).

## 5.2 STM topography

When depositing cobalt on the partially covered surface, the clusters can be found on the Rh(111) clean surface as well as on the BN nanomesh regions as shown in figure 5.2. While Co clusters on the BN layer appear nearly hemispherical or dome-shaped, they are flat and irregular on the pristine Rh(111) surface.

There are mainly three reasons why the clusters appear differently:

First of all, due to the large interfacial free energy the cobalt clusters flatten on the bare metal. Alloying can not be excluded but has never been observed for this system in STM.

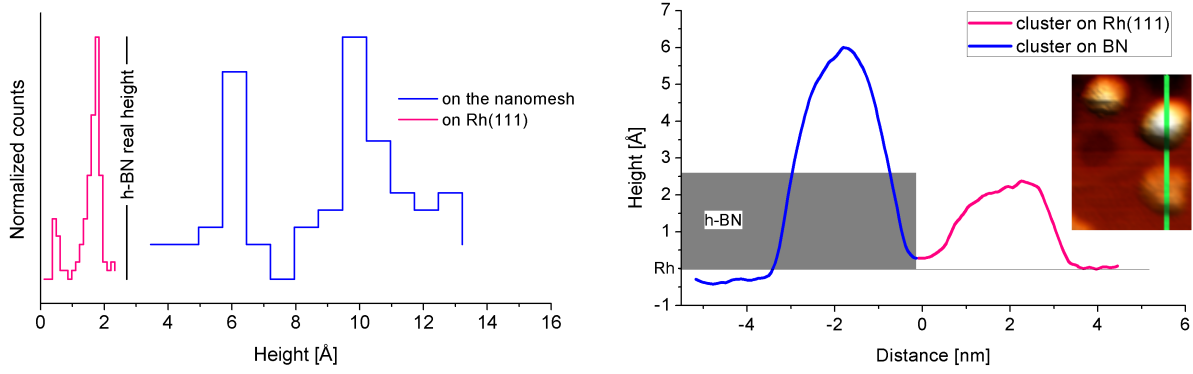
Second, according to the spherical jellium model [198–200] clusters up to a few hundreds or even thousand atoms can be seen as a core of positive ions with delocalized electrons around it<sup>3</sup>. These delocalised electron shells lead to a round shape in STM.

Third, the nanomesh appears lower than its real height for the bias used (see figure 4.6

<sup>1</sup>Measured with a Pt100 resistance thermometer.

<sup>2</sup>Type K thermocouples are rarely used for temperatures lower than 70 K although tables down to 4 K exist since the Seebeck coefficient is non-linear and drops with decreasing temperature.

<sup>3</sup>This leads for free clusters to magic sizes (2, 8, 20 etc.) with closed electronic shells.



- (a) Co cluster height distribution histograms on the Rh(111) (magenta) and on the nanomesh (blue). The bulk Co hcp lattice constants are 2.51 Å and 4.07 Å. On the rhodium the clusters appear between 1.5 and 2.0 Å high corresponding to one layer. On the nanomesh the apparent height has two peaks at 6 and 10 Å corresponding to one monolayer followed by another one or two hcp stacked layers.
- (b) Line profile of the nanomesh-pristine Rh(111) interface with two clusters. The nanomesh (very left in the profile, top in the inset) appears lower than the rhodium (very right in the profile, bottom of the inset). The cluster on the nanomesh has an apparent height of 6 Å the other one of ~2 Å.

Figure 5.3: Co cluster heights

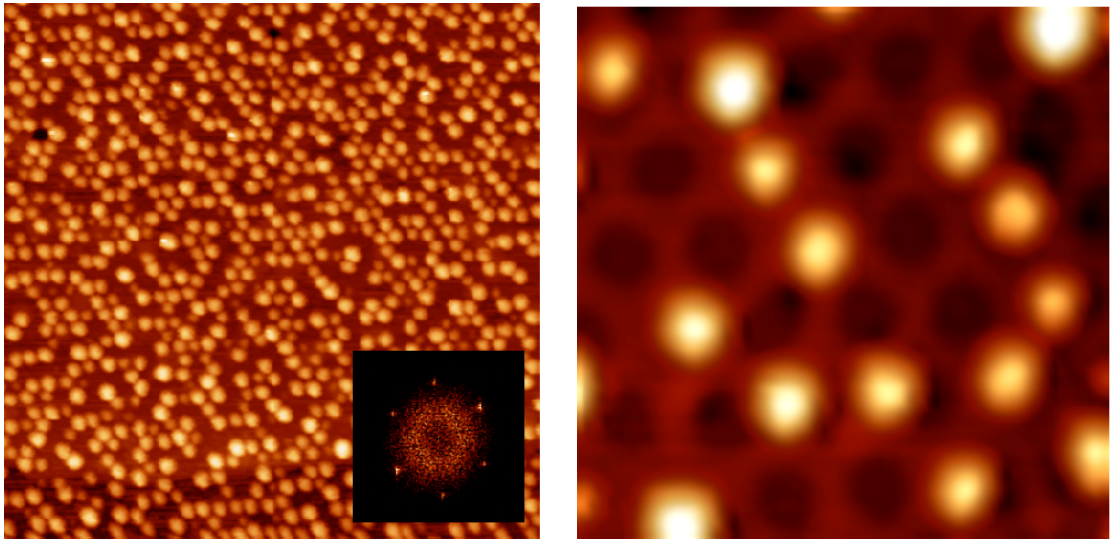
on page 57). On the cluster the tunneling from the nanomesh to the metal substrate is not determining the apparent height anymore. On the cluster one observes the full height of the cluster plus the nanomesh's apparent height while the surrounding nanomesh appears transparent and thus as high as the bare metal substrate or even lower. So the clusters on the nanomesh appear about the nanomesh's true height higher than they are.<sup>4</sup> Similar phenomena could be observed in other ultrathin decoupling layers, too. E.g. for clusters on Al<sub>2</sub>O<sub>3</sub>/NiAl(110) [201, 202] or even for single atoms on CuN [203, 204] or NaCl[9, 11].

This is illustrated in figure 5.3b. It shows a line profile over two clusters across the nanomesh-pristine rhodium interface. The cluster on the nanomesh appears about the nanomesh's height too high. The nanomesh itself is at the used bias of 1.5 eV almost invisible.

For the height distribution histogram (see figure 5.3a) this fact is not considered. It has two peaks for the clusters on the nanomesh at 6 and 10 Å. The distance of 4 Å fits perfectly for two hexagonally packed layers. The peak at 10 Å is rather broad indicating a variety of atomic structures as reported in the literature for small clusters [205, 206].

<sup>4</sup>This is only true for biases where the nanomesh is as high as the rhodium. Generally the apparent cluster height is sum of the true cluster height and the nanomesh's true height minus the nanomesh's apparent height.

To estimate the number of atoms in a cluster is difficult. The overview image of the clusters on the partial coverage (figure 5.2) shows a homogeneous distribution of clusters over both areas. There is no reason why more cobalt should arrive on the nanomesh region than on the bare rhodium. The clusters on the rhodium are one monolayer high and around 2 nm in diameter. The clusters on the nanomesh have a similar size. A rough estimation of the number of atoms results in 20 to 100 atoms for most of the clusters. The error in the estimation for the clusters on the nanomesh is about 20 % since neither the height (invisible h-BN) nor the width of the clusters (tip convolution) is directly accessible in STM.



(a) Image of cobalt clusters on the complete nanomesh after three consecutive deposition cycles. The templating effect of the nanomesh results in a hexagonal symmetry (see inset FFT). 100x100 nm<sup>2</sup>, room temperature [128].

(b) 17.5x17.5 nm<sup>2</sup> STM topograph illustrating the clusters in the cavities of the nanomesh, +1.5 eV, 0.2 nA, 4.2 K.

Figure 5.4: Ordering of the cobalt clusters deposited on the nanomesh using BLAG.

The hexagonal alignment of the cobalt clusters in the cavities of the nanomesh can be seen in figure 5.4. The clusters usually do not rest perfectly in the middle of the cavities but the cluster's center is trapped atop of the edge of the cavity. Similar behaviour was observed for naphthalocyanine molecules [143] and copper phthalocyanines [189] as well as pentacene[207]. Merely C<sub>60</sub> molecules rest [21, 173, 208] perfectly in the nanomesh's cavities. For structures bigger than 3 nm used in other studies e.g. gold [168, 169], cobalt [123, 124] or lead [124, 209] this behaviour is lost. Consequently the

cobalt clusters prove the templating capabilities of the BN nanomesh for metal clusters smaller than its periodicity of 3.2 nm.

### 5.3 Coulomb blockade gap?

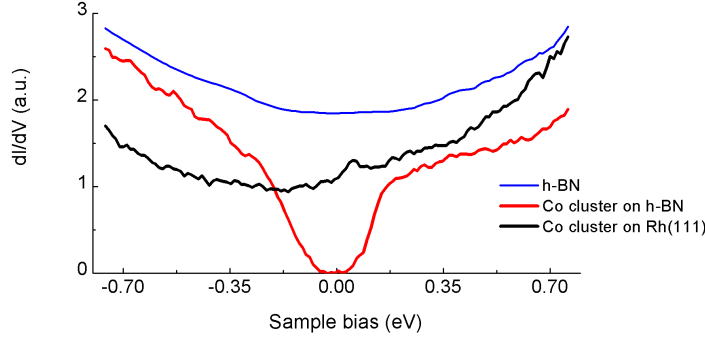


Figure 5.5:  $dI/dV$  spectra on the clean boron nitride nanomesh and on two cobalt clusters.  $I_t = 1$  nA,  $V = +1.5$  eV. The cluster on the nanomesh shows an electronic gap at the Fermi level. Other gap shapes, sizes and positions can be observed. See figures 5.7 and 5.8.

By means of STS the electronic properties of the Co clusters were studied focusing on the role played by the BN nanomesh. The results show the presence of an electronic gap on the Co clusters separated from the metal substrate by the h-BN layer. One example is shown in figure 5.5. The gap shape, size and position can vary on different clusters. What is the origin of this gap?

In small metallic clusters isolated from metallic electrodes, the tunneling process is affected by Coulomb blockade effects[210–213]. This could be observed in several systems of small clusters on thin insulators [201, 214]. The idea is simply an ultras-small double barrier with two serially coupled tunnel junctions as shown in figure 5.6 with a resistance higher than the resistance quantum  $h/e^2$ . The addition of one electron into the cluster increases the energy of the system by a factor

$$E_C = \frac{e^2}{2C} . \quad (5.1)$$

If the capacitance  $C$  of the clusters is small enough, then this capacitive charging energy  $E_C$  is larger than the thermal energy  $k_B T$  and a Coulomb gap opens

$$V_g = \frac{e}{2C} . \quad (5.2)$$

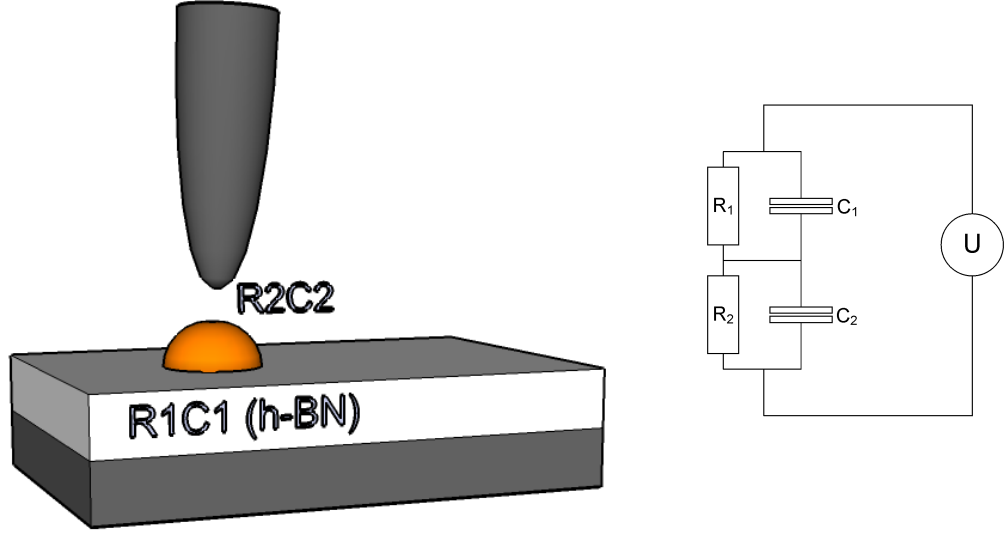


Figure 5.6: Double capacitor model for the cobalt cluster on the h-BN nanomesh on Rh(111). The first tunneling barrier is the single layer nanomesh with  $R_1$  and  $C_1$ . The second capacitor is the vacuum gap between the cobalt cluster and the metallic STM tip ( $R_2D_2$ ).

It is evident that the Coulomb blockade regime is only accessible for small clusters and/or low temperatures. It originates from the charging of the clusters by a single electron and leads to the complete suppression of current at low biases.

For the present system, the capacitance of the Co clusters can be roughly estimated using a plate capacitor model

$$C = \frac{\epsilon_0 \epsilon_{BN} A}{d} \quad (5.3)$$

Assuming for the BN layer a thickness of  $2.2 \text{ \AA}$ , a dielectric constant of 4 [215] and using the contact area  $A$  obtained from the STM topography (that contains tip convolution and apparent height effects), an approximate capacitance of  $1 \cdot 10^{-18} \text{ F}$  is estimated for a Co cluster of  $2.5 \text{ nm}$  diameter. For this value of the capacitance a Coulomb gap  $V_g$  of  $200 \text{ meV}$  is expected. This is consistent with the gap width of the Co clusters adsorbed on the BN nanomesh as shown in figure 5.5. Moreover, while all the spectra measured on Co clusters on the BN nanomesh show a gap, STS spectra measured with exactly the same tip and stabilization conditions on Co clusters on the pristine Rh(111) surface show a clear metallic behavior what excludes tip effects like oxide layers on the tungsten tip[216]. Reference spectra measured on the clean BN nanomesh with the same tip also show a metallic behavior (as explained above, when measuring on the BN nanomesh



at these voltages electrons are directly tunneling into the metal) which excludes the possibility that the gap is also present on the BN confirming that it is an intrinsic feature of the Co cluster on the BN nanomesh.

But is it really a Coulomb gap? There are a few facts that seem to contradict this initial interpretation:

- The gap is not symmetric around the Fermi energy but often shifted to negative bias.
- A Coulomb blockade staircase with equidistant steps of  $e/C$  has never been observed reliably. It should be detectable if  $R_1 C_1 \gg R_2 C_2$  [217, 218].
- The gap width does not scale with size according to equation 5.2. There are narrower and a few wider gaps on very small clusters. Sometimes it is difficult to determine the gap size. Many spectra are asymmetric.

With the publication of Laskowski et al. about the bonding of the BN to transition metal surfaces [178] a new interpretation occurred: The striking similarity to adsorption induced gap states. This possibility had been excluded before because buffer layer assisted growth is supposed to avoid adsorption induced gap states for metals on semiconductors and insulators [187]. But Stroscio et al. saw a very similar phenomena for iron clusters on GaAs(110) [219]. In the case of cobalt on the nanomesh there are some similarities of the DOS for h-BN on Co(111). But the peaks do not coalesce for all microscopic tips as they should to support this explanation and Stroscio et al. saw the adsorption induced gap states on the surface close to the cluster not on the clusters themselves. A typical example that lead to this interpretation is shown in figure 5.7b. And the clusters are most likely only physisorbed on the nanomesh. At low bias and/or high currents or fast scanning speeds the clusters move to the tip and disappear from the surface irreversibly.

The origin of the gap is presumably a different one.<sup>5</sup> The cobalt clusters are small, in the order of a few ten atoms. This is the range of the transition of atomiclike to metallic characteristics [220, 221]. The discrete energy levels of single atoms develop to a quasicontinuous behavior around the Fermi energy with increasing number of atoms

---

<sup>5</sup>This interpretation was inspired by a talk given by T.S. Rahman, UCF, Florida, USA. I thank her for the fruitful discussion on the topic.

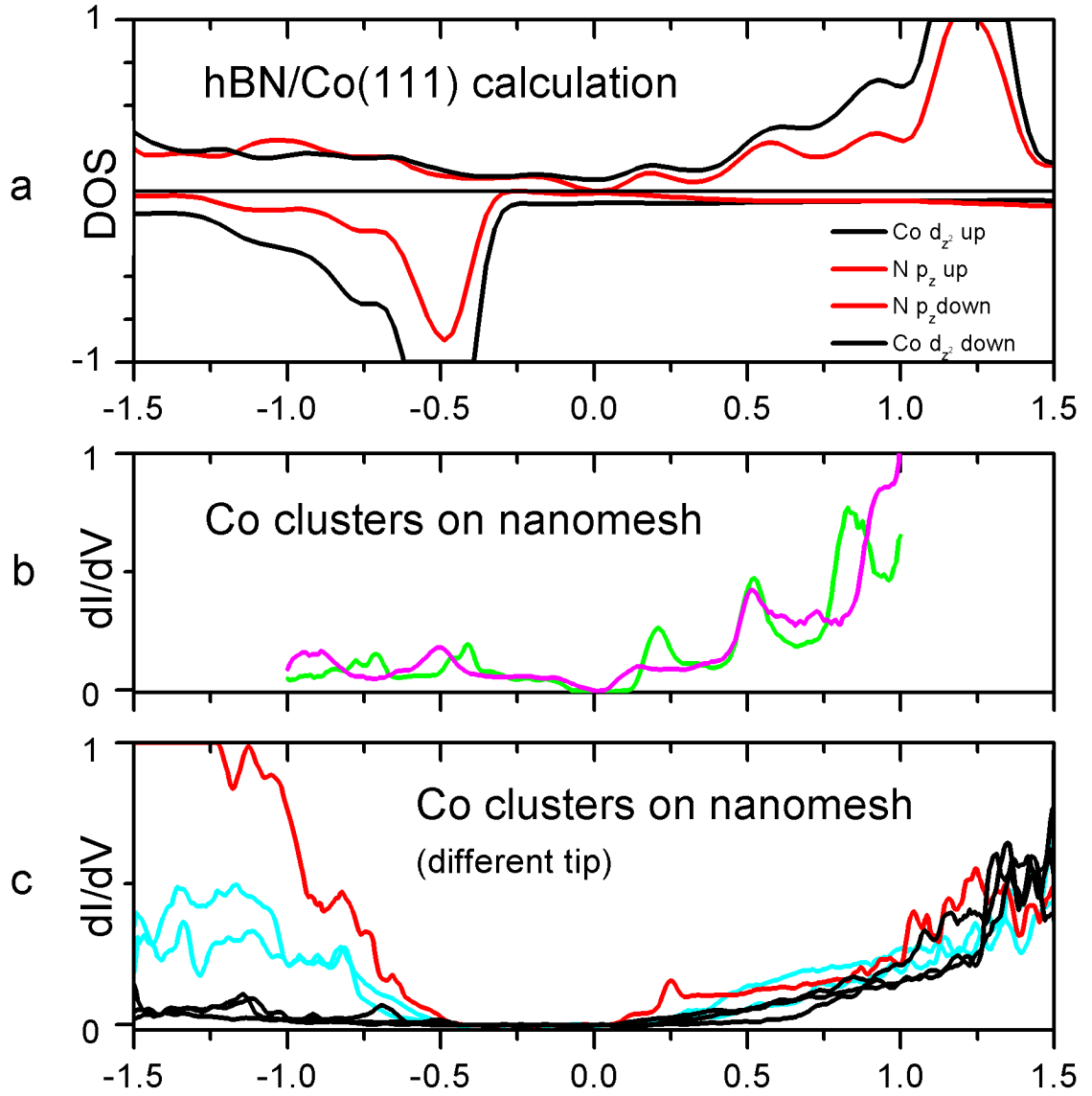


Figure 5.7: Comparison of  $dI/dV$  spectroscopy on Co clusters ( $\sim 3$  nm) (**bc**) and the calculated density of states (**a**) by Laskowski et al. [178].

**a** Spin resolved projected DOS for h-BN on Co(111). Only the surface Co  $d_{z^2}$  and the nitrogen  $p_z$  states are shown. **bc**  $dI/dV$  spectra on top of the Co clusters on the nanomesh at 4.3 K with different tips. **b** shows  $dI/dV$  spectra on two different clusters with a dirty tip. The spectra resemble a Coulomb blockade staircase and show striking similarities to the calculated DOS (h-BN/Co(111), spin up). **c** shows spectra on three different clusters with different tips that were featureless on the clean nanomesh. All units are arbitrary.

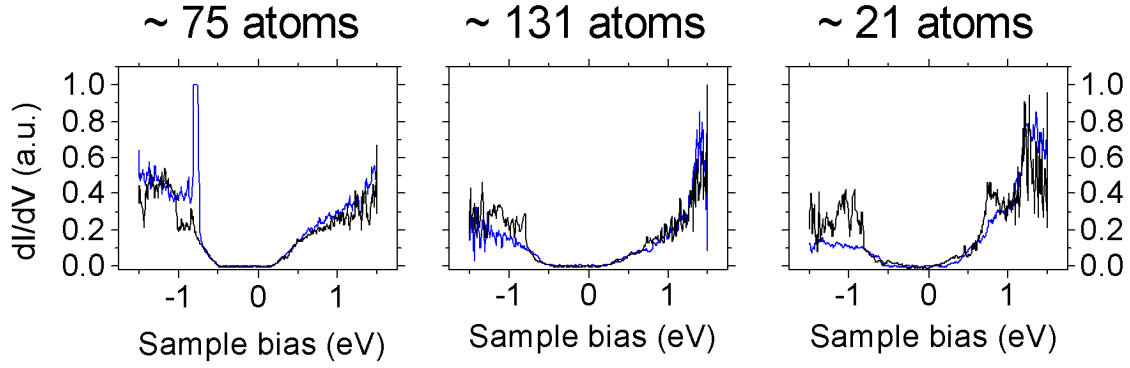


Figure 5.8:  $dI/dV$  spectra on three different cobalt clusters with appr.  $75 \pm 19$ ,  $131 \pm 30$  and  $21 \pm 7$  atoms. The blue lines are repetitions after one hour to check the reproducibility. Stabilization conditions:  $I_t = 1$  nA,  $U_{sample} = 1.5$  eV, 4.4 K.

in the cluster. The mean energy level spacing in the free electron approximation [222] is

$$\delta E \sim \frac{2\pi^2 \hbar^2}{m_e k_F V} \quad (5.4)$$

where  $m_e$  is the electron mass,  $k_F$  the Fermi wave vector and  $V$  the cluster volume.<sup>6</sup> According to the spherical jellium model for small particles the upper limit for the mean energy level splitting is [198]

$$\Delta E \sim \frac{\hbar^2 k_F \pi}{2.71 m_e r_{cluster}}. \quad (5.5)$$

The critical cluster size  $N_C$  for the transition to metallic behavior [220] is temperature dependent and follows

$$N_C \propto \frac{1}{\sqrt{cluster\ size}} \quad (5.6)$$

A generic phase diagram for free cobalt clusters has been shown by Aguilera-Granja et al. [220, 224]. They provide a clear transition to metallic behavior as a function of temperature and cluster size. Figure 5.9a taken from Lin et al. [225] shows experimental results for the energy gap in gold clusters on thin MgO in agreement with the decoupled Co clusters.

The values for the critical cluster size for the molecular-metallic transition given in the literature vary considerably. Alonso and Aguilera-Granja et al. give 31 to 35 atoms

<sup>6</sup>A more general form would be  $\delta E = 1/\mathcal{N}(\varepsilon_F)$  with  $\mathcal{N}$  as the density of states per spin state [23]. The case of semiconductor quantum dots that show a similar behavior for larger sizes (similar to their De Broglie wavelength of  $\approx 7$  nm) due to the reduced charge carrier densities can be understood. [223]

at 110 K, 55 atoms at liquid nitrogen temperature and 93 atoms at 44 K [220, 224]. At 4.2 K the critical clusters size is even higher.

The discrete energy levels bunch together to electronic shells [199, 226]. The resulting gap that forms in the electronic structure of small (cobalt) clusters is a gap between the highest occupied molecular orbital (HOMO) and the lowest unoccupied molecular orbital (LUMO). The expression *molecular* orbital is commonly used in the literature though highest occupied *cluster* orbital would be more appropriate. With increasing number of atoms per cluster and/or with increased thermal broadening of the orbitals the cluster becomes metallic.

Apart from photo emission and point-contact spectroscopy studies [227, 228] there are only a few reports about experimental (STM) work on decoupled individual small cobalt clusters and their electronic structure so far<sup>7</sup>. But the size of the HOMO-LUMO gap and its position relative to the Fermi level has been subject of a couple of theoretical studies: Sebetci et al. provide HOMO-LUMO gaps for very small cobalt clusters in the range of 1 to 6 atoms. The HOMO-LUMO gap varies between 0.4 and 1.04 eV depending on the number of atoms and their orientation. Singh and Kroll calculated the HOMO-LUMO gaps for bigger clusters of 13, 55 and 147 atoms [231]. Their gaps for the majority spin are 0.5, 0.23 and 0.15 eV respectively. Ma et al. report HOMO-LUMO gaps of 0.1 to 0.7 eV for cobalt clusters up to 13 atoms [232].

Other authors working on small cobalt clusters and their magnetic properties did not determine the HOMO-LUMO gap. Datta et al. provide a detailed overview of possible configurations for clusters from 1 to 20 atoms [206]. Aguilera-Granja and Rodriguez-Lopez et al. [205, 233] calculated bigger clusters up to 60 atoms, too.

Though the values for the HOMO-LUMO gaps given in the above mentioned papers vary they are in the same order of magnitude and within the estimation from equations 5.4 and 5.5. Many authors deal with the differences of the electronic properties not only with the cluster size but they highlight the influence of the structural isomers explicitly. In most of the experimental references the authors show deviant spectra for different clusters both in the sub meV as well as in the eV energy range [222, 227].

Despite many groups report on the magnetic properties of small cobalt clusters [233–236] the application of magnetic fields up to 10.5 T perpendicular to the surface (one

---

<sup>7</sup>Odom et al. studied even smaller cobalt clusters on nanotubes that showed a Kondo resonance [229]. Sell et al. and Schouteden et al. deposited bigger clusters on Ge(001) [230] and Au(111) [222] respectively.

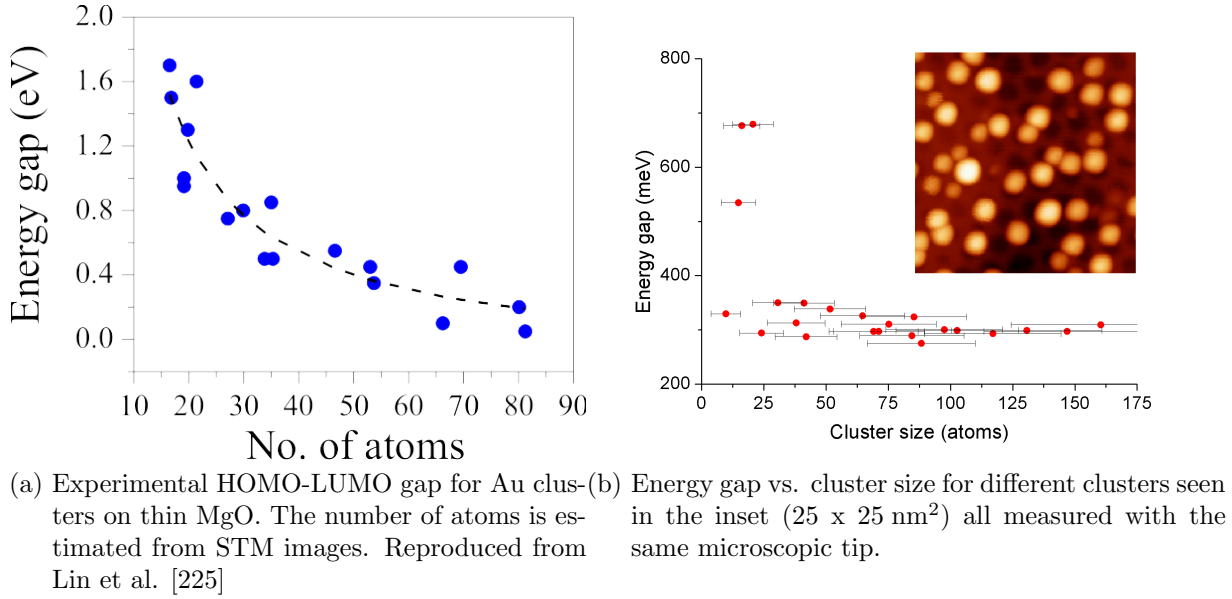


Figure 5.9: Size dependent energy gaps in decoupled cluster.

direction only) did not produce any clear change in the  $dI/dV$  spectroscopy.

To summarize, the cobalt clusters on the nanomesh are in a different electronic environment than on the bare rhodium substrate. They appear with a different height and shape in the STM topography and seem to grow with the hcp plane parallel to the nanomesh. The electronic gap initially explained as a Coulomb gap can be attributed to the HOMO-LUMO gap of small clusters. The boron nitride nanomesh avoids hybridization of the molecular orbitals of the clusters with the metallic substrate. This is the proof of its decoupling properties.



## 6 Pb particles on h-BN

The effect of fluctuations on superconductivity of low dimensional systems has been a subject of research for the past few decades [238–242]. However, recent technological developments have opened the possibility to synthesize and characterize high quality nano-structures, which has renewed the interest in this field [24, 243, 244].

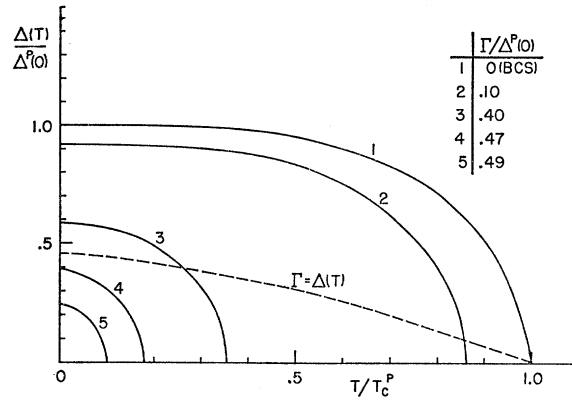


Figure 6.1: Curves 2-5 show the superconducting gap width  $\Delta(T)$  in planar tunnel junctions for a successively increased amount of paramagnetic impurities deviating from the BCS [245] behavior (1) vs. temperature. Reproduced from S. Skalski et al. [246, 247].

Fluctuations are not only present for low dimensions but can be caused by e.g. paramagnetic impurities, too. The work by Skalski et al. [246, 247] addressed the impact of magnetic impurities on the superconducting energy gap and the transition temperature as shown in figure 6.1.

The transition from superconductor to normal conductor at zero magnetic field is a second order phase transition and therefore, it is expected that superconducting fluctuations should lead to a critical region beyond  $T_c$ , where the mean field theory breaks down and the fluctuations in the order parameter  $\Psi$  become significant [248–250].

$$\Psi \sim \frac{\delta \Psi^2}{\Psi_0} \quad (6.1)$$

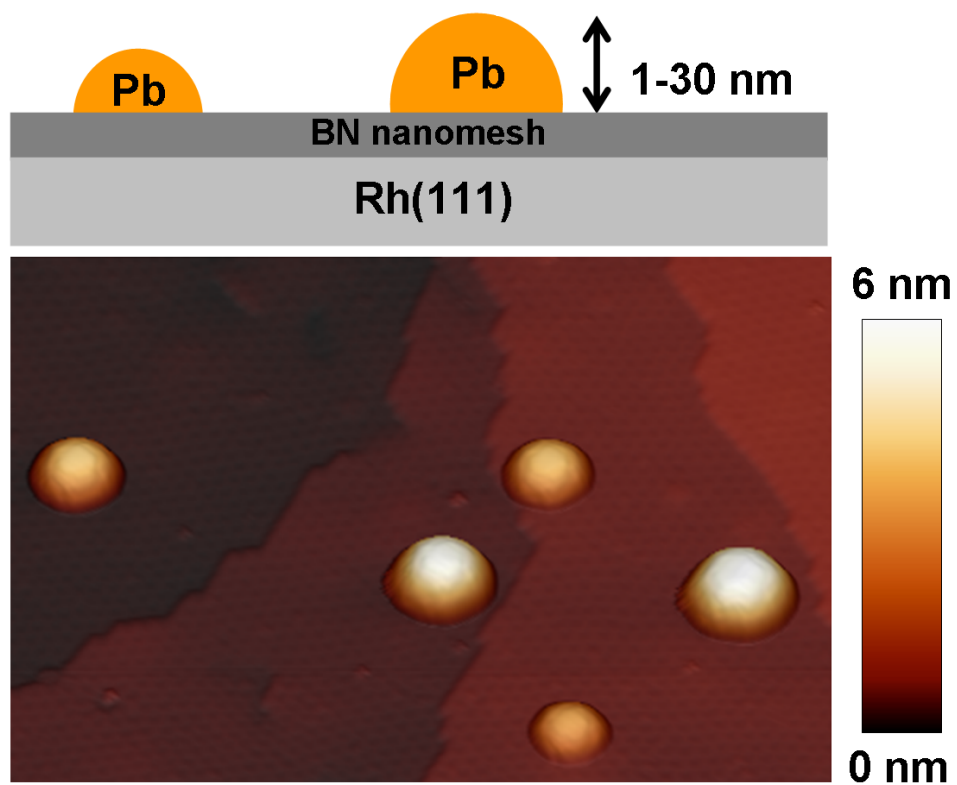


Figure 6.2: The top panel shows a schematic of the system studied with isolated Pb nanoparticles grown on top of a BN monolayer formed on Rh(111) substrate. The lower panel is a typical STM image showing the general morphology of the samples with isolated Pb nanoparticles of different sizes. The scale bar is shown to the right of the image.



where  $\Psi_0$  is the equilibrium order parameter at the temperature  $T$ . For bulk classical superconductors the width of the critical region is very small [251]

$$\frac{dT}{T_c} \sim \frac{T_c^4}{E_F} \sim 10^{-12} \quad (6.2)$$

and hence cannot be accessed through experiments.

As the size of the superconductor is reduced to nanometer length scales, an enhancement of the fluctuations compared to bulk is expected, thereby increasing the width of the critical region [238, 252]. This opens up the critical region for experimental investigations [239, 240, 243].

However, an accurate measurement of the width of this critical region can only be achieved by measuring the superconducting properties of single, isolated nanoparticles. Therefore, it is appealing to probe how superconducting fluctuations affect superconductivity in nanoparticles where the number of electrons taking part in superconductivity is of the order of a few 1000.

Till date, only the pioneering experiments by Ralph and coworkers have been able to detect superconductivity of individual nanoparticles [28, 253] by fabricating single electron transistor devices with an embedded superconducting nanoparticle. Their measurements in single Al grains capped with a thick insulating  $\text{Al}_2\text{O}_3$  layer showed that superconductivity persists much below the coherence length.<sup>1</sup>

In fact, it was argued by Anderson half a century ago that superconductivity is suppressed only when the mean level spacing

$$\delta = \frac{1}{\mathcal{N}(\varepsilon_F)} \sim \frac{1}{\text{volume}} \quad (6.3)$$

becomes larger than the bulk superconducting energy gap  $\Delta$  [27]. The validity of the Anderson criterion and the evolution of the superconducting transition temperature ( $T_c$ ) with particle size have been studied previously on ensemble averaged systems [256–260].

However, these experiments did not address the mechanism for the destruction of superconductivity or the role of superconducting fluctuations in a single nanoparticle, possibly due to the difficulty in controlling the particle size distribution or the inter-particle coupling in those experiments.

Now, it is possible to study of the evolution of superconductivity in single, isolated

---

<sup>1</sup>There are two very recent publications by Wang et al. and a very interesting one by Brun et al. from the group of W.D. Schneider addressing the spectroscopy of Pb islands. But their thin islands are wider than the bulk coherence length and can not be considered zero-dimensional [254, 255].

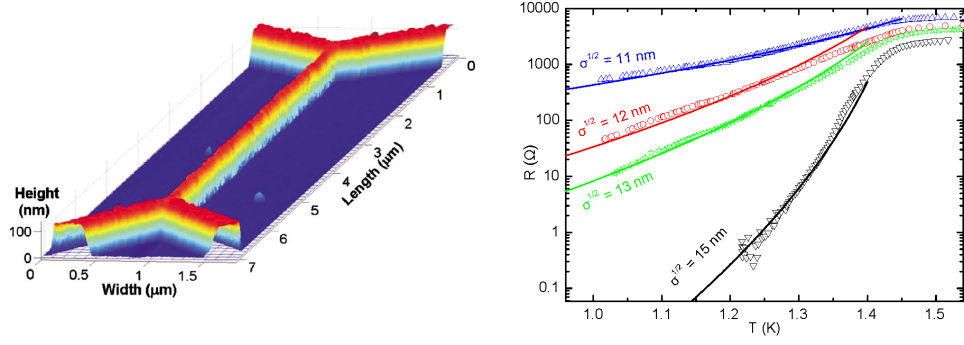


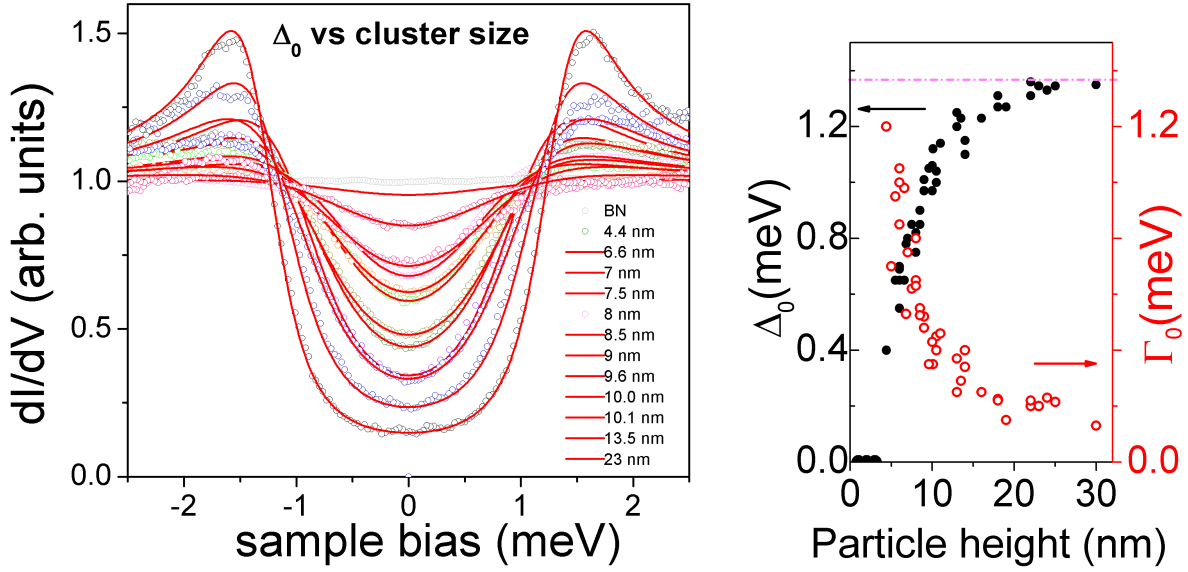
Figure 6.3: Resistance versus temperature (right) for thin Al nanowires (left) with a  $T_c$  of 1.5 K. The resistance is much higher than predicted for thermally activated phase slips and is attributed to quantum fluctuations. Reproduced from M. Zgirski et al. [262].

superconducting nanoparticles as a function of size and temperature. Through the low temperature STM measurements on individual Pb nanoparticles grown in situ, in ultrahigh vacuum conditions, one can address three fundamental questions:

- How small can a superconductor be before it loses its superconducting properties?
- Which is the mechanism behind the destruction of superconductivity in small particles?
- How do fluctuations of the order parameter affect superconductivity and how far in temperature extends the fluctuation dominated region for a single nanoparticle?

The results in this chapter show that both quantum and critical fluctuations affect the superconducting quasiparticle density of states and  $T_c$  of nanoparticles. The analysis of the tunneling spectra at the lowest temperature show that the limiting size of superconductivity is attained when the energy scale associated with the quantum phase fluctuations of the order parameter becomes equal to the mean value of the order parameter itself. Though this was known theoretically [261], it had not been observed since it required measurements on single, isolated nanoparticles.

Moreover, thermal fluctuations give rise to a finite energy gap above  $T_c$  in particles with sizes  $\leq 13$  nm. This persistence of superconductivity beyond  $T_c$  where superconducting fluctuations dominate extends to much higher temperatures than predicted by models based on the Ginzburg-Landau theory or observed in experiments on ensemble averaged nanoparticle systems [238–240, 243, 252, 261].



(a) Conductance spectra for particles with heights varying from 4.4 nm to 23 nm (top to bottom). The open circles denote the experimental raw data. The solid lines are the fits using equation 6.4. The tunneling spectrum measured on the h-BN is shown as a reference (flat line in ash).  
 (b) The superconducting energy gap ( $\Delta(0)$ , black solid circles) and the corresponding broadening parameter ( $\Gamma(0)$ , red open circles) are plotted as a function of particle size. The scale for  $\Delta(0)$  is shown at the left hand side while for  $\Gamma(0)$  it is shown in the right hand side.

Figure 6.4: Particle size impact on tunneling spectra (left) and  $\Delta(0)$  and  $\Gamma_0$  at 1.0 K.

One important question won't be answered in this STM study: What is the resistance of a single nanoparticle? It is known for one-dimensional superconductors that a finite resistance remains for very thin wires due to quantum fluctuations [263]. Zgirski et al. reported recently about superconducting Al nanowires [262] where quantum fluctuations for wire diameters smaller than 13 nm lead to a finite resistivity below  $T_c$  (see figure 6.3). Considering zero-dimensional particles as short one-dimensional wires the resistivity should be non-zero even below  $T_c$  in the fluctuation dominated regime.

## 6.1 Low temperature spectroscopy

The preparation of the Pb particles is similar to the preparation of the Co clusters in the previous chapter using buffer layer assisted growth. Pb clusters form directly on the xenon buffer layer due to the reduced interaction with the substrate and grow in size during xenon desorption due to cluster coalescence until making contact with the surface. The final size of the nanoparticles can be tuned by adjusting the amount of deposited

Pb and the buffer layer thickness. In order to study a wide range of nanoparticle sizes, two different sets of preparation parameters were used: 0.5 ML of Pb with 3000 L Xe and 2.0 ML of Pb with 15000 L of Xe.<sup>2</sup> This produced isolated Pb nanoparticles with heights between 1 and 35 nm.

Figure 6.2 shows a typical STM topographic image of isolated Pb nanoparticles of varying size on the h-BN nanomesh on Rh(111). The high resolution STM images reveal that the particles are hemispherical to a good approximation. The height has been chosen as the reference dimension for the particle size as it is measured with very high accuracy with the STM - in contrary to the lateral dimensions where tip convolution can be surprisingly huge for high particles. Apparent height effects as for smaller clusters on the nanomesh are negligible. Conductance spectra ( $dI/dV$  vs.  $V$ ) were measured at 1.0 K on top of each Pb particle of different heights. For all  $dI/dV$  spectra the initial stabilization conditions were  $I_t = 0.1$  nA and a sample bias of 8.0 meV. The modulation frequency was 830 Hz with 50  $\mu$ eV rms (see figure 3.10).

Figure 6.4a shows unprocessed experimental  $dI/dV$  spectra (normalized to the  $dI/dV$  signal at a bias of 4 meV) for different particle sizes. A small asymmetry between positive and negative voltages is observed for some of the spectra. The origin of this asymmetry is not clear at present but could arise from the specific nature of the density of states in the tip. The curves were fitted with the tunneling equation given by Tinkham [252]

$$G(V) = \left. \frac{dI}{dV} \right|_V = G_{nn} \frac{d}{dV} \left\{ \int_{-\infty}^{\infty} N_S(E) \{f(E) - f(E - eV)\} dE \right\} \quad (6.4)$$

Where  $N_S(E)$  is the quasi-particle excitation density of the superconductor,  $f(E)$  is the Fermi-Dirac distribution function and  $G_{nn}$  is the conductance of the tunnel junction for  $V \gg \Delta/e$ .  $N_S(E)$  is given by Dynes et al. [264]:

$$N_S(E, \Gamma, T) = \Re \left( \frac{E + i\Gamma(T)}{\sqrt{(E + i\Gamma(T))^2 - \Delta(T)^2}} \right) \quad (6.5)$$

Where,  $\Delta(T)$  is the superconducting energy gap and  $\Gamma(T)$  is a phenomenological broadening parameter which incorporates all broadening arising from any non-thermal sources<sup>3</sup>. There is an excellent agreement between the experimental data and the theo-

---

<sup>2</sup>These high amounts of xenon lead to a blueish discoloration on the sample that vanishes during warming to room temperature.

<sup>3</sup>Mostly  $\Gamma$  is taken as the broadening associated with the finite lifetime  $\tau$  of the quasiparticle states ( $\Gamma = \hbar/\tau$ ).

retical fits giving unique values of  $\Delta(T)$  and  $\Gamma(T)$  which characterizes ideally the superconducting state of each Pb nanoparticle. Tunneling spectra were unchanged even with microscopic tip changes as long as the tip remained metallic close to the Fermi energy. Moreover, application of a magnetic field led to the disappearance of the gap<sup>4</sup>, which demonstrates that the spectra are associated with superconductivity and not from any other electronic effects.

Figure 6.4b shows the particle size variation of  $\Delta$  and  $\Gamma$  at 1.0 K (denoted as  $\Delta_0$  and  $\Gamma_0$ ). Pb particles larger than 20 nm show a superconducting gap similar to bulk Pb ( $\sim 1.36$  meV).  $\Delta_0$  gradually decreases with reduction in particle size, till it completely vanishes for  $\sim 3$  nm particles, consistent with the Anderson criterion. This shows that superconductivity survives in Pb nanoparticles down till a size which is an order of magnitude smaller than the coherence length  $\xi$  for bulk Pb (86 nm).

Furthermore, the decrease of  $\Delta_0$  with cluster size is concomitant with an increase of  $\Gamma_0$  until  $\Gamma_0 \gg \Delta_0$  at which superconductivity is completely destroyed (figure 6.4b). The increase in  $\Gamma_0$  can be associated with the increase of phase fluctuations arising from the uncertainty relation [252],  $\Delta N \Delta \Phi \geq 1$ .

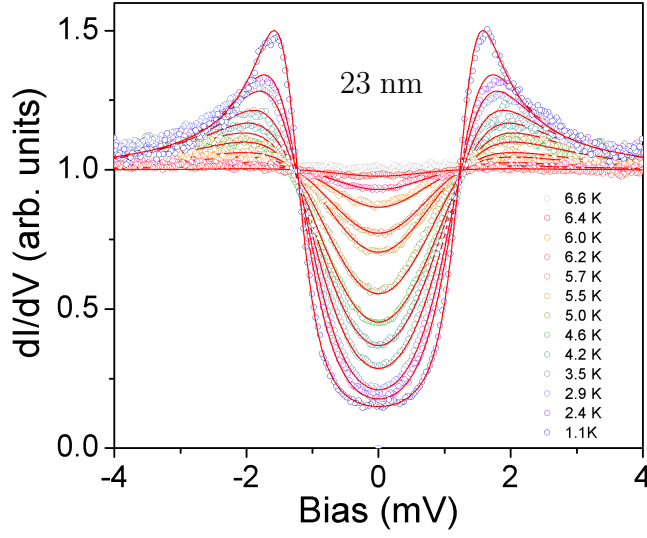
In superconducting nanoparticles, the phase  $\Phi$  of the superconducting wave function becomes indefinite due to the small number of electrons,  $N$ . This increase of phase fluctuations will manifest itself as an increase in the broadening of the tunneling spectra which explains the observed increase in  $\Gamma_0$  at small sizes. These fluctuations are expected to destroy superconductivity when the energy scale associated with the fluctuations ( $\Gamma_0$ ) of the order parameter becomes equal to the mean value of the order parameter ( $\Delta_0$ ) [241, 261]. The results demonstrate that the critical particle size given by Anderson's criterion is the same as the size where superconducting fluctuations destroy superconductivity [261] in zero dimensional superconductors.

The temperature dependence of superconducting properties with reduction in particle size was investigated by acquiring  $dI/dV$  spectra at various temperatures from 1 to 8 K on Pb nanoparticles of different sizes. Figure 6.5a shows the tunneling spectra for two different particles, 10.5 and 23 nm high. Each spectrum is again fitted using equation 6.4 giving  $\Delta(T)$  and  $\Gamma(T)$  as a function of temperature for each particle.

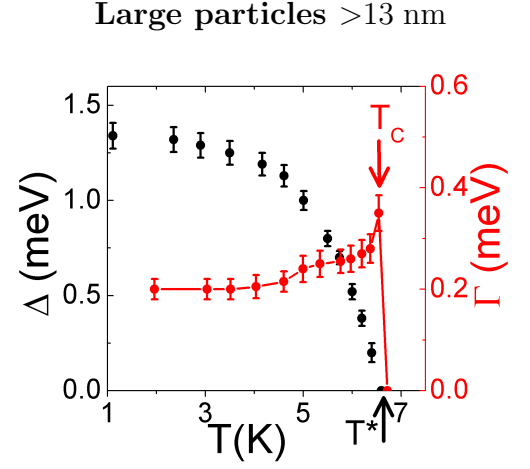
The evolution of  $\Gamma(T)$  is quite different for the two particles (figure 6.5b). In the larger

---

<sup>4</sup>For small particles the Ginzburg-Landau parameter  $\kappa = \lambda/\xi$  becomes higher than  $1/\sqrt{2}$  the limit for a type II superconductor because  $\xi$  scales with the mean free path that cannot be larger than the particle dimensions [265]. The critical field scales with the size. The smallest Pb islands where vortex formation could be observed by Nishio et al. was  $\sim 40$  nm [266].



(a) Conductance spectra as a function of temperature, for two particles of 23 nm and 10.5 nm height respectively. The experimental raw data are shown by open circles (Dark blue for the lowest temperature to red for the highest temperature). The data in ash is taken at a temperature where no superconducting signal is obtained. The solid lines are the fits using equation 6.4. The inset shows in detail the raw data for 5.74 K and its corresponding fit. Notice the quality of the fit at this temperature ( $T > T_c$ ) where the conductance only varies by  $\sim 2\%$ .



(b) The variation of  $\Delta(T)$  (black solid circles) and  $\Gamma(T)$  (red solid circles) with temperature for the two particles as obtained from the fits on the left respectively. We observe that the  $\Gamma(T)$  shows a peak at a particular temperature for both particles which we associate with the superconducting transition temperature  $T_c$ . Interestingly, for the smaller particle we observe a finite energy gap above  $T_c$ .

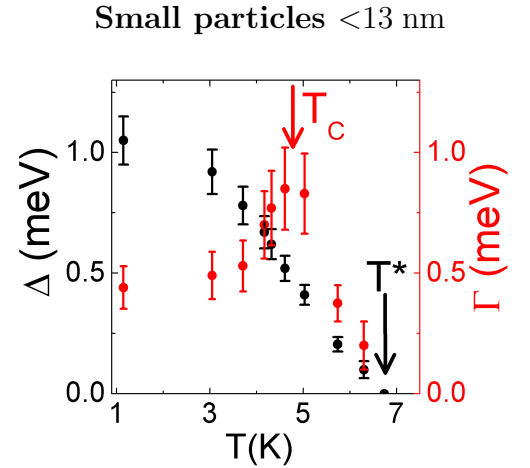
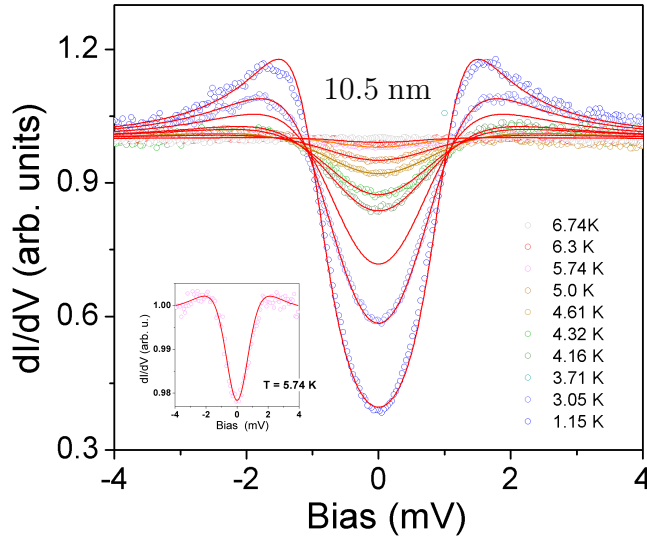


Figure 6.5:  $dI/dV$  spectra and variation of  $\Gamma$  and  $\Delta$  for representative particles for the BCS [245] and the fluctuation dominated regime.

particle,  $\Gamma$  increases monotonically. For the smaller particle it shows a non-monotonic dependence of  $\Gamma$  with temperature.

To understand the difference in the temperature evolution of  $\Gamma(T)$ , the role of thermal fluctuations on the order parameter need to be considered. From the Ginzburg-Landau theory, the fluctuations in the order parameter are given by[252]:

$$\frac{(\delta\Psi)^2}{\Psi_0^2} = \frac{2\pi kT}{H_{c0}^2(1 - \frac{T}{T_c})^2 V} \quad (6.6)$$

Where,  $H_{c0}$  is the zero temperature critical field and  $V$  is the volume of the particle. Equation 6.6 shows that the fluctuations cause a very small fractional change in  $\Psi$  except close to  $T_c$  or in very small particles ( $V \rightarrow 0$ )  $(\delta\Psi)^2$  diverges. Also note above  $T_c$ ,  $\Psi_0 = 0$  while

$$(\delta\Psi)^2 \propto \frac{kT}{V(1 - \frac{T}{T_c})} \quad (6.7)$$

and hence all superconducting effects arise from fluctuations alone [261]. Since fluctuations lead to a broadening of the quasiparticle spectrum, the maximum of  $\Gamma(T)$  is associated with  $T_c$  [267].

The above described method to determine  $T_c$  for the Pb nanoparticles is different from the more conventional methods. Usually  $T_c$  is defined by the temperature for the expulsion of the magnetic field (Meißner-Ochsenfeld) or the disappearance of resistivity. Since one can not perform conventional measurements on isolated nanoparticles, the  $T_c$  is determined from the temperature at which  $\Gamma(T)$  shows a maximum. For bulk Pb the temperature where  $\Gamma(T)$  shows a maximum corresponds to the  $T_c$  (7.25 K) obtained from the more conventional methods. The comparison with bulk properties justifies this definition.

The variation of  $T_c$  with particle size shows a slow decrease down till 4 nm (figure 6.6a). Below 4 nm  $T_c$  drops sharply to zero where the Anderson criterion is reached. This variation in  $T_c$  is consistent with earlier reports on small particles of Pb where a decrease in  $T_c$  has also been observed, though measurements were performed on ensemble averaged systems [257, 268].

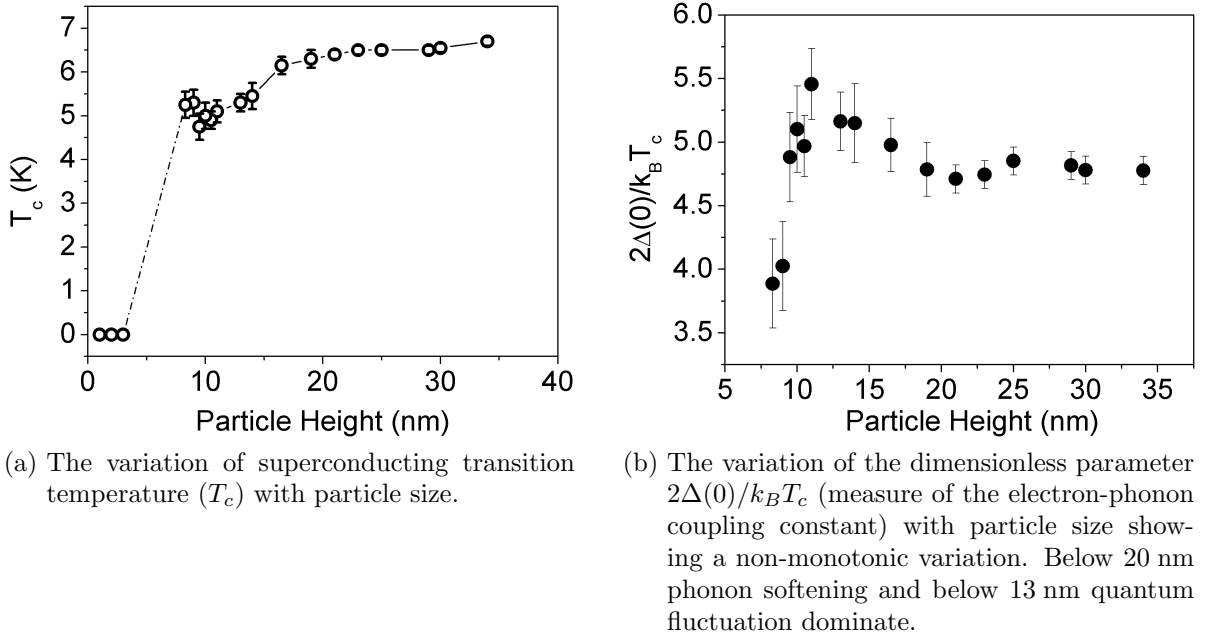


Figure 6.6

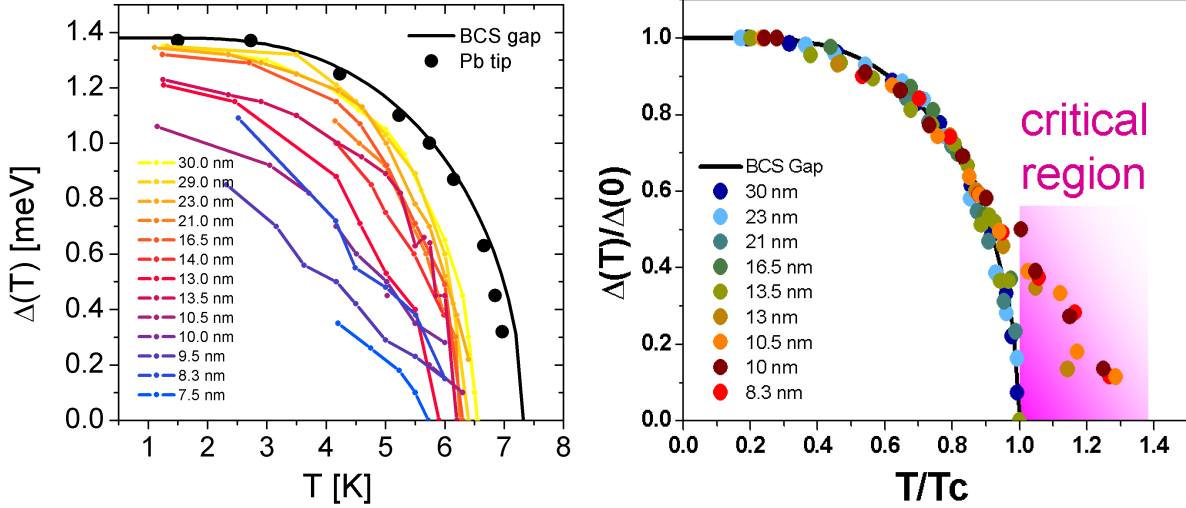
## 6.2 Quantum and critical fluctuations in the superconductivity of single, isolated Pb nanoparticles

The size variation of  $T_c$  in nanoscale superconductors is usually explained on the basis of two mechanisms: Surface effects and quantum size effects. Surface effects lead to a decrease of the surface phonon frequency [269] which increases the electron-phonon coupling strength ( $\lambda$ ) [270, 271] while, quantum size effects are expected to decrease  $\lambda$  for a strong coupling superconductor like Pb till it reaches the BCS value [272].

Figure 6.6b shows the variation of  $2\Delta_0/k_B T_c$  (a measure of  $\lambda$ ) with particle size. The non-monotonic variation of the electron-phonon coupling ( $2\Delta_0/k_B T_c$ ) with particle size demonstrates that there is an interplay of surface and quantum size effects which leads to the small decrease in  $T_c$  with particle size as observed in Pb nanoparticles. It is worth noting that for particle sizes where quantum size effects dominate (e.g.  $< 11$  nm), superconducting fluctuations become important which could also modify the BCS-Eliashberg theory gap ratio of  $2\Delta_0/k_B T_c$ .

Finally, to investigate the effect of critical fluctuations close to  $T_c$  in small particles,





(a) Not normalised gap  $\Delta(T)$  vs.  $T$  for Pb nanoparticles (colored) and bulk Pb tip (black solid circles). Normalisation to  $T^*$  would lead to lower  $\Delta(T)$  than the BCS value at the same reduced temperature. Note the similarities to figure 6.1.

(b) Reduced gap  $\Delta(T)/\Delta(0)$  vs. reduced temperature ( $T/T_c$ ) for different nanoparticles shown by closed circles (dark blue for the largest 30 nm particle to red for the smallest 8.3 nm particle).

Figure 6.7: Superconducting gap vs. temperature data for different clusters deviates from the BCS behaviour ( $\Delta(T) = \Delta(0) - \sqrt{2\pi\Delta(0)k_B T_c} \cdot \exp(-\Delta/k_B T)$ ) [273]. Normalization with  $T_c$  ( $< T^*$ ) leads to the appearance of a tail beyond  $T_c$  for particles with sizes  $\leq 13$  nm indicating a fluctuation dominated regime for these small nanoparticles.

$\Delta(T)/\Delta(0)$  for different nanoparticles is plotted as a function of  $T/T_c$  (figure 6.7b). While the larger particles ( $>13$  nm) follow the expected BCS functional form for all temperatures, for the smaller particles the  $\Delta(T)$  vs.  $T$  forms a tail at higher temperatures with non zero  $\Delta$  above  $T_c$ .

Interestingly, this indicates that for small particles there is a fluctuation dominated regime characterized by a finite energy gap beyond  $T_c$ . This fluctuation dominated regime persists up to a temperature  $T^*$  ( $> T_c$ ), beyond which  $\Delta \approx 0$ .

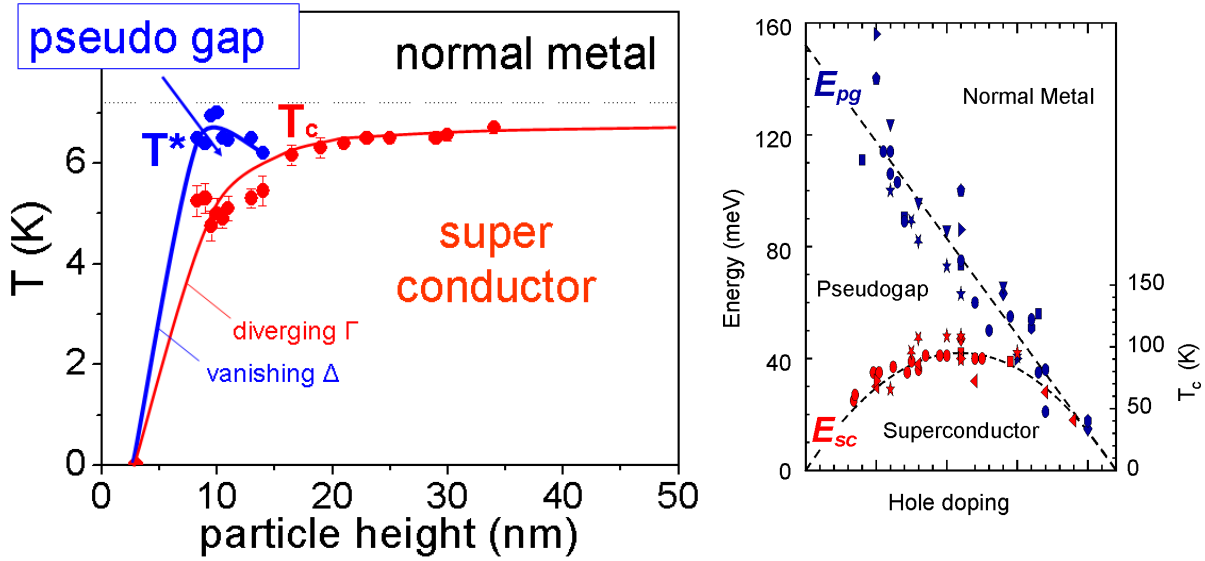
A schematic phase diagram outlining the superconducting and fluctuation dominated phases is plotted in figure 6.8a. For larger particles ( $>13$  nm), the estimated critical temperatures  $T_c$  and  $T^*$  are identical within the experimental error.

However, for the smaller particles ( $< 13$  nm)  $T^*$  is higher than  $T_c$ , extending up to  $\sim 1.4 T_c$ . The effect of fluctuations on the thermodynamic properties based on the Ginzburg-Landau theory predicts the width of the fluctuation regime in zero dimensional superconductors to be given by [243, 261, 274]:

$$\frac{\delta T}{T_c} \approx 13.3 \frac{T_{c0}}{E_F} \sqrt{\frac{\xi_0^3}{V}}, \quad (6.8)$$

where,  $\xi_0$  is the bulk coherence length and  $V$  is the volume of the particle. Using this equation the width of the fluctuation region is expected to extend to  $\sim 1.1 T_c$  for a 10 nm Pb particle. This has also been observed experimentally from measurements of diamagnetism in an ensemble averaged Pb nanoparticle system [243]. Interestingly, the local scale experiments on single nanoparticles show a much higher fluctuation dominated regime than observed previously. A large fluctuation dominated regime has also been observed for the high  $T_c$  cuprate superconductors in the pseudogap phase though proper understanding of this phase is still lacking [276].

It needs to be pointed out that since it is difficult to have a direct experimental measure of the mean field  $T_c$  for the small nanoparticles, one could also choose a different criterion to define it. If one chooses the temperature for the vanishing of the superconducting energy gap as the  $T_c$  (i.e.  $T^* =$  mean field transition temperature), then it appears that for small particles below 13 nm, there is a strong deviation from the usual BCS variation of the temperature dependence of the gap (see also figure 6.7a). In addition,  $2\Delta(0)/k_B T_c$  also decreases below the BCS weak coupling value of 3.52 for the small nanoparticles. Though one cannot rule out this explanation completely, it seems less likely as in this regime the mean level spacing  $\delta$  is still much lower than the



(a) Schematic phase diagram for the superconducting Pb nanoparticles as a function of particle size. Two different phases appear: a pure superconducting region and a fluctuation dominated regime. While all the nanoparticles have the pure superconducting region, the small nanoparticles ( $\leq 13$  nm) also show a fluctuation dominated regime in between  $T_c$  and  $T^*$ , where there is a finite energy gap beyond  $T_c$ .

(b) Simplified extract of a high  $T_c$  superconductors' phase diagram (reproduced from [275]). The role of the particle height is assigned to the doping level in HTSC. Similar to (a) there are a superconducting, a normal metal/insulator and a pseudogap region. The red symbols denote  $T_c$  while the blue mark  $T^*$ .

Figure 6.8: Generic phase diagram derived from figure 6.7b and comparison to high  $T_c$  superconductors' phase diagram (b) (reproduced from [275]).

superconducting energy gap  $\Delta(0)$  which ideally sets the limit for the validity of the BCS model in small particles.

To summarize, superconducting fluctuations affect the quasiparticle energy spectrum and superconductivity in small Pb nanoparticles. Quantum fluctuations of the order parameter determine the length scale down to which superconducting correlation persists. This length scale corresponds to the same critical particle size for the destruction of superconductivity as predicted from the Anderson's criterion.

Critical fluctuations give rise to a finite energy gap above  $T_c$  for particles where quantum size effects start to dominate. This fluctuation dominated regime extends to higher temperatures than predicted by models based on the Ginzburg-Landau theory. In addition, the present results also show that there is an interplay of surface effects and quantum size effects which influences the variation of  $T_c$  in this strong coupling zero dimensional superconductor.



# 7 Sn nanoparticles

## 7.1 Superconducting proximity effect

Superconducting proximity effects [277–279] occur at a normal metal/superconductor interface. The superconducting wave function varies smoothly across the interface changing the properties in both materials. The superconductivity leaks into the normal metal where Cooper pairs can be found with a certain probability. On the other hand side the pair breaking probability in the superconductor rises. The superconducting energy gap decreases close to the interface and recovers in the bulk of the superconductor.

The corresponding length scales are the normal state and superconducting coherence lengths  $\xi_N$  and  $\xi_S$

$$\xi_{N,S}(T) = \sqrt{\frac{\hbar D_{N,S}}{2\pi k_B T}} \quad (7.1)$$

where  $D$  is the diffusivity of the normal and the superconductor, respectively. Note that for  $T \rightarrow 0$  both lengths diverge.

Proximity effects have been studied intensively in the 1960s. They are well known for Pb films [280, 281] and have been studied recently for granular structures or nanocomposites [282, 283] in direct contact with a normal metal. As a general result the superconducting energy gap decreases.

Since the observations in the Pb nanoparticles in the previous chapter has some similarities to proximity effects like the reduced  $T_c$  for small particles it was always a point of discussion if really size effects or merely the proximity effect could be the reason for the observed reduction in the superconducting energy gap. There are already two striking arguments against proximity effects: a) the evolution of  $\Delta$  with particle size reaches the bulk value already for particle heights around 20 nm and b) no energy gap could be found in the  $dI/dV$  spectra down to 1 K close to the particles on the h-BN/Rh(111) substrate (as it has been observed e.g. by le Sueur et al. [284]).

In order to exclude the possibility of proximity effects Sn nanoparticles of the same size range (2–30 nm) were deposited on the boron nitride nanomesh using buffer layer

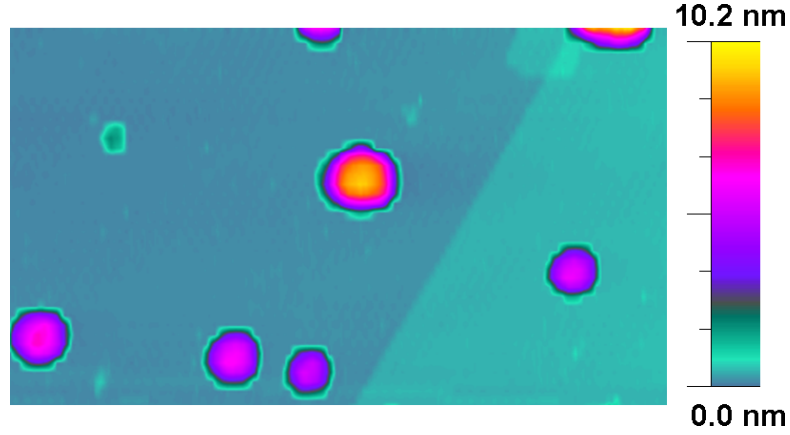


Figure 7.1: STM image showing Sn clusters on the h-BN/Rh(111) substrate. The scale bar is shown in the right.  $200 \times 120 \text{ nm}^2$ ,  $+1.5 \text{ eV}$ ,  $0.1 \text{ nA}$ .

assisted growth. Sn is well known to show an increase in  $T_c$  for reduced sizes (in ensemble measured systems) while the proximity effect leads to reduced  $T_c$ , too [103, 285].

## 7.2 Shell effects in Sn nanoparticles

One of the most exciting predictions is the occurrence of shell effects, very similar to the presence of electronic shell structure in atomic, nuclear and cluster physics (as mentioned in chapter 5), which leads to huge enhancements of the superconducting energy gap ( $\Delta$ ) [286–288] at certain particle sizes. Here, through the STS measurements on single, isolated Sn nanoparticles it is shown that minor changes in the particle size leads to large variations in  $\Delta$ , as large as 100 %. The observed oscillations of the superconducting energy gap can be described quantitatively through finite size corrections in the BCS model. Interestingly, the results on Sn are in contrast with those on Pb nanoparticles, where no such oscillations are observed. This difference is due to the comparatively shorter coherence length in Pb which suppresses the finite size corrections. The results demonstrate that as a consequence of the shell effects the superconducting energy gap can be enhanced by  $\sim 60 \%$  from its bulk value by only tuning the particle size in Sn nanoparticles.

There has also been a surge of theoretical interest in ultrasmall superconductors [241, 289, 290]. Exciting predictions have been made recently regarding the occurrence of shell effects in clean, superconducting nano-particles [286–288]. The origin of shell effects is primarily due to the discretization of the energy levels in small grains which leads to

substantial deviations of from the bulk limit. For small particles, the number of discrete energy levels within a small energy window ( $\pm\Delta$ ) around the Fermi energy  $E_F$  fluctuates with very small changes in the system size (which moves slightly the position of  $E_F$ ). Consequently this leads to fluctuations in the spectral density around  $E_F$ . Since, in superconductivity only electrons around  $\pm\Delta$  of  $E_F$  participate in pairing, an increase (decrease) of the spectral density around  $E_F$  will make pairing more (less) favorable, thereby increasing (decreasing)  $\Delta$ . As a consequence the gap becomes dependent on the size and the shape of the grain. The amount of fluctuations also increases with the symmetry of the particle [288], since symmetry introduces degeneracies in the energy spectrum. It is easy to see that these degenerate levels, usually referred to as shells in nuclear, atomic and cluster physics [199], will enhance the fluctuations in the spectral density and also in the gap as the number of levels within  $\pm\Delta$  of  $E_F$ , and consequently the number of electrons taking part in pairing, fluctuates dramatically. For cubic or spherical grains this might lead to a large (above 50 %) modification of  $\Delta$ . Theoretically, these shell effects will be described quantitatively by introducing finite size corrections to the BCS model [288].

Despite the potential interest of the occurrence of shell effects in the context of superconductivity there has been no experimental proof of the phenomena so far. This is largely due to the fact that this requires measurements on single, isolated particles where the shape is well defined and the size can be tuned. In addition, in order to test the theoretical predictions, measurements have to be done in systems which fulfill the following criteria:

1. the particle has a certain degree of symmetry
2. the coherence length is much longer than the particle size
3. the BCS model is applicable
4. the bulk gap is larger than the mean level spacing.

Here, it is shown experimentally for the first time the existence of shell effects in small superconductors. Through the STM measurements on individual hemispherical nanoparticles of Sn grown in situ, in ultrahigh vacuum conditions, large oscillations in the low temperature superconducting energy gap  $\Delta$  with particle size were observed. The results demonstrate that it is possible to enhance  $\Delta$  by more than 60 % by tuning the particle size.

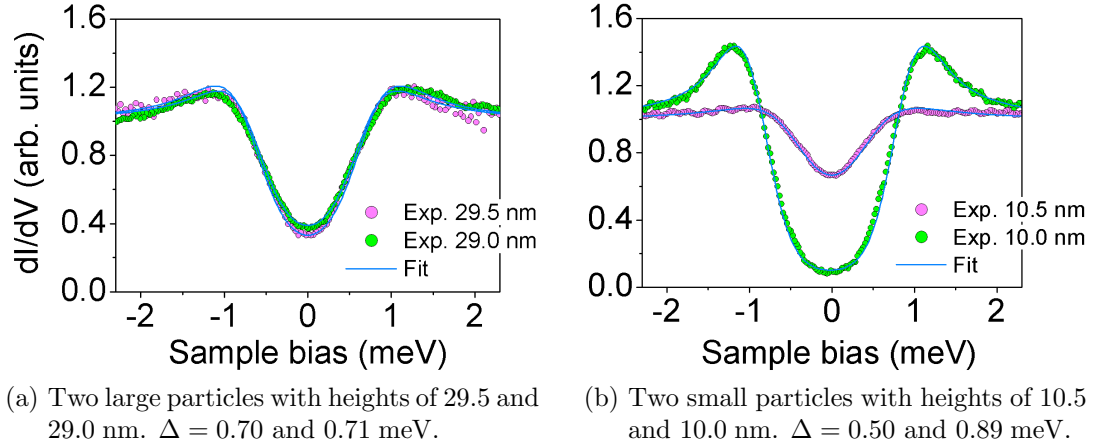


Figure 7.2: Experimental measurement of the superconducting energy gap in Sn nanoparticles by STM. Tunneling DOS (solid symbols) along with the theoretical fits (solid lines) measured by STS at  $T = 1.4$  K.

Theoretical finite size corrections to the BCS formalism for hemispherical Sn nanoparticles provide a very good quantitative description of the experimental data. Further one can show that the large oscillations in  $\Delta$  are strongly suppressed in Pb, a strong coupling superconductor. The theoretical reason is that the coherence length in Pb is comparatively shorter than the coherence length in Sn. This is a further indication of the validity of this model of shell effects in metallic nanoparticles.

Figure 7.1 shows a typical STM topographic image of isolated Sn nanoparticles on hBN/Rh(111), where the size varies between 2 – 30 nm. The STM images reveal that particles are hemispherical to a good approximation which implies that the particles have a well defined symmetry. The height was chosen as the reference dimension for the particle size as it is measured with very high accuracy with the STM. Conductance spectra ( $dI/dV$  vs  $V$ ) were measured at 1.4 K on top of each Sn particle of different heights. Plots in figure 7.2 illustrate the results both for large and small sized Sn nanoparticles respectively. They show unprocessed experimental normalized  $dI/dV$  spectra (normalized with  $dI/dV$  at  $V = 4.0$  meV) for two similar sized large particles (b) and two similar sized small particles (c), which give their density of states (DOS).

The curves were fitted with the same procedure as used in the previous chapter giving the value of  $\Delta(T)$  for each nanoparticle. One observes from figure 7.2 that though the large particles differing in a size of 1 nm have similar DOS signifying similar gaps, there is a huge difference in the DOS for the smaller particles even if they differ less than 1 nm in size. The  $\Delta$  obtained from the fits differ by  $\sim 80\%$  for the small particles,



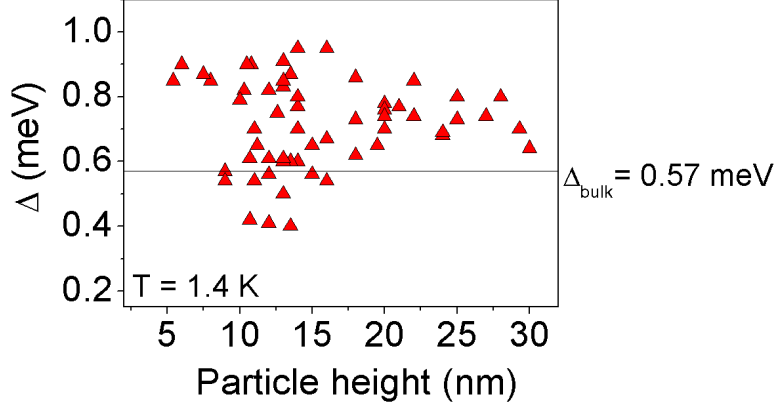


Figure 7.3: Variation of the superconducting energy gap ( $\Delta_0$ ) measured at  $T = 1.4$  K with particle height. Large oscillations in the gap ( $\sim \pm 50$  %) for particles below 20 nm.

exemplifying the enormous oscillations in gap values present in the smaller particles. This is more clearly visible in figure 7.3 where the gap values are plotted as a function of particle size. Below a particle size of 20 nm, gap values differ even more than 100 % for similar sized particles. Interestingly, the gap for the largest particle measured is also higher than the bulk gap of Sn by 20 %.

In order to explain the experimental results a theoretical study of finite size corrections in the BCS formalism in line with references [287, 288] was carried out by/in cooperation with Prof. A.M. Garcia-Garcia from Princeton and Dr. J.D. Urbina from the University of Regensburg. One of the contributions comes from the corrections to the BCS mean field approximation which is obtained in the grand canonical ensemble with a variable number of electrons which is no longer valid for small particles with a fixed number of electrons. The other contribution arises from finite size corrections to the BCS gap equation.

For the first contribution, the leading finite size corrections to the BCS mean field formalism, obtained by using the exact solution of the Richardson model [291], tends to suppress superconductivity [292]. It leads to a monotonic decrease of the gap as the system size decreases and hence does not play a role in the experimentally observed oscillations.

For the second contribution, two types of corrections are identified [287, 288], smooth and fluctuating. The former depends on the surface and volume of the grain and always enhances the gap with respect to the bulk [288]. Since it decreases monotonously with the system size it is not relevant in the description of the experimental fluctuations.

The starting point to study the fluctuating part is the self consistent equation for

the BCS order parameter  $\Delta(\varepsilon)$ . The finite size corrections to the gap arise from the corrections to the matrix elements and the spectral density  $\nu(\varepsilon)$  which enter in the gap equation. Explicit expressions for both can be obtained for a particular geometry of the particle. The gap equation can be solved numerically or analytically in powers of  $1/k_F L$  where  $k_F$  is the Fermi wave vector and  $L$  is the typical length of the particle [293]. It has been found in references [287, 288] that to leading order the oscillations in the gap are controlled by fluctuations in  $\nu(\varepsilon)$  arising from the discreteness of the level spectrum. Explicit expressions of  $\nu(\varepsilon)$  can be obtained after including the symmetry of the grain in terms of the periodic orbits [293]. As a general rule symmetries in the grain lead to degeneracies in the spectrum and to stronger fluctuations in  $\nu(\varepsilon)$ . To compare with the experimental results,  $\nu(\varepsilon)$  was obtained for a hemispherical particle [294]. The gap equation was then solved in powers of  $1/k_F L$ . To leading order, the oscillating part of the gap is given by:

$$\tilde{\Delta} = \frac{\bar{\Delta}}{2} \frac{3\pi}{k_F R} \sum_{q=1}^{\infty} \sum_{p=2q}^{\infty} A_{pq} K_0 \left( \frac{l_{pq}}{\xi} \right) \sin \left( k_F l_{pq} + \beta_{pq} \frac{\pi}{2} \right) \quad (7.2)$$

$$\begin{aligned} \text{with } A_{pq} &= -\frac{1}{2\pi q} & \text{for } p = 2q \\ &= (-1)^q \sin(2\Theta_{pq}) \sqrt{\frac{\sin \Theta_{pq} k_F R}{\pi p}} & \text{for } p > 2q \end{aligned}$$

$$\begin{aligned} \text{and } \beta_{pq} &= 0 & \text{for } p = 2q \\ &= p + \frac{3}{2} & \text{for } p > 2q. \end{aligned}$$

Here,  $R$  is the radius of the hemispherical particles,  $l_{pq} = 2pR \sin(\Theta_{pq})$  is the length of the periodic orbits,  $\Theta_{pq} = \pi q/p$ ,  $K_0$  is the Bessel function of second order and  $\bar{\Delta}$  is the average gap. The index  $p$  denotes the number of vertices and  $q$  denotes the number of windings of the periodic orbits.

In order to compare with the experimental gap for Sn nanoparticles, the BCS gap equation is exactly solved. The parameters used to describe the Sn nanoparticles are their radius (which is equal to the height measured by the STM for hemispherical particles),  $k_F = 16.2 \text{ nm}^{-1}$ ,  $E_f = 10.2 \text{ eV}$  and the coupling constant  $\lambda \sim 0.45$  [271, 295].

The calculated gap normalized with respect to the average gap of large Sn particles ( $R > 25 \text{ nm}$ ) estimated from the experimental data is plotted as a function of the height

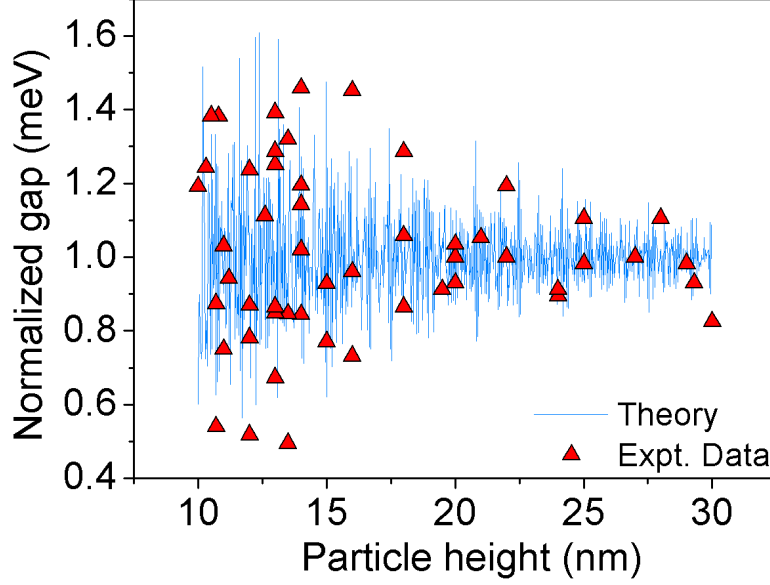


Figure 7.4: Observation of shell effects. Normalized gap (with respect to the measured gap for large particles  $\sim 0.7$  meV) vs. particle height. The solid symbols are obtained from the experimental data and the solid line is obtained from the theoretical calculations. Huge oscillations in the gap predicted due to the occurrence of shell effects.

of the particles in figure 7.4. One observes a strong dependence of the  $\Delta$  with particle size. There are huge oscillations in the gap values with variations of around  $\pm 50\%$  for particle sizes below 20 nm. For comparison with the experimental results, the data from figure 7.3 is replotted again in figure 7.4 (shown by solid symbols). Here the data is also normalized with respect to the gap value obtained experimentally for the large particles ( $\Delta_0 = 0.7$  meV). One obtains an excellent quantitative matching with the theoretical results, indicating that finite size corrections play a dominant role in the superconductivity of Sn nanoparticles.

In addition to the large oscillations observed in the gap, it appears that Sn nanoparticles also show  $\sim 20\%$  enhancement of the average gap with respect to bulk ( $\sim 0.57$  meV). To understand this, the finite size effects were computed for the average superconducting energy gap. Though one obtains a good qualitative description of the experimental results, there is worse quantitative matching compared with the oscillating part. Theory predicts only a  $\sim 5\%$  increase in the average gap. Speculatively that this is due to the non trivial behavior of the matrix elements. For a high symmetry nanoparticle these matrix elements are energy dependent and different from  $1/V$ , with  $V$  the volume of the

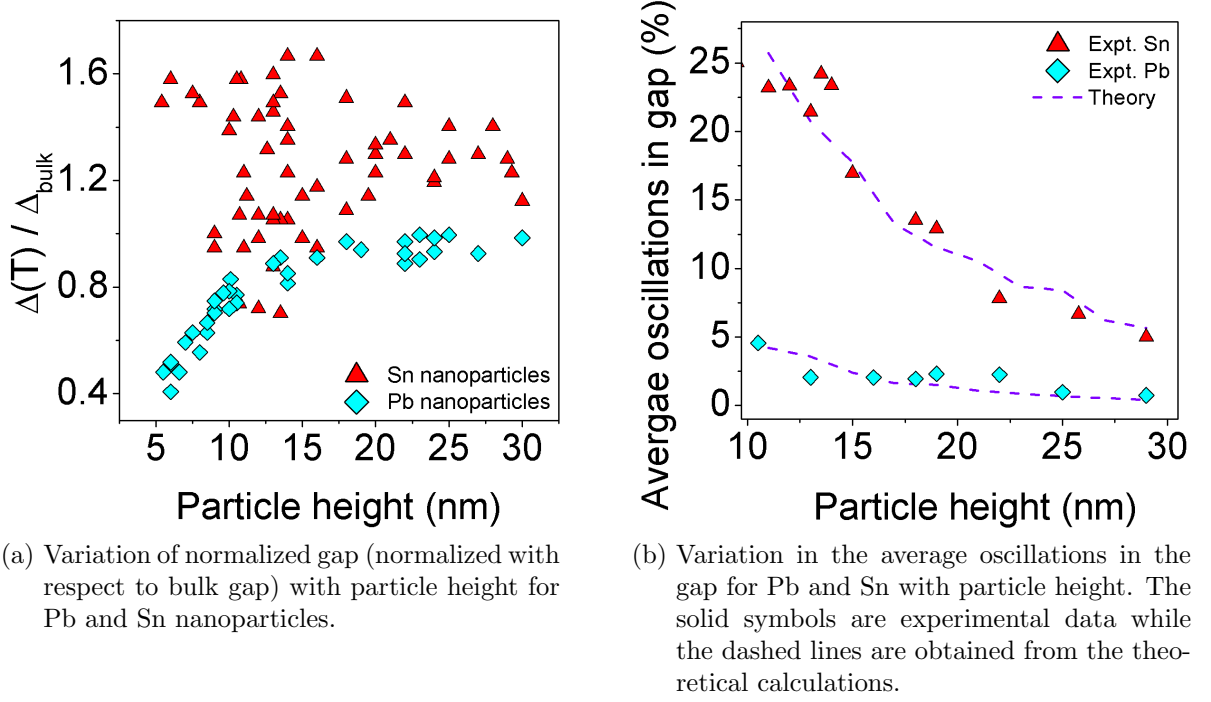


Figure 7.5: Comparison between Pb and Sn nanoparticles.

grain, even in the thermodynamic limit.

As a next step is to verify whether the oscillations in the gap seen for the Sn nanoparticles are a universal feature for small superconductors with definite symmetry. For this, the results obtained from the measurements on Pb hemispherical nanoparticles (figure 7.5a) were compared with the Sn particles. Surprisingly, no such oscillations in the gap are seen in the Pb nanoparticles, which show a monotonic decrease in  $\Delta$  with particle size. (In the plots of figure 7.5a, the gap is normalized with respect to the bulk gap value for both Sn (0.57 meV) and Pb (1.35 meV)). The reason for this striking difference is due the fact that the coherence length of Pb ( $\sim 80$  nm) is much shorter than that of Sn ( $\sim 240$  nm).

It needs to be noted that the shell effects leading to fluctuations in the spectral density close to  $E_F$  will tend to get averaged out for scales smaller than the coherence length thereby strongly suppressing the effect. On a more technical level the oscillations in the gap are suppressed in Pb because the contribution of periodic orbits longer than the coherence length to the sum in equation 7.2 is exponentially suppressed (for  $x \gg 1$  and  $K_0(x) \sim \exp(-x)$ ). The results for Pb are thus a further indication that shell effects are the reason for the oscillations observed in Sn. In figure 7.5b the average oscillations

obtained from both experiments and theory as a function of particle height are plotted for Pb and Sn nanoparticles. The average oscillations were obtained by dividing the particle size in small bins of width typically around 5 nm. The average gap and the standard deviation from this value were determined in each bin. Figure 7.5b plots the standard deviation of the gap which gives the average oscillations for a given particle size. It can clearly be seen that in both cases of Pb and Sn, equation 7.2 gives a very good quantitative description of the observed average oscillations in the gap.

In summary, the existence of shell effects is experimentally verified in small superconducting nanoparticles with well defined symmetry which leads to huge oscillations in the superconducting energy gap with the reduction of system size. Finally, the results show that for any classical BCS superconductor with large quantum coherence lengths it is possible to enhance the superconducting energy gap by large factors ( $\sim 60\%$ ) by tuning only the particle size thereby demonstrating another rich and novel property of quantum confinement.



## 8 Summary and outlook

During the time of this thesis a low temperature scanning tunneling microscope has been further developed. It achieved sub-Kelvin performance. The base temperature decreased from 2.7 to 0.8 K, the vibrational noise could be lowered to less than 1 pm and the electronic resolution is limited by the temperature and not by electronic or radio frequency noise.

To study the electronic properties of individual nanostructures they need to be decoupled from the metallic substrate. The hexagonal boron nitride nanomesh turned out to be an ideal playground for scanning tunneling spectroscopy. That the h-BN nanomesh on Rh(111) is a continuous corrugated monolayer could be proven by two different methods: Atomically resolved STM images as well as tunneling spectroscopy. In both areas of the nanomesh, the cavities and ridges a wide band gap is present. The bias dependent apparent height measurements on a partially covered sample are in agreement with the STS measurements and the calculations by Laskowski et al.

The nanomesh's decoupling and templating capabilities have been shown in a study on small cobalt clusters. They have been grown using buffer layer assisted growth. Clusters decoupled from the substrate show an electronic gap that could be attributed to the HOMO-LUMO gap of small clusters that are still too small to be metallic. Consecutive deposition cycles result in a high filling level of the nanomesh cavities with cobalt clusters. They follow the nanomesh's structure as a template.

The possibilities of the nanomesh are not yet exploit. There are mainly two experiments that should be performed. The first is the growth of graphene on boron nitride heteroepitaxially. It has been reported by the group of Oshima [119, 120] on h-BN/Ni(111).<sup>1</sup> They did LEED, Auger and vibrational spectroscopy but no STM so far. The graphene on h-BN should have a bandgap - the missing link for graphene's way to application and large scale integration.<sup>2</sup>

---

<sup>1</sup>The use of spin polarized substrates for single layer hBN like Ni or Co is an attractive option e.g. to study the ferromagnet - superconductor proximity effects from the substrate to a superconducting particle.

<sup>2</sup>Thanks to Mike F. Crommie, from Berkeley for the vivid discussion on the topic.

The second experiment is the deposition of single molecular magnets on the nanomesh on Rh(111). There have been many attempts to deposit isolated single molecular magnets on clean surfaces without convincing results so far. Especially the most famous candidate the  $\text{Mn}_{12}$  molecule is not evaporable and has an expected blocking temperature of 3 K. The unique combination of the electro spray ion beam deposition that can soft land huge molecules and a sub Kelvin STM for the low temperature spectroscopy opens the avenue to these new experiments.

The last chapters of this thesis deals with the evolution of superconductivity in single isolated superconducting particles.

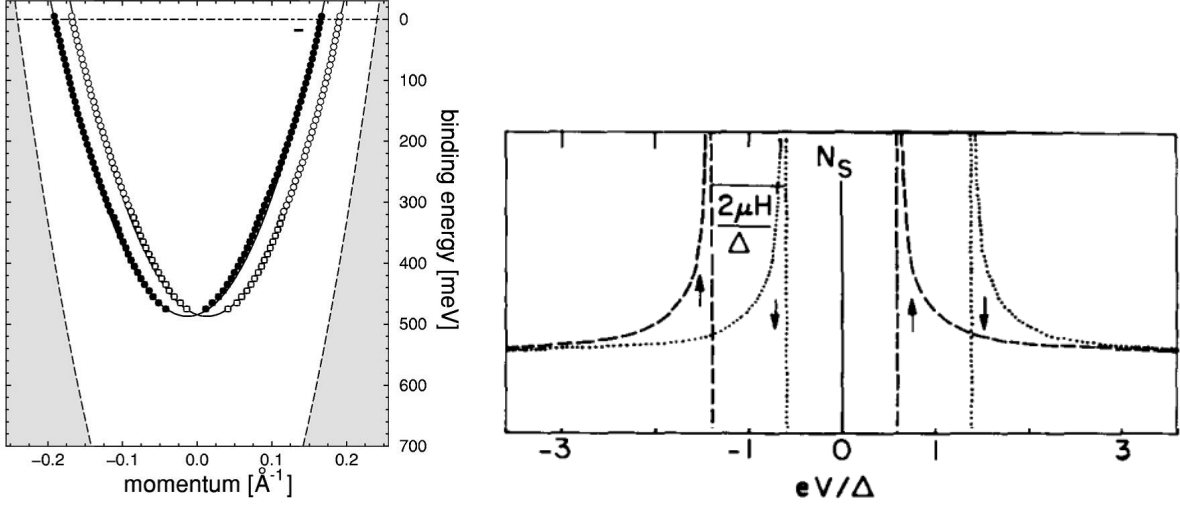
During the chase for the smallest superconductor the role of quantum fluctuations has been investigated for Pb particles. For bigger particles above 13 nm height a small decrease in the superconducting gap could be observed. For smaller particles there is a fluctuation dominated regime up to  $1.4 T_c$  demonstrating the importance of superconducting fluctuations for systems with a limited number of electrons. For very small particles below 4 nm no superconductivity could be observed.

For tin nanoparticles minor changes in the particle size lead to large variations in the superconducting energy gap for particles smaller than 20 nm. The variations can be as large as 100 % for particles of the same size. The observed oscillations of the superconducting energy gap can be described quantitatively through finite size corrections in the BCS model. Interestingly, the results on Sn are in contrast with those on Pb nanoparticles from the precedent chapter, where no such oscillations are observed. This difference is due to the comparatively shorter coherence length in Pb which suppresses the finite size corrections.

The results demonstrate that as a consequence of the shell effects the superconducting energy gap can be enhanced by approximately 60 % from its bulk value by tuning the particle size in Sn particles decoupled from the surface. The results for the tin particles confirm the assumption that proximity effects are effectively inhibited by the boron nitride nanomesh.

The superconducting particles have not been studied in a magnetic field so far. Their behavior deviates from the bulk in a magnetic field. The Ginzburg-Landau parameter, the ratio of the two characteristic lengths in superconductivity - the London penetration depth  $\lambda_L$  and the coherence length  $\xi_0$  - defines the response of the superconductor in a





(a) Spin split dispersion of the Au(111) surface state seen in photo emission spectroscopy. Image reproduced from Reinert et al. [73]. (b) Magnetic field splitting of the quasiparticle states in a superconductor. Image reproduced from Meservey et al. [58].

Figure 8.1: Spin split Au(111) surface state. Image reproduced from [73]

magnetic field.

$$\kappa = \frac{\lambda_L}{\xi_0} \quad \begin{cases} < 1/\sqrt{2} & \text{type I} \\ > 1/\sqrt{2} & \text{type II} \end{cases} \quad (8.1)$$

Both lengths alter with temperature and the effective mean free path  $l_{\text{eff}}$  (the size of the particle) [296].

$$\xi(T) \propto \sqrt{\xi_0 l_{\text{eff}} \frac{T_c}{T_c - T}} \quad \text{and} \quad \lambda_L(T) \propto \sqrt{\frac{1}{l_{\text{eff}}} \frac{T_c}{T_c - T}} \quad (8.2)$$

There is a transition from type I to type II with decreasing size where  $\kappa = 1/\sqrt{2}$ . To find this transition for nanoscale superconductors and study the behavior in the magnetic field will be a challenge in the future. Cren et al. reported this year about vortices in flat 110 nm wide Pb islands on Si(111) above 240 mT [297]. For islands smaller than the coherence length no vortices could be observed so far although the expected critical fields are huge compared to bulk type I superconductors.

Another interesting aspect of the superconducting particles is their vibrational spectrum. As mentioned in the very beginning phonon softening influences the electron-phonon coupling and has a considerable effect on  $T_c$ . Brun et al. observed phonon modes for flat lead islands on silicon [255]. The next step would be to study the phonons of superconducting particles with tunneling spectroscopy as a function of size, temperature

and coupling to the substrate.

Up to now superconductors played a role only as/on the substrate. There is another experiment where superconductors as tips are required. They were mentioned in the STM part as well as the Fourier transform scanning tunneling spectroscopy.<sup>3</sup> The idea is to combine both to measure the spin split dispersion relation of the Au(111) surface state [73, 299] (see figure 8.1a).

The initial proposal was to apply a magnetic field that would lead to a Zeeman splitting of the two spin components. Unfortunately the Zeeman splitting is small. It would require an energy resolution of less than 1 meV at 10 T. The by far easier way would be to prepare a superconducting tip by dipping it in a vanadium sample. The two spin states could be addressed at different bias voltages when a magnetic field is applied to the tip. The unavoidable Zeeman splitting of the surface state is negligible. As a result in FT-images a ring should be visible for both orientations. Their centers are expected to be offset by  $0.03 \text{ \AA}^{-1}$ .

The motivation for this thesis was to study electronic properties of individual isolated adsorbates with length scales in the regime far below the bulk. Spatial resolution and low temperatures - in order to improve the energy resolution - could be reached. The transition to nanoscale objects permits the observation of electronic properties that are not present in bulk materials. The *molecular* behavior for cobalt clusters and the *shell effects* in the tin particles as well as the *fluctuation dominated regime* in lead particles are just a few examples of exciting physics that occur merely acceding the world of nanoscale science.

---

<sup>3</sup>The latter has been used for the work on the quasiparticle chirality in epitaxial graphene that is together with image potential states on graphene not part of this thesis but published elsewhere [268, 298].

# Zusammenfassung

Im Rahmen dieser Doktorarbeit wurde am Max-Planck-Institut für Festkörperforschung ein Rastertunnelmikroskop fortentwickelt. Es handelt sich um ein Tieftemperaturmikroskop mit in situ Probentransfer unter Ultrahochvakuum. Das Mikroskop erreicht jetzt subKelvin Temperaturen im regulären Betrieb mit  $^3\text{He}$ . Die Leistungsfähigkeit des Gerätes wurde signifikant verbessert: Die Basistemperatur konnte von 2.7 auf 0.8 K gesenkt werden. Störungen im Spitze-Probe-Abstand sind auf weniger als 1 pm reduziert worden und die Energieauflösung ist nur durch die erreichte Temperatur - und nicht durch elektronisches oder Radiofrequenz-Rauschen - determiniert.

Um die elektronischen Eigenschaften individueller Nanostrukturen zu untersuchen, müssen diese vom metallischen Substrat entkoppelt sein. Das hexagonale Bornitrid-Nanomesh hat sich als ideale Spielwiese für die Rastertunnelspektroskopie erwiesen. Es konnte mit zwei Methoden nachgewiesen werden, dass das h-BN-Nanomesh auf Rh(111) eine kontinuierliche korrigierte Monolage ist. Atomar aufgelöste Bilder und Tunnelspektroskopie belegen dies. In beiden Bereichen des Nanomesh, den Erhöhungen und den Kavitäten zeigt sich eine breite elektronische Bandlücke von ca. 6 eV. Die spannungsabhängigen Messungen der scheinbaren Höhe auf partiell bedeckten Proben stimmen mit Tunnelspektroskopiemessungen und Berechnungen von Laskowski et al. überein.

Das Nanomesh vermag nicht nur Adsorbate wirkungsvoll vom Substrat zu entkoppeln, sondern dient auch als Strukturvorlage. Beides wurde anhand kleiner Kobaltcluster untersucht, die mittels Edelgaspuffer aufgewachsen wurden. Entkoppelte Cluster weisen eine elektronische Bandlücke auf, die dem Abstand zwischen dem höchsten besetzten und dem niedrigsten unbesetzten Molekülzustand entspricht. Diese Cluster sind noch zu klein, um eine metallische Bandstruktur auszubilden. Aufeinanderfolgende Aufdampfzyklen führen zu hohen Füllgraden der Nanomesh-Kavitäten mit Kobaltclustern, die der Struktur des Nanomeshs folgen.

Die letzten beiden Kapitel der Arbeit behandeln kleine voneinander isolierte, supraleitende Partikel.

Auf der Suche nach dem kleinsten Supraleiter wurde die Rolle von Quantenfluktuationen anhand von Bleipartikeln untersucht. Für Partikel mit mehr als 13 nm Höhe konnte eine leichte Verringerung der supraleitenden Bandlücke beobachtet werden. Für kleinere Partikel gibt es einen fluktuationsdominierten Bereich oberhalb der Sprungtemperatur, der sich bis zu  $1.4 T_c$  erstreckt und die Bedeutung supraleitender Fluktuationen für Systeme mit begrenzter Elektronenzahl verdeutlicht. Für sehr kleine Partikel unter 4 nm konnte keine Supraleitung beobachtet werden.

Bei Zinnnanopartikeln unter 20 nm führen geringfügige Änderungen in der Partikelgröße zu sehr großen Variationen in der supraleitenden Energielücke. Die Abweichungen können bis zu 100% für Partikel gleicher Größe betragen. Die beobachteten Oszillationen der supraleitenden Energielücke können quantitativ durch Größenkorrekturen im BCS Modell erklärt werden. Interessanterweise stehen die Ergebnisse für Zinn im Gegensatz zu den Ergebnissen für Blei aus dem vorhergehenden Kapitel. Dort wurden derartige Oszillationen nicht beobachtet. Der Unterschied erklärt sich durch die vergleichsweise kürzere Kohärenzlänge im Blei, was die Größenkorrektur im BCS-Modell unterdrückt.

# Publications

- [1] J. Zhang, V. Sessi, C.H. Michaelis, I. Brihuega, J. Honolka, K. Kern, R. Skomski, X. Chen, G. Rojas, and A. Enders. Ordered layers of Co clusters on BN template layers. *Physical Review B (Condensed Matter and Materials Physics)*, 78(16):165430, 2008. <http://dx.doi.org/10.1103/PhysRevB.78.165430>.
- [2] I. Brihuega, C.H. Michaelis, J. Zhang, S. Bose, V. Sessi, J. Honolka, M.A. Schneider, A. Enders, and K. Kern. Electronic decoupling and templating of Co nanocluster arrays on the boron nitride nanomesh. *Surface Science*, 602 (14): L95–L99, July 2008. <http://dx.doi.org/10.1016/j.susc.2008.04.040>.
- [3] I. Brihuega, P. Mallet, C. Bena, S. Bose, C. Michaelis, L. Vitali, F. Varchon, L. Magaud, K. Kern, and J.Y. Veuillen. Quasiparticle Chirality in Epitaxial Graphene Probed at the Nanometer Scale. *Physical Review Letters*, 101(20): 206802, 2008. <http://dx.doi.org/10.1103/PhysRevLett.101.206802>.
- [4] S. Bose, V.M. Silkin, R. Ohmann, I. Brihuega, L. Vitali, C.H. Michaelis, P. Mallet, J.Y. Veuillen, M.A. Schneider, E.V. Chulkov, P.M. Echenique, and K. Kern Image potential states as quantum probe of graphene interfaces. *accepted*, 2009.
- [5] I. Brihuega, S. Bose, M. Moreno, C.H. Michaelis, and K. Kern. Quantum size and Fluctuation Effects in Single Superconducting Pb Nanoparticles. *submitted.*, 2009.
- [6] S. Bose, A.M. Garcia-Garcia, M.M. Ugeda, J.D. Urbina, C.H. Michaelis, I. Brihuega, and K. Kern. Observation of 'shell effects' in superconducting nanoparticles of Sn. *submitted.*, 2009.
- [7] V. Sessi, C.H. Michaelis, K. Kuhnke, D. Vermeille, R. Felici, J. Honolka, and K. Kern. Growth of Co on atomically flat Xe layers studied by surface scattering and diffraction *in prep.*, 2010.
- [8] S. Bose, C.H. Michaelis, A.M. Garcia-Garcia, M.M. Ugeda, J.D. Urbina, I. Brihuega, and K. Kern. Strong enhancement of superconducting energy gap in isolated Sn nanoparticles: experimental demonstration of shell effects. *submitted.*, 2010.
- [9] A. Uhl, C. Michaelis, R.W. Mills, and K.D. Jandt. The influence of storage and indenter load on the Knoop hardness of dental composites polymerized with LED and halogen technologies. *DENTAL MATERIALS*, 20(1):21–28, JAN 2004. [http://dx.doi.org/10.1016/S0109-5641\(03\)00054-X](http://dx.doi.org/10.1016/S0109-5641(03)00054-X).



# References

Most of the references have a digital object identifier (DOI). In the electronic form the link <http://dx.doi.org/...> guides you directly to the full text on the publishers homepage.

- [1] H. Kamerlingh-Onnes. The resistance of pure mercury at helium temperatures. *Commun. Phys. Lab. Univ. Leiden*, 12:120, 1911.
- [2] Felix Bloch. Über die Quantenmechanik der Elektronen in Kristallgittern. *Zeitschrift für Physik A Hadrons and Nuclei*, 52:555, 1929. <http://dx.doi.org/10.1007/BF01339455>.
- [3] S. Mornet, S. Vasseur, F. Grasset, and E. Duguet. Magnetic nanoparticle design for medical diagnosis and therapy. *Journal of Materials Chemistry*, 14:2161, 2004. <http://dx.doi.org/10.1039/b402025a>.
- [4] A.N. Shipway, E. Katz, and I. Willner. Nanoparticle arrays on surfaces for electronic, optical, and sensor applications. *ChemPhysChem*, 1:18, 2000. [http://dx.doi.org/10.1002/1439-7641\(20000804\)1:1<18::AID-CPHC18>3.0.CO;2-L](http://dx.doi.org/10.1002/1439-7641(20000804)1:1<18::AID-CPHC18>3.0.CO;2-L).
- [5] J. Wiebe. *Aufbau einer 300mK-Ultrahochvakuum-Rastertunnelmikroskopie-Anlage mit 14T-Magnet und Untersuchung eines stark ungeordneten zweidimensionalen Elektronensystems*. PhD thesis, Universität Hamburg, 2003. [http://physik.uni-hamburg.de/services/fachinfo/\\_\\_\\_Volltexte/Jens\\_Bernhard\\_Reinhold\\_\\_\\_Wiebe/Jens\\_Bernhard\\_Reinhold\\_\\_\\_Wiebe.pdf](http://physik.uni-hamburg.de/services/fachinfo/___Volltexte/Jens_Bernhard_Reinhold___Wiebe/Jens_Bernhard_Reinhold___Wiebe.pdf).
- [6] J. Wiebe, A. Wachowiak, F. Meier, D. Haude, T. Foster, M. Morgenstern, and R. Wiesendanger. A 300 mK ultra-high vacuum scanning tunneling microscope for spin-resolved spectroscopy at high energy resolution. *Rev. Sci. Instrum.*, 75(11):4871, 2004. <http://dx.doi.org/10.1063/1.1794431>.
- [7] M. Kugler, C. Renner, O. Fischer, V. Mikheev, and G. Batey. A He-3 refrigerated scanning tunneling microscope in high magnetic fields and ultrahigh vacuum. *Rev. Sci. Instrum.*, 71(3):1475, 2000.
- [8] H. Kambara, T. Matsui, Y. Niimi, and H. Fukuyama. Construction of a versatile ultralow temperature scanning tunneling microscope. *Rev. Sci. Instrum.*, 78, 2007. <http://dx.doi.org/10.1063/1.2751095>.
- [9] J. Repp, G. Meyer, F.E. Olsson, and M. Persson. Controlling the charge state of individual gold adatoms. *Science*, 305(5683):493, 2004. <http://dx.doi.org/10.1126/science.1099557>.

- [10] J. Repp, G. Meyer, S.M. Stojkovic, A. Gourdon, and C. Joachim. Molecules on insulating films: Scanning-tunneling microscopy imaging of individual molecular orbitals. *Phys. Rev. Lett.*, 94(2):026803, 2005. <http://dx.doi.org/10.1103/PhysRevLett.94.026803>.
- [11] J. Repp and G. Meyer. Scanning tunneling microscopy of adsorbates on insulating films. From the imaging of individual molecular orbitals to the manipulation of the charge state. *Applied Physics A-Materials Science & Processing*, 85(4):399, 2006. <http://dx.doi.org/10.1007/s00339-006-3703-0>.
- [12] X.H. Qiu, G.V. Nazin, and W. Ho. Mechanisms of reversible conformational transitions in a single molecule. *Phys. Rev. Lett.*, 93(19):196806, 2004. <http://dx.doi.org/10.1103/PhysRevLett.93.196806>.
- [13] A.J. Heinrich, J.A. Gupta, C.P. Lutz, and D.M. Eigler. Single-atom spin-flip spectroscopy. *Science*, 306(5695):466, 2004. <http://dx.doi.org/10.1126/science.1101077>.
- [14] S. Schintke, S. Messerli, M. Pivetta, F. Patthey, L. Libioulle, M. Stengel, A. De Vita, and W.D. Schneider. Insulator at the ultrathin limit: MgO on Ag(001). *Phys. Rev. Lett.*, 87(27), 2001. <http://dx.doi.org/10.1103/PhysRevLett.87.276801>.
- [15] S. Schintke and W.D. Schneider. Insulators at the ultrathin limit: electronic structure studied by scanning tunnelling microscopy and scanning tunnelling spectroscopy. *Journal Of Physics-Condensed Matter*, 16(4):R49, 2004. <http://dx.doi.org/10.1088/0953-8984/16/4/R02>.
- [16] W. Hebenstreit, J. Redinger, Z. Horozova, M. Schmid, R. Podloucky, and P. Varga. Atomic resolution by STM on ultra-thin films of alkali halides: experiment and local density calculations. *Surf. Sci.*, 424(2-3):L321, 1999. [http://dx.doi.org/10.1016/S0039-6028\(99\)00095-3](http://dx.doi.org/10.1016/S0039-6028(99)00095-3).
- [17] J. Viernow, D.Y. Petrovykh, A. Kirakosian, J.L. Lin, F.K. Men, M. Henzler, and F.J. Himpsel. Chemical imaging of insulators by STM. *Physical Review B*, 59(15):10356, 1999. <http://dx.doi.org/10.1103/PhysRevB.59.10356>.
- [18] A. Rosenhahn, J. Schneider, J. Kandler, C. Becker, and K. Wandelt. Interaction of oxygen with Ni<sub>3</sub>Al(111) at 300 K and 1000 K. *Surf. Sci.*, 435:705, 1999. [http://dx.doi.org/10.1016/S0039-6028\(99\)00126-0](http://dx.doi.org/10.1016/S0039-6028(99)00126-0).
- [19] I. Sebastian and H. Neddermeyer. Scanning tunneling microscopy on the atomic and electronic structure of CoO thin films on Ag(100). *Surf. Sci.*, 454:771, 2000. [http://dx.doi.org/10.1016/S0039-6028\(00\)00060-1](http://dx.doi.org/10.1016/S0039-6028(00)00060-1).
- [20] G. Kresse, M. Schmid, E. Napetschnig, M. Shishkin, L. Kohler, and P. Varga. Structure of the ultrathin aluminum oxide film on NiAl(110). *Science*, 308(5727):1440, 2005. <http://dx.doi.org/10.1126/science.1107783>.



- [21] M. Corso, W. Auwarter, M. Muntwiler, A. Tamai, T. Greber, and J. Osterwalder. Boron nitride nanomesh. *Science*, 303(5655):217, 2004. <http://dx.doi.org/10.1126/science.1091979>.
- [22] J.V. Barth, G. Costantini, and K. Kern. Engineering atomic and molecular nanostructures at surfaces. *Nature*, 437(7059):671, 2005. <http://dx.doi.org/10.1038/nature04166>.
- [23] J. von Delft and D.C. Ralph. Spectroscopy of discrete energy levels in ultrasmall metallic grains. *Physics Reports-Review Section Of Physics Letters*, 345(2-3):61–173, April 2001. [http://dx.doi.org/10.1016/S0370-1573\(00\)00099-5](http://dx.doi.org/10.1016/S0370-1573(00)00099-5).
- [24] A. Bezryadin, C.N. Lau, and M. Tinkham. Quantum suppression of superconductivity in ultrathin nanowires. *Nature*, 404(6781):971, 2000. <http://dx.doi.org/10.1038/35010060>.
- [25] M.M. Ozer, Y. Jia, Z.Y. Zhang, J.R. Thompson, and H.H. Weitering. Tuning the quantum stability and superconductivity of ultrathin metal alloys. *Science*, 316(5831):1594, June 2007. <http://dx.doi.org/10.1126/science.1142159>.
- [26] A.A. Shanenko, M.D. Croitoru, M. Zgirski, F.M. Peeters, and K. Arutyunov. Size-dependent enhancement of superconductivity in Al and Sn nanowires: Shape-resonance effect. *Physical Review B*, 74, 2006. <http://dx.doi.org/10.1103/PhysRevB.74.052502>.
- [27] P.W. Anderson. Theory Of Dirty Superconductors. *J. Phys. Chem. Solids*, 11(1):26, 1959. [http://dx.doi.org/10.1016/0022-3697\(59\)90036-8](http://dx.doi.org/10.1016/0022-3697(59)90036-8).
- [28] D.C. Ralph, C.T. Black, and M. Tinkham. Spectroscopic Measurements Of Discrete Electronic States In Single Metal Particles. *Phys. Rev. Lett.*, 74(16):3241–3244, April 1995. <http://dx.doi.org/10.1103/PhysRevLett.74.3241>.
- [29] E.L. Wolf. Electron tunnelling spectroscopy. *Rep Prog Phys*, 41:1439, 1978. <http://dx.doi.org/10.1088/0034-4885/41/9/002>.
- [30] G. Binnig, H. Rohrer, C. Gerber, and E. Weibel. Tunneling Through A Controllable Vacuum Gap. *Appl. Phys. Lett.*, 40(2):178, 1982. <http://link.aip.org/link/?APPLAB/40/178/1>.
- [31] D. A. Bonnell. *Scanning probe microscopy and spectroscopy*. Wiley-VCH, New York ; Weinheim [u.a.], 2001.
- [32] R. Wiesendanger. *Scanning tunneling microscopy*. Springer, Berlin [u.a.], 1996.
- [33] J.A. Stroscio. *Scanning tunneling microscopy*. Academic Pr., Boston [u.a.], 1993.
- [34] C.J. Chen. *Introduction to scanning tunneling microscopy*. Oxford University Press, New York, second edition edition, 2007. ISBN 978-0-19-507150-4. <http://dx.doi.org/10.1093/acprof:oso/9780199211500.001.0001>.

- [35] N.D. Lang. Spectroscopy of single atoms in the scanning tunneling microscope. *Physical Review B*, 34(8):5947, 1986. <http://dx.doi.org/10.1103/PhysRevB.34.5947>.
- [36] J. Tersoff and D.R. Hamann. Theory and Application for the Scanning Tunneling Microscope. *Phys. Rev. Lett.*, 50(25):1998–2001, 1983. <http://dx.doi.org/10.1103/PhysRevLett.50.1998>.
- [37] J. Tersoff and D.R. Hamann. Theory of the scanning tunneling microscope. *Physical Review B*, 31(2):805, 1985. <http://dx.doi.org/10.1103/PhysRevB.31.805>.
- [38] W.A. Hofer, A.S. Foster, and A.L. Shluger. Theories of scanning probe microscopes at the atomic scale. *Reviews Of Modern Physics*, 75:1287, 2003. <http://dx.doi.org/10.1103/RevModPhys.75.1287>.
- [39] J. Bardeen. Tunnelling from a Many-Particle Point of View. *Phys. Rev. Lett.*, 6: 57, 1961. <http://dx.doi.org/10.1103/PhysRevLett.6.57>.
- [40] M. Buttiker, Y. Imry, R. Landauer, and S. Pinhas. Generalized many-channel conductance formula with application to small rings. *Physical Review B*, 31(10): 6207, 1985. <http://dx.doi.org/10.1103/PhysRevB.31.6207>.
- [41] J. Cerda, M.A. Van Hove, P. Sautet, and M. Salmeron. Efficient method for the simulation of STM images. I. Generalized Green-function formalism. *Physical Review B*, 56(24):15885, 1997. <http://dx.doi.org/10.1103/PhysRevB.56.15885>.
- [42] L.V. Keldysh. Diagram Technique for nonequilibrium Processes. *Soviet Physics JETP-USSR*, 20(4):1018, 1965.
- [43] M. Brandbyge, J.L. Mozos, P. Ordejon, J. Taylor, and K. Stokbro. Density-functional method for nonequilibrium electron transport. *Physical Review B*, 65 (16), 2002. <http://dx.doi.org/10.1103/PhysRevB.65.165401>.
- [44] T.K. Pratt and R. Williams. Non-linear analysis of slip-stick motion. *Journal of Sound and Vibration*, 74(4):531, 1981. [http://dx.doi.org/10.1016/0022-460X\(81\)90417-X](http://dx.doi.org/10.1016/0022-460X(81)90417-X).
- [45] K. Besocke. An Easily Operable Scanning Tunneling Microscope. *Surf. Sci.*, 181 (1-2):145, 1987. [http://dx.doi.org/10.1016/0039-6028\(87\)90151-8](http://dx.doi.org/10.1016/0039-6028(87)90151-8).
- [46] S.H. Pan, E.W. Hudson, and J.C. Davis. He-3 refrigerator based very low temperature scanning tunneling microscope. *Rev. Sci. Instrum.*, 70(2):1459, 1999. <http://dx.doi.org/10.1063/1.1149605>.
- [47] S. Katzir. The discovery of the piezoelectric effect. *Archive for History of Exact Sciences*, 57(1):61, 2003. <http://dx.doi.org/10.1007/s00407-002-0059-5>.

- [48] J. Bechhoefer. Feedback for physicists: A tutorial essay on control. *Reviews of Modern Physics*, 77(3):783–836, JUL 2005. <http://dx.doi.org/10.1103/RevModPhys.77.783>.
- [49] M.F. Crommie, C.P. Lutz, and D.M. Eigler. Confinement of Electrons to Quantum Corrals on a Metal Surface. *Science*, 262:218, 1993. <http://dx.doi.org/10.1126/science.262.5131.218>.
- [50] W.A. Hofer. Challenges and errors: interpreting high resolution images in scanning tunneling microscopy. *Prog. Surf. Sci.*, 71:147, 2003. [http://dx.doi.org/10.1016/S0079-6816\(03\)00005-4](http://dx.doi.org/10.1016/S0079-6816(03)00005-4).
- [51] R. Temirov, S. Soubatch, O. Neucheva, A.C. Lassise, and F.S. Tautz. A novel method achieving ultra-high geometrical resolution in scanning tunnelling microscopy. *New Journal of Physics*, 10:053012, 2008. <http://stacks.iop.org/1367-2630/10/053012>.
- [52] L. Gross, F. Mohn, N. Moll, P. Liljeroth, and G. Meyer. The Chemical Structure of a Molecule Resolved by Atomic Force Microscopy. *Science*, 325:1110, 2009. <http://dx.doi.org/10.1126/science.1176210>.
- [53] M. Bode. Spin-polarized scanning tunnelling microscopy. *Reports on Progress in Physics*, 66:523, 2003. <http://dx.doi.org/10.1088/0034-4885/66/4/203>.
- [54] F. Meier, L. Zhou, J. Wiebe, and R. Wiesendanger. Revealing magnetic interactions from single-atom magnetization curves. *Science*, 320:82, 2008. <http://dx.doi.org/10.1126/science.1154415>.
- [55] A. Kohen, Y. Noat, T. Proslier, E. Lacaze, M. Aprili, W. Sacks, and D. Roditchev. Fabrication and characterization of scanning tunneling microscopy superconducting Nb tips having highly enhanced critical fields. *Physica C: Superconductivity*, 419:18, 2005. <http://dx.doi.org/10.1016/j.physc.2004.12.001>.
- [56] S.H. Pan, E.W. Hudson, and J.C. Davis. Vacuum tunneling of superconducting quasiparticles from atomically sharp scanning tunneling microscope tips. *Applied Physics Letters*, 73:2992, 1998. <http://dx.doi.org/10.1063/1.122654>.
- [57] Y. Uehara, T. Fujita, M. Iwami, and S. Ushioda. Superconducting niobium tip for scanning tunneling microscope light emission spectroscopy. *Rev. Sci. Instrum.*, 72:2097, 2001. <http://dx.doi.org/10.1063/1.1350644>.
- [58] R. Meservey and P.M. Tedrow. Spin-polarized electron tunnel. *Physics Reports-Review Section Of Physics Letters*, 238:173–243, 1994.
- [59] B.C. Stipe, M.A. Rezaei, and W. Ho. Single-molecule vibrational spectroscopy and microscopy. *Science*, 280:1732, 1998. <http://dx.doi.org/10.1126/science.280.5370.1732>.

- [60] B.C. Stipe, H.A. Rezaei, and W. Ho. Localization of inelastic tunneling and the determination of atomic-scale structure with chemical specificity. *Physical Review Letters*, 82:1724, 1999. <http://dx.doi.org/10.1103/PhysRevLett.82.1724>.
- [61] H. Gawronski, M. Mehlhorn, and K. Morgenstern. Imaging phonon excitation with atomic resolution. *Science*, 319:930, 2008. <http://dx.doi.org/10.1126/science.1152473>.
- [62] L. Petersen, P.T. Sprunger, P. Hofmann, E. Laegsgaard, B.G. Briner, M. Doering, H.P. Rust, A.M. Bradshaw, F. Besenbacher, and E.W. Plummer. Direct imaging of the two-dimensional Fermi contour: Fourier-transform STM. *Physical Review B*, 57:R6858, 1998. <http://dx.doi.org/10.1103/PhysRevB.57.R6858>.
- [63] O. Jeandupeux, L. Burgi, H. Hirstein, A. and Brune, and K. Kern. Thermal damping of quantum interference patterns of surface-state electrons. *Physical Review B*, 59:15926, 1999. <http://dx.doi.org/10.1103/PhysRevB.59.15926>.
- [64] L. Bürgi. *Scanning Tunneling Microscopy as Local Probe of Electron Density, Dynamics, and Transport at Metal Surfaces*. PhD thesis, EPFL Lausanne, Switzerland, 1999.
- [65] R.M. Feenstra, J.A. Stroscio, J. Tersoff, and A.P. Fein. Atom-Selective Imaging of the GaAs(110) Surface. *Physical Review Letters*, 58:1192, 1987. <http://dx.doi.org/10.1103/PhysRevLett.58.1192>.
- [66] F.J. Giessibl. Advances in atomic force microscopy. *Rev. Mod. Phys.*, 75:949, 2003. <http://dx.doi.org/10.1103/RevModPhys.75.949>.
- [67] G. Wittich. *Scanning Tunneling Microscopy and Spectroscopy at Low Temperatures: Development of a 1 K-Instrument and Local Characterization of Heterogenous Metal Systems*. PhD thesis, University of Konstanz, Konstanz, Germany, 2005. <http://www.ub.uni-konstanz.de/kops/volltexte/2005/1669/pdf/dissertation.pdf>.
- [68] R. Hamers. *Interaction of Radiation with Surfaces and Electron Tunneling in Landolt-Börnstein - Group III Condensed Matter*. Springer, 2006. [http://dx.doi.org/10.1007/10119615\\_61](http://dx.doi.org/10.1007/10119615_61).
- [69] F. Paschen. Ueber die zum Funkenübergang in Luft, Wasserstoff und Kohlensäure bei verschiedenen Drucken erforderliche Potentialdifferenz. *Annalen der Physik*, 273(5):69, 1889. <http://dx.doi.org/10.1002/andp.18892730505>.
- [70] F. Rosebury. *Handbook of electron tube and vacuum techniques*. Springer, 1993.
- [71] Verein Deutscher Eisenhüttenleute, editor. *Steel - Fundamentals and Applications*. Springer, Berlin, Heidelberg u.a., 1993.

- [72] J. Klier, R. Berndt, E.V. Chulkov, V.M. Silkin, P.M. Echenique, and S. Crampin. Dimensionality effects in the lifetime of surface states. *Science*, 288:1399, 2000. <http://dx.doi.org/10.1126/science.288.5470.1399>.
- [73] F. Reinert, G. Nicolay, S. Schmidt, D. Ehm, and S. Hufner. Direct measurements of the L-gap surface states on the (111) face of noble metals by photoelectron spectroscopy. *Physical Review B*, 63(11):115415, 2001. <http://dx.doi.org/10.1103/PhysRevB.63.115415>.
- [74] J.E. Hoffman. *A Search for Alternative Electronic Order in the High Temperature Superconductor Bi<sub>2</sub>Sr<sub>2</sub>CaCu<sub>2</sub>O<sub>8</sub>+d by Scanning Tunneling Microscopy*. PhD thesis, University of California, Berkely, 2003. <http://physics.harvard.edu/~jhoffman/thesis/HoffmanThesis.pdf>.
- [75] K.W. Taconis, J.J.M. Beenakker, A.O.C. Nier, and L.T. Aldrich. Measurements concerning the vapour-liquid equilibrium of solutions of He<sup>3</sup> in He<sup>4</sup> below 2.19K. *Physica*, 15:733, 1949. [http://dx.doi.org/10.1016/0031-8914\(49\)90078-6](http://dx.doi.org/10.1016/0031-8914(49)90078-6).
- [76] H.P. Rust, M. Doering, J.I. Pascual, T.P. Pearl, and P.S. Weiss. Temperature control of a liquid helium cooled Eigler-style scanning tunneling microscope. *Rev. Sci. Instrum.*, 72:4393, 2001. <http://dx.doi.org/10.1063/1.1416108>.
- [77] F. Pobell. *Matter and Methods at Low Temperatures*. Springer, Berlin, Heidelberg, 3rd edition, 2007.
- [78] C. Debuschewitz. *Spektroskopische Untersuchungen von Proximity-Systemen : Aufbau eines 300-mK-Rastertunnelmikroskops mit hoher Energieauflösung und Untersuchungen der Zustandsdichte am System Aluminium/Gold*. PhD thesis, Universität Konstanz, 2008. <http://nbn-resolving.de/urn:nbn:de:bsz:352-opus-60004>.
- [79] H. le Sueur. *Cryogenic AFM-STM for mesoscopic physics*. PhD thesis, Universite Pierre et Marie Curie - Paris VI, 2007. <http://tel.archives-ouvertes.fr/tel-00261434/en/>.
- [80] G.A. Slack, R.A. Tanzilli, R.O. Pohl, and J.W. Vandersande. The intrinsic thermal conductivity of AlN. *Journal of Physics and Chemistry of Solids*, 48:641, 1987. [http://dx.doi.org/10.1016/0022-3697\(87\)90153-3](http://dx.doi.org/10.1016/0022-3697(87)90153-3).
- [81] H.M. Rosenberg. The Thermal Conductivity of Metals at Low Temperatures. *Philosophical Transactions of the Royal Society of London. Series A, Mathematical and Physical Sciences*, 247:441, 1955. <http://www.jstor.org/stable/91541>.
- [82] A. Waleh and N.H. Zebouni. Study of Supercooling and Thermal Conductivity in Superconducting Molybdenum. *Physical Review B*, 4:2977, 1971. <http://dx.doi.org/10.1103/PhysRevB.4.2977>.

- [83] P. Kapitza. Viscosity of Liquid Helium below the  $\lambda$ -Point. *Nature*, 141:74, 1938. <http://dx.doi.org/10.1038/141074a0>.
- [84] P.V.E. McClintock, D.J. Meredith, and J.K. Wigmore. *Matter at low temperatures*. Blackie, Glasgow, 1984.
- [85] G. K. White and P. J. Meeson. *Experimental techniques in low-temperature physics*. Clarendon Press, Oxford, 4. edition, 2002.
- [86] J.G. Weisend, editor. *Handbook of cryogenic engineering*. Taylor & Francis, Washington, DC, 1998.
- [87] C.A. Bailey, editor. *Advanced cryogenics*. Plenum Pr., London, 1971.
- [88] R.C. Richardson, editor. *Experimental techniques in condensed matter physics at low temperatures*. Addison Wesley, Redwood City, CA, 1988.
- [89] L.J. Lauhon and W. Ho. Effects of temperature and other experimental variables on single molecule vibrational spectroscopy with the scanning tunneling microscope. *Rev. Sci. Instrum.*, 72:216, 2001. <http://dx.doi.org/10.1063/1.1327311>.
- [90] R. Morrisson. *Grounding and Shielding Techniques*. Wiley, New York, 1998.
- [91] H.W. Ott. *Noise Reduction Techniques in Electronic Systems*. John Wiley & Sons, 1988.
- [92] H. Suderow, P. Martinez-Samper, N. Luchier, J.P. Brison, S. Vieira, and P.C. Canfield. Tunneling spectroscopy in the magnetic superconductor *TmNi<sub>2</sub>B<sub>2</sub>C*. *Phys. Rev. B*, 64:020503, 2001. <http://dx.doi.org/10.1103/PhysRevB.64.020503>.
- [93] K. Bladh, D. Gunnarsson, E. Hurfeld, S. Devi, C. Kristoffersson, B. Smalander, S. Pehrson, T. Claeson, P. Delsing, and M. Taslakov. Comparison of cryogenic filters for use in single electronics experiments. *Rev. Sci. Instrum.*, 74:1323, 2003. <http://dx.doi.org/10.1063/1.1540721>.
- [94] D.C. Glattli, P. Jacques, A. Kumar, P. Pari, and L. Saminadayar. A noise detection scheme with 10 mK noise temperature resolution for semiconductor single electron tunneling devices. *J. Appl. Phys.*, 81:7350, 1997. <http://dx.doi.org/10.1063/1.365332>.
- [95] A.B. Williams and F.J. Taylor. *Electronic Filter Design Handbook*. McGraw-Hill, fourth edition, 2006.
- [96] S. Rauschenbach, F.L. Stadler, E. Lunedei, N. Malinowski, S. Koltsov, G. Costantini, and K. Kern. Electrospray ion beam deposition of clusters and biomolecules. *Small*, 2(4):540, 2006. <http://dx.doi.org/10.1002/smll.200500479>.

- [97] S. Rauschenbach. *Electrospray Ion Beam Deposition and Mass Spectrometry of Nonvolatile Molecules and Nanomaterials*. PhD thesis, EPFL, Lausanne, Switzerland, 2007. <http://library.epfl.ch/theses/?nr=3958>.
- [98] G. Firpo, F.B. de Mongeot, C. Boragno, and U. Valbusa. High performance portable vacuum suitcase. *Rev. Sci. Instrum.*, 76, 2005. <http://dx.doi.org/10.1063/1.1834493>.
- [99] S. Olthof. Rastertunnelmikroskopie und -spektroskopie an Halbleiternanostrukturen. Master's thesis, University of Stuttgart, 2006.
- [100] C. Rajadurai, Z. Qu, O. Fuhr, B. Gopalan, R. Kruk, M. Ghafari, and M. Ruben. Lattice-solvent controlled spin transitions in iron(II) complexes. *Dalton Trans.*, (32):3531, 2007. <http://dx.doi.org/10.1039/b703700g>.
- [101] K. Watanabe, T. Taniguchi, and H. Kanda. Direct-bandgap properties and evidence for ultraviolet lasing of hexagonal boron nitride single crystal. *Nat. Mater.*, 3(6):404, 2004. <http://dx.doi.org/10.1038/nmat1134>.
- [102] H. Ma, S.H. Lin, R.W. Carpenter, P. Rice, and O.F. Sankey. Ab initio calculation of band structure, x-ray emission, quantum yield, and electron-energy-loss spectra of hexagonal boron nitride. *Journal of Applied Physics*, 73:7422, 1993. <http://dx.doi.org/10.1063/1.353983>.
- [103] Z. Liu and T.B. Marder. B-N versus C-C: How similar are they? *Angewandte Chemie-International Edition*, 47(2):242, 2008. <http://dx.doi.org/10.1002/anie.200703535>.
- [104] R. Haubner, M. Wilhelm, R. Weissenbacher, and B. Lux. Boron nitrides - Properties, synthesis and applications. In *High Performance Non-Oxide Ceramics II*, volume 102 of *Structure and Bonding*, pages 1–45. Springer Berlin / Heidelberg, 2002. [http://dx.doi.org/10.1007/3-540-45623-6\\_1](http://dx.doi.org/10.1007/3-540-45623-6_1).
- [105] T. Oku, T. Hirano, M. Kuno, T. Kusunose, K. Niihara, and K. Suganuma. Synthesis, atomic structures and properties of carbon and boron nitride fullerene materials. *Materials Science and Engineering B*, 74:206, 2000. [http://dx.doi.org/10.1016/S0921-5107\(99\)00563-2](http://dx.doi.org/10.1016/S0921-5107(99)00563-2).
- [106] E. Bengu and L.D. Marks. Single-walled BN nanostructures. *Phys. Rev. Lett.*, 86(11):2385, 2001. <http://dx.doi.org/10.1103/PhysRevLett.86.2385>.
- [107] N.G. Chopra, R.J. Luyken, K. Cherry, V.H. Crespi, M.L. Cohen, S.G. Louie, and A. Zettl. Boron-Nitride Nanotubes. *Science*, 269:966, 1995. <http://dx.doi.org/10.1126/science.269.5226.966>.
- [108] T. Brugger, S. Günther, B. Wang, J.H. Dil, M. Bocquet, J. Osterwalder, J. Winterlin, and T. Greber. Comparison of electronic structure and template function

- of single-layer graphene and a hexagonal boron nitride nanomesh on Ru(0001). *Physical Review B*, 79:045407, 2009. <http://dx.doi.org/10.1103/PhysRevB.79.045407>. <http://link.aps.org/abstract/PRB/v79/e045407>.
- [109] A. Goriachko and H. Over. Modern Nanotemplates Based on Graphene and Single Layer h-BN. *Zeitschrift für Physikalische Chemie - International journal of research in physical chemistry and chemical physics*, 223:157, 2009. <http://dx.doi.org/10.1524/zpch.2009.6030>.
  - [110] O. Hassel. Über die Kristallstruktur des Graphits. *Zeitschrift für Physik*, 25:317, 1924. <http://cod.ibt.lt/cif/1/1011060.cif>.
  - [111] A. Brager. An X-Ray Examination of the Structure of Boron Nitride. *Acta Physicochimica (USSR)*, 7:699, 1937. <http://cod.ibt.lt/cif/1/1010602.cif>.
  - [112] Cambridge Crystallographic Data Centre. Mercury 1.42, 2009. [http://www.ccdc.cam.ac.uk/free\\_services/mercury/](http://www.ccdc.cam.ac.uk/free_services/mercury/).
  - [113] S.V. Nguyen, T. Nguyen, H. Treichel, and O. Spindler. Plasma-Assisted Chemical Vapor Deposition and Characterization of Boron Nitride Films. *J. Electrochem. Soc.*, 141:1633, 1994. <http://dx.doi.org/10.1149/1.2054974>.
  - [114] A. Nagashima, N. Tejima, and C. Oshima. Electronic states of the pristine and alkali-metal-intercalated monolayer graphite/Ni(111) systems. *Phys. Rev. B*, 50:17487, 1994. <http://dx.doi.org/10.1103/PhysRevB.50.17487>.
  - [115] C. Oshima and A. Nagashima. Ultra-thin epitaxial films of graphite and hexagonal boron nitride on solid surfaces. *Journal of Physics-Condensed Matter*, 9:1, 1997. <http://dx.doi.org/10.1088/0953-8984/9/1/004>.
  - [116] A. Nagashima, N. Tejima, Y. Gamou, T. Kawai, and C. Oshima. Electronic-Structure Of Monolayer Hexagonal Boron-Nitride Physisorbed On Metal-Surfaces. *Phys. Rev. Lett.*, 75:3918, 1995. <http://dx.doi.org/10.1103/PhysRevLett.75.3918>.
  - [117] A. Nagashima, N. Tejima, Y. Gamou, T. Kawai, and C. Oshima. Electronic Dispersion-Relations of Monolayer Hexagonal Boron-Nitride formed on the Ni(111) Surface. *Physical Review B*, 51:4606, 1995. <http://dx.doi.org/10.1103/PhysRevB.51.4606>.
  - [118] E. Rokuta, Y. Hasegawa, K. Suzuki, Y. Gamou, C. Oshima, and A. Nagashima. Phonon dispersion of an epitaxial monolayer film of hexagonal boron nitride on Ni(111). *Phys. Rev. Lett.*, 79(23):4609, 1997. <http://dx.doi.org/10.1103/PhysRevLett.79.4609>.
  - [119] A. Nagashima, Y. Gamou, M. Terai, M. Wakabayashi, and C. Oshima. Electronic states of the heteroepitaxial double-layer system: Graphite/monolayer hexagonal



- boron nitride/Ni(111). *Physical Review B*, 54(19):13491, 1996. <http://dx.doi.org/10.1103/PhysRevB.54.13491>.
- [120] T. Tanaka, A. Ito, A. Tajima, E. Rokuta, and C. Oshima. Heteroepitaxial film of monolayer graphene/monolayer h-BN on Ni(111). *Surface Review and Letters*, 10(5):721, 2003. <http://dx.doi.org/10.1142/S0218625X03005529>.
  - [121] T. Tanaka, A. Itoh, K. Yamashita, E. Rokuta, and C. Oshima. Heteroepitaxial system of h-BN/monolayer graphene on Ni(111). *Surface Review and Letters*, 10: 697, 2003.
  - [122] W. Auwarter, T. J. Kreutz, T. Greber, and J. Osterwalder. XPD and STM investigation of hexagonal boron nitride on Ni(111). *Surf. Sci.*, 429(1):229, 1999. [http://dx.doi.org/10.1016/S0039-6028\(99\)00381-7](http://dx.doi.org/10.1016/S0039-6028(99)00381-7).
  - [123] W. Auwarter, M. Muntwiler, T. Greber, and J. Osterwalder. Co on h-BN/Ni(111): from island to island-chain formation and Co intercalation. *Surf. Sci.*, 511:379–386, 2002. [http://dx.doi.org/10.1016/S0039-6028\(02\)01545-5](http://dx.doi.org/10.1016/S0039-6028(02)01545-5).
  - [124] W. Auwarter. *One Monolayer of Hexagonal Boron Nitride on Ni(111): an Atomically Sharp Interface*. PhD thesis, Universität Zürich, 2003.
  - [125] C. Becker and K. Wandelt. Surfaces: Two-Dimensional Templates. In *Templates in Chemistry III*, volume 287 of *Topics in Current Chemistry*, pages 45–86. Springer, Berlin, 2009. [http://dx.doi.org/10.1007/128\\_2008\\_151](http://dx.doi.org/10.1007/128_2008_151).
  - [126] H. Brune, M. Giovannini, K. Bromann, and K. Kern. Self-organized growth of nanostructure arrays on strain-relief patterns. *Nature*, 394:451, 1998. <http://dx.doi.org/10.1038/28804>.
  - [127] V. Holy, G. Springholz, M. Pinczolis, and G. Bauer. Strain induced vertical and lateral correlations in quantum dot superlattices. *Phys. Rev. Lett.*, 83(2):356, 1999. <http://dx.doi.org/10.1103/PhysRevLett.83.356>.
  - [128] J. Zhang, V. Sessi, C.H. Michaelis, I. Brihuega, J. Honolka, K. Kern, R. Skomski, X. Chen, G. Rojas, and A. Enders. Ordered layers of Co clusters on BN template layers. *Physical Review B*, 78:165430, 2008. <http://dx.doi.org/10.1103/PhysRevB.78.165430>.
  - [129] R. Bennewitz. Structured surfaces of wide band gap insulators as templates for overgrowth of adsorbates. *JOURNAL OF PHYSICS-CONDENSED MATTER*, 18(26):R417., 2006. <http://dx.doi.org/10.1088/0953-8984/18/26/R01>.
  - [130] M. Vogelgesang. *Ultrathin KCl films on Cu(110) and Cu(111) studied by low-temperature scanning tunneling microscopy*. PhD thesis, EPFL, Lausanne, Switzerland, 2005. <http://library.epfl.ch/theses/?nr=3352&lang=ger>.

- [131] K. Glocker, M. Sokolowski, A. Soukopp, and E. Umbach. Initial growth of insulating overlayers of NaCl on Ge(100) observed by scanning tunneling microscopy with atomic resolution. *Physical Review B*, 54(11):7705, 1996. <http://dx.doi.org/10.1103/PhysRevB.54.7705>.
- [132] A. Klust, T. Ohta, A.A. Bostwick, E. Rotenberg, Q.M. Yu, F.S. Ohuchi, and M.A. Olmstead. Electronic structure evolution during the growth of ultrathin insulator films on semiconductors: From interface formation to bulklike CaF<sub>2</sub>/Si(111) films. *Physical Review B*, 72, 2005. <http://dx.doi.org/10.1103/PhysRevB.72.205336>.
- [133] S.C. Street, C. Xu, and D.W. Goodman. The physical and chemical properties of ultrathin oxide films. *Annu. Rev. Phys. Chem.*, 48:43, 1997. <http://dx.doi.org/10.1146/annurev.physchem.48.1.43>.
- [134] M. Ritter, W. Ranke, and W. Weiss. Growth and structure of ultrathin FeO films on Pt(111) studied by STM and LEED. *Physical Review B*, 57(12):7240, 1998. <http://dx.doi.org/10.1103/PhysRevB.57.7240>.
- [135] J. Libuda, F. Winkelmann, M. Baumer, H.J. Freund, T. Bertrams, H. Neddermeyer, and K. Muller. Structure and defects of an ordered alumina film on NiAl(110). *Surf. Sci.*, 318:61, 1994. [http://dx.doi.org/10.1016/0039-6028\(94\)90341-7](http://dx.doi.org/10.1016/0039-6028(94)90341-7).
- [136] G. Ceballos, Z. Song, J.I. Pascual, H.P. Rust, H. Conrad, M. Baumer, and H.J. Freund. Structure investigation of the topmost layer of a thin ordered alumina film grown on NiAl(110) by low temperature scanning tunneling microscopy. *Chem. Phys. Lett.*, 359:41, 2002. [http://dx.doi.org/10.1016/S0009-2614\(02\)00578-X](http://dx.doi.org/10.1016/S0009-2614(02)00578-X).
- [137] T. Maroutian, S. Degen, C. Becker, K. Wandelt, and R. Berndt. Superstructures and coincidences of a thin oxide film on a metallic substrate: A STM study. *Physical Review B*, 68(15), 2003. <http://dx.doi.org/10.1103/PhysRevB.68.155414>.
- [138] C. Hagendorf, R. Shantyr, K. Meinel, K. M. Schindler, and H. Neddermeyer. Scanning tunneling microscopy and spectroscopy investigation of the atomic and electronic structure of CoO islands on Ag(001). *Surf. Sci.*, 532:346, 2003. [http://dx.doi.org/10.1016/S0039-6028\(03\)00192-4](http://dx.doi.org/10.1016/S0039-6028(03)00192-4).
- [139] Y. Z. Wu, A. K. Schmid, and Z. Q. Qiu. Spin-dependent quantum interference from epitaxial MgO thin films on Fe(001). *Phys. Rev. Lett.*, 97(21), 2006. <http://dx.doi.org/10.1103/PhysRevLett.97.217205>.
- [140] L. P. Zhang, M. Kuhn, and U. Diebold. Growth, structure and thermal properties of chromium oxide films on Pt(111). *Surf. Sci.*, 375(1):1, 1997. [http://dx.doi.org/10.1016/S0039-6028\(96\)01256-3](http://dx.doi.org/10.1016/S0039-6028(96)01256-3).

- [141] F. M. Leibsle, S. S. Dhesi, S. D. Barrett, and A. W. Robinson. STM observations of Cu(100)-c(2x2)N surfaces: evidence for attractive interactions and an incommensurate c(2x2) structure. *Surface Science*, 317(3):309, 1994. [http://dx.doi.org/10.1016/0039-6028\(94\)90287-9](http://dx.doi.org/10.1016/0039-6028(94)90287-9).
- [142] R. Widmer, S. Berner, O. Groning, T. Brugger, E. Osterwalder, and T. Greber. Electrolytic in situ STM investigation of h-BN-nanomesh. *Electrochem. Commun.*, 9(10):2484, 2007. <http://dx.doi.org/10.1016/j.elecom.2007.07.019>.
- [143] S. Berner, M. Corso, R. Widmer, O. Groening, R. Laskowski, P. Blaha, K. Schwarz, A. Goriachko, H. Over, S. Gsell, M. Schreck, H. Sachdev, T. Greber, and J. Osterwalder. Boron nitride nanomesh: Functionality from a corrugated monolayer. *Angewandte Chemie-International Edition*, 46(27):5115, 2007. <http://dx.doi.org/10.1002/anie.200700234>.
- [144] O. Bunk, M. Corso, D. Martoccia, R. Herger, P. R. Willmott, B. D. Patterson, J. Osterwalder, I. van der Veen, and T. Greber. Surface X-ray diffraction study of boron-nitride nanomesh in air. *Surf. Sci.*, 601(2):L7, 2007. <http://dx.doi.org/10.1016/j.susc.2006.11.018>.
- [145] M. Gsell, P. Jakob, and D. Menzel. Effect of substrate strain on adsorption. *Science*, 280(5364):717, 1998. <http://dx.doi.org/10.1126/science.280.5364.717>.
- [146] F. Mueller, S. Huefner, and H. Sachdev. Epitaxial growth of boron nitride on a Rh(111) multilayer system: Formation and fine tuning of a BN-nanomesh. *Surf. Sci.*, 603(3):425, 2009. <http://dx.doi.org/10.1016/j.susc.2008.10.033>.
- [147] G. Mamantov and J.L. Margrave. Decomposition of liquid borazine. *Journal of Inorganic and Nuclear Chemistry*, 20:348, 1961. [http://dx.doi.org/10.1016/0022-1902\(61\)80289-3](http://dx.doi.org/10.1016/0022-1902(61)80289-3).
- [148] T. Wideman and L.G. Sneddon. Convenient Procedures for the Laboratory Preparation of Borazine. *Inorg. Chem.*, 34:1002, 1995. <http://dx.doi.org/10.1021/ic00108a039>.
- [149] K.T. Moon, D.S. Min, and D.P. Kim. A route to boron nitride via simply prepared borazine precursor. *Bulletin of the Korean Chemical Society*, 19:222, 1998. <http://journal.kcsnet.or.kr/>.
- [150] C.A. Jaska, K. Temple, A.J. Lough, and I. Manners. Transition metal-catalyzed formation of boron-nitrogen bonds: Catalytic dehydrocoupling of amine-borane adducts to form aminoboranes and borazines. *J. Am. Chem. Soc.*, 125:9424, 2003. <http://dx.doi.org/10.1021/ja0301601>.
- [151] G. Dong, E.B. Fourre, F.C. Tabak, and J.W.M. Frenken. Formation of Boron Nitride Nanomesh on Rh(111). Poster-photo: High temperature STM study of borazine adsorption and nanomesh formation, 2009.

- [152] V.N. Demin, I.P. Asanov, and Z.L. Akkerman. Chemical vapor deposition of pyrolytic boron nitride from borazine. *J. Vac. Sci. Technol. A*, 18:94, 2000. <http://dx.doi.org/10.1116/1.582124>.
- [153] J.A. Rodriguez, C.M. Truong, and D.W. Goodman. Synthesis of boron nitride ultrathin films: The bonding and chemistry of ammonia and hydrazine on Ru(0001) and B/Ru(0001) surfaces. *J. Vac. Sci. Technol. A*, 10:955, 1992. <http://dx.doi.org/10.1116/1.577885>.
- [154] R.M. Desrosiers, D.W. Greve, and A.J. Gellman. Nucleation of boron nitride thin films on Ni(100). *Surf. Sci.*, 382:35, 1997. [http://dx.doi.org/10.1016/S0039-6028\(97\)00092-7](http://dx.doi.org/10.1016/S0039-6028(97)00092-7).
- [155] M.T. Paffett, R.J. Simonson, P. Papin, and R.T. Paine. Borazine adsorption and decomposition at Pt(111) and Ru(001) surfaces. *Surf. Sci.*, 232:286, 1990. [http://dx.doi.org/10.1016/0039-6028\(90\)90121-N](http://dx.doi.org/10.1016/0039-6028(90)90121-N).
- [156] W. Auwarter, M. Muntwiler, J. Osterwalder, and T. Greber. Defect lines and two-domain structure of hexagonal boron nitride films on Ni(111). *Surf. Sci.*, 545: L735, 2003. <http://dx.doi.org/10.1016/j.susc.2003.08.046>.
- [157] G.B. Grad, P. Blaha, K. Schwarz, W. Auwarter, and T. Greber. Density functional theory investigation of the geometric and spintronic structure of h-BN/Ni(111) in view of photoemission and STM experiments. *Physical Review B*, 68:085404, 2003. <http://dx.doi.org/10.1103/PhysRevB.68.085404>.
- [158] M. Schmid, G. Kresse, A. Buchsbaum, E. Napetschnig, S. Gritschneder, M. Reichling, and P. Varga. Nanotemplate with holes: Ultrathin alumina on Ni<sub>3</sub>Al(111). *Phys. Rev. Lett.*, 99(19), 2007. <http://dx.doi.org/10.1103/PhysRevLett.99.196104>.
- [159] R. Laskowski, P. Blaha, T. Gallauner, and K. Schwarz. Single-layer model of the hexagonal boron nitride nanomesh on the rh(111) surface. *Phys. Rev. Lett.*, 98: 106802, 2007. <http://dx.doi.org/10.1103/PhysRevLett.98.106802>.
- [160] R. Laskowski and P. Blaha. Unraveling the structure of the h-BN/Rh(111) nanomesh with ab initio calculations. *J. Phys.: Condens. Matter*, 20, 2008. <http://dx.doi.org/10.1088/0953-8984/20/6/064207>.
- [161] F. Mueller, S. Huefner, and H. Sachdev. One-dimensional structure of boron nitride on chromium (110) - a study of the growth of boron nitride by chemical vapour deposition of borazine. *Surf. Sci.*, 602(22):3467, 2008. <http://dx.doi.org/DOI:10.1016/j.susc.2008.06.037>. <http://www.sciencedirect.com/science/article/B6TVX-4T0WJR0-1/2/d9d731dd195c08450a9f770a2c5dbc68>.
- [162] T. Greber, L. Brandenberger, M. Corso, A. Tamai, and J. Osterwalder. Single layer hexagonal boron nitride films on Ni(110). In *e.-J. Surf. Sci. Nanotech.*, 2006. <http://dx.doi.org/10.1380/ejssnt.2006.410>.

- [163] A.B. Preobrajenski, A.S. Vinogradov, and N. Martensson. Ni 3d-BN pi hybridization at the h-BN/Ni(111) interface observed with core-level spectroscopies. *Physical Review B*, 70(16), 2004. <http://dx.doi.org/10.1103/PhysRevB.70.165404>.
- [164] A.B. Preobrajenski, A.S. Vinogradov, and N. Martensson. Monolayer of h-BN chemisorbed on Cu(111) and Ni(111): The role of the transition metal 3d states. *Surf. Sci.*, 582(1):21, 2005. <http://dx.doi.org/10.1016/j.susc.2005.02.047>.
- [165] M. Muntwiler, M. Hengsberger, A. Dolocan, H. Neff, T. Greber, and J. Osterwalder. Energetics and dynamics of unoccupied electronic states at the h-BN/Ni(111) interface. *Physical Review B*, 75(7), FEB 2007. <http://dx.doi.org/10.1103/PhysRevB.75.075407>.
- [166] K. Zumbraegel, K. Wulff, C. Eibl, M. Donath, and M. Hengsberger. Exchange-split interface state at h-BN/Ni(111). *Physical Review B*, 78(8), 2008. <http://dx.doi.org/10.1103/PhysRevB.78.085422>.
- [167] M.P. Allan, S. Berner, M. Corso, T. Greber, and J. Osterwalder. Tunable self-assembly of one-dimensional nanostructures with orthogonal directions. *Nanoscale Research Letters*, 2:94, 2007. <http://dx.doi.org/10.1007/s11671-006-9036-2>.
- [168] A. Goriachko, Y. B. He, M. Knapp, H. Over, M. Corso, T. Brugger, S. Berner, J. Osterwalder, and T. Greber. Self-assembly of a hexagonal boron nitride nanomesh on Ru(0001). *Langmuir*, 23(6):2928, 2007. <http://dx.doi.org/10.1021/la062990t>.
- [169] A. Goriachko, Y.B. He, and H. Over. Complex growth of NanoAu on BN nanomeshes supported by Ru(0001). *J. Phys. Chem. C*, 112:8147, 2008. <http://dx.doi.org/10.1021/jp7119608>.
- [170] A.B. Preobrajenski, M.A. Nesterov, May Ling Ng, A.S. Vinogradov, and N. Martensson. Monolayer h-BN on lattice-mismatched metal surfaces: On the formation of the nanomesh. *Chem. Phys. Lett.*, 446(1-3):119, 2007. <http://dx.doi.org/10.1016/j.cplett.2007.08.028>.
- [171] I. Brihuega, C.H. Michaelis, J. Zhang, S. Bose, V. Sessi, J. Honolka, M.A. Schneider, A. Enders, and K. Kern. Electronic decoupling and templating of Co nanocluster arrays on the boron nitride nanomesh. *Surf. Sci.*, 602:L95, 2008. <http://dx.doi.org/10.1016/j.susc.2008.04.040>.
- [172] A.B. Preobrajenski, A.S. Vinogradov, May Ling Ng, E. Cavar, R. Westerstrom, A. Mikkelsen, E. Lundgren, and N. Martensson. Influence of chemical interaction at the lattice-mismatched h-BN/Rh(111) and h-BN/Pt(111) interfaces on the overlayer morphology. *Physical Review B*, 75(24), 2007. <http://dx.doi.org/10.1103/PhysRevB.75.245412>.

- [173] M. Corso, T. Greber, and J. Osterwalder. h-BN on Pd(110): a tunable system for self-assembled nanostructures? *Surf. Sci.*, 577:L78, 2005. <http://dx.doi.org/10.1016/j.susc.2005.01.015>.
- [174] M. Morscher, M. Corso, T. Greber, and J. Osterwalder. Formation of single layer h-BN on Pd(111). *Surf. Sci.*, 600:3280, 2006. <http://dx.doi.org/10.1016/j.susc.2006.06.016>.
- [175] J.-W. He and D.W. Goodman. Interaction of borazine with a Re(0001) surface, studied by LEED, TDS, AES and ELS. *Surf. Sci.*, 232:138, 1990. [http://dx.doi.org/10.1016/0039-6028\(90\)90594-X](http://dx.doi.org/10.1016/0039-6028(90)90594-X).
- [176] E. Cavar, R. Westerstrom, A. Mikkelsen, E. Lundgren, A.S. Vinogradov, M.L. Ng, A.B. Preobrajenski, A.A. Zakharov, and N. Martensson. A single h-BN layer on Pt(111). *Surf. Sci.*, 602(9):1722, 2008. <http://dx.doi.org/10.1016/j.susc.2008.03.008>.
- [177] R. Laskowski. Boron nitride nanomesh. In *CCP9 Conference, Cambridge*, 2008.
- [178] R. Laskowski, P. Blaha, and K.H. Schwarz. Bonding of hexagonal BN to transition metal surfaces: An ab initio density-functional theory study. *Physical Review B*, 78, 2008. <http://dx.doi.org/10.1103/PhysRevB.78.045409>.
- [179] R. Laskowski, T. Gallauner, P. Blaha, and K. Schwarz. Density functional theory simulations of B K and N K NEXAFS spectra of h-BN/transition metal(111) interfaces. *J. Phys.: Condens. Matter*, 21:104210, 2009. <http://dx.doi.org/10.1088/0953-8984/21/10/104210>.
- [180] A.B. Preobrajenski, S.A. Krasnikov, A.S. Vinogradov, May Ling Ng, T. Käämbre, A.A. Cafolla, and N. Mårtensson. Adsorption-induced gap states of h-BN on metal surfaces. *Physical Review B (Condensed Matter and Materials Physics)*, 77(8):085421, 2008. <http://dx.doi.org/10.1103/PhysRevB.77.085421>. <http://link.aps.org/abstract/PRB/v77/e085421>.
- [181] J.H. Weaver and G.D. Waddill. Cluster Assembly of Interfaces: Nanoscale Engineering. *Science*, 251:1444, 1991. <http://dx.doi.org/10.1126/science.251.5000.1444>.
- [182] F. Baletto and R. Ferrando. Structural properties of nanoclusters: Energetic, thermodynamic, and kinetic effects. *Reviews of Modern Physics*, 77:371, 2005. <http://dx.doi.org/10.1103/RevModPhys.77.371>.
- [183] K.-H. Meiweis-Broer, editor. *Metal Clusters at Surfaces*. Springer, Berlin, Heidelberg u.a., 2000.
- [184] H. Brune. *Metal Clusters at Surfaces*, chapter Growth of Metal Clusters at Surfaces, page 67. Springer, 2000.

- [185] W. Chen, K.P. Loh, H. Xu, and A.T.S. Wee. Growth of monodispersed cobalt nanoparticles on 6H-SiC(0001) honeycomb template. *Applied Physics Letters*, 84: 281, 2004. <http://dx.doi.org/10.1063/1.1639508>.
- [186] P. Milani and S. Iannotta. *Cluster Beam Synthesis of Nanostructured Materials*. Springer, Berlin, Heidelberg u.a., 1999.
- [187] G.D. Waddill, C.M. Aldao, I.M. Vitomirov, S.G. Anderson, C. Capasso, and J.H. Weaver. Ag and Co cluster deposition on GaAs(110): Fermi level pinning in the absence of metal-induced gap states and defects. *J. Vac. Sci. Technol. B*, 7:950, 1989. <http://dx.doi.org/10.1116/1.584586>.
- [188] K. Bromann, C. Felix, H. Brune, W. Harbich, R. Monot, J. Buttet, and K. Kern. Controlled deposition of size-selected silver nanoclusters. *Science*, 274:956, 1996. <http://dx.doi.org/10.1126/science.274.5289.956>.
- [189] H. Dil, J. Lobo-Checa, R. Laskowski, P. Blaha, S. Berner, J. Osterwalder, and T. Greber. Surface trapping of atoms and molecules with dipole rings. *Science*, 319:1824, 2008. <http://dx.doi.org/10.1126/science.1154179>.
- [190] M.A. Chesters, M. Hussain, and J. Pritchard. Xenon monolayer structures on copper and silver. *Surface Science*, 35:161, 1973. [http://dx.doi.org/10.1016/0039-6028\(73\)90211-2](http://dx.doi.org/10.1016/0039-6028(73)90211-2).
- [191] R.D. Diehl, T. Seyller, M. Caragiu, G.S. Leatherman, N. Ferralis, K. Pussi, P. Kaukasoina, and M. Lindroos. The adsorption sites of rare gases on metallic surfaces: a review. *J. Phys.: Condens. Matter*, 16:S2839, 2004. <http://dx.doi.org/10.1088/0953-8984/16/29/001>. Workshop on Surface Dynamics, Phonons, Adsorbate Vibrations and Diffusion, Meramec, MO, OCT 02-05, 2003.
- [192] L.W. Bruch, R.D. Diehl, and J.A. Venables. Progress in the measurement and modeling of physisorbed layers. *Rev. Mod. Phys.*, 79:1381, 2007. <http://dx.doi.org/10.1103/RevModPhys.79.1381>.
- [193] R.J. Behm, C.R. Brundle, and K. Wandelt. The underlayer influence on photoemission and thermal desorption of xenon adsorbed on Ag(111). *J. Chem. Phys.*, 85(2):1061, 1986. <http://dx.doi.org/10.1063/1.451299>.
- [194] P.C. Dai, Z. Wu, T. Angot, S.K. Wang, H. Taub, and S.N. Ehrlich. Synchrotron x-ray-diffraction study of the structure and growth of Xe films adsorbed on the Ag(111) surface. *Physical Review B*, 59:15464, 1999. <http://dx.doi.org/10.1103/PhysRevB.59.15464>.
- [195] K. Kern, R. David, P. Zeppenfeld, and G. Comsa. Registry effects in the thermodynamic quantities of Xe adsorption on Pt(111). *Surface Science*, 195(3):353, 1988. [http://dx.doi.org/10.1016/0039-6028\(88\)90347-0](http://dx.doi.org/10.1016/0039-6028(88)90347-0).

- [196] W. Widdra, P. Trischberger, W. Friess, D. Menzel, S.H. Payne, and H.J. Kreuzer. Rare-gas thermal desorption from flat and stepped platinum surfaces: Lateral interactions and the influence of dimensionality. *Physical Review B*, 57:4111, 1998. <http://dx.doi.org/10.1103/PhysRevB.57.4111>.
- [197] V. Sessi et al. in preparation. in preparation, 2009.
- [198] M. Brack. The physics of simple metal clusters: self-consistent jellium model and semiclassical approaches. *Rev. Mod. Phys.*, 65:677, 1993. <http://dx.doi.org/10.1103/RevModPhys.65.677>.
- [199] W.A. deHeer. The physics of simple metal clusters: experimental aspects and simple models. *Rev. Mod. Phys.*, 65:611, 1993. <http://dx.doi.org/10.1103/RevModPhys.65.611>.
- [200] W.D. Knight, K. Clemenger, W.A. de HEER, W.A. Saunders, M.Y. Chou, and M.L. Cohen. Electronic Shell Structure and Abundances of Sodium Clusters. *Physical Review Letters*, 52:2141, 1984. <http://dx.doi.org/10.1103/PhysRevLett.52.2141>.
- [201] E. Napetschnig, M. Schmid, and P. Varga. Pd, Co and Co-Pd clusters on the ordered alumina film on NiAl(110): Contact angle, surface structure and composition. *Surf. Sci.*, 601(15):3233, 2007. <http://dx.doi.org/10.1016/j.susc.2007.05.047>.
- [202] K.H. Hansen, T. Worren, E. Laegsgaard, F. Besenbacher, and I. Stensgaard. Bias dependent apparent height of an Al<sub>2</sub>O<sub>3</sub> thin film on NiAl(110), and of supported Pd clusters. *Surface Science*, 475:96, 2001. [http://dx.doi.org/10.1016/S0039-6028\(00\)01077-3](http://dx.doi.org/10.1016/S0039-6028(00)01077-3).
- [203] C.F. Hirjibehedin, C.P. Lutz, and A.J. Heinrich. Spin coupling in engineered atomic structures. *Science*, 312(5776):1021, 2006. <http://dx.doi.org/10.1126/science.1125398>.
- [204] A.F. Otte. *Magnetism of a Single Atom*. PhD thesis, Technische Universiteit Delft, 2008. <https://openaccess.leidenuniv.nl/handle/1887/12660>.
- [205] F. Aguilera-Granja, A. Garcia-Fuente, and A. Vega. Comparative ab initio study of the structural, electronic, and magnetic trends of isoelectronic late 3d and 4d transition metal clusters. *Physical Review B*, 78(13), OCT 2008. <http://dx.doi.org/10.1103/PhysRevB.78.134425>.
- [206] S. Datta, M. Kabir, S. Ganguly, B. Sanyal, T. Saha-Dasgupta, and A. Mookerjee. Structure, bonding, and magnetism of cobalt clusters from first-principles calculations. *Physical Review B*, 76, 2007. <http://dx.doi.org/10.1103/PhysRevB.76.014429>.



- [207] A. Kabakchiev. Pentacene molecules on the BN-nanomesh. personal communication, 2008.
- [208] J.G. Che and H.P. Cheng. First-principles investigation of a monolayer of C-60 on h-BN/Ni(111). *Physical Review B*, 72, 2005. <http://dx.doi.org/10.1103/PhysRevB.72.115436>.
- [209] I. Brihuega, S. Bose, M. Moreno, C.H. Michaelis, and K. Kern. Quantum and critical fluctuations in the superconductivity of single isolated Pb nanoparticles. *submitted*, 1:1, 2009.
- [210] I. Giaever and H.R. Zeller. Superconductivity Of Small Tin Particles Measured By Tunneling. *Phys. Rev. Lett.*, 20:1504, 1968. <http://dx.doi.org/10.1103/PhysRevLett.20.1504>.
- [211] J. Lambe and R.C. Jaklevic. Charge-Quantization Studies Using A Tunnel Capacitor. *Phys. Rev. Lett.*, 22:1371, 1969. <http://dx.doi.org/10.1103/PhysRevLett.22.1371>.
- [212] D.V. Averin and K.K. Likharev. Coulomb blockade of single-electron tunneling, and coherent oscillations in small tunnel junctions. *J. Low Temp. Phys.*, 62:345, 1986. <http://dx.doi.org/10.1007/BF00683469>.
- [213] J.B. Barner and S.T. Ruggiero. Observation of the incremental charging of Ag particles by single electrons. *Phys. Rev. Lett.*, 59:807, 1987. <http://dx.doi.org/10.1103/PhysRevLett.59.807>.
- [214] H. Graf, J. Vancea, and H. Hoffmann. Single-electron tunneling at room temperature in cobalt nanoparticles. *Appl. Phys. Lett.*, 80(7):1264, 2002. <http://dx.doi.org/10.1063/1.1450251>.
- [215] S.P.S. Arya and A. Damico. Preparation, Properties and Applications of Boron-Nitride Thin-Films. *Thin Solid Films*, 157:267, 1988. [http://dx.doi.org/10.1016/0040-6090\(88\)90008-9](http://dx.doi.org/10.1016/0040-6090(88)90008-9).
- [216] R. Wilkins, M. Amman, E. Benjacov, and R.C. Jaklevic. Single-electron and oxide-impurity effects in junctions formed by a cryogenic scanning tunneling microscope. *Physical Review B*, 42:8698, 1990. <http://dx.doi.org/10.1103/PhysRevB.42.8698>.
- [217] C. Schonenberger, H. Vanhouten, and H.C. Donkersloot. Single-Electron Tunnelling Observed at Room Temperature by Scanning-Tunnelling Microscopy. *Europhys. Lett.*, 20:249, 1992. <http://dx.doi.org/10.1209/0295-5075/20/3/010>.
- [218] D. Anselmetti, T. Richmond, A. Baratoff, G. Borer, M. Dreier, M. Bernasconi, and H. J. Guntherodt. Single-Electron Tunnelling at Room Temperature with Adjustable Double-Barrier Junctions. *Europhys. Lett.*, 25:297, 1994. <http://dx.doi.org/10.1209/0295-5075/25/4/010>.

- [219] P.N. First, J.A. Strosio, R.A. Drogoset, D.T. Pierce, and R.J. Celotta. Metallicity and gap states in tunneling to Fe clusters in GaAs(110). *Physical Review Letters*, 63:1416, 1989. <http://dx.doi.org/10.1103/PhysRevLett.63.1416>.
- [220] J.A. Alonso. Electronic and atomic structure, and magnetism of transition-metal clusters. *Chemical Reviews*, 100:637, 2000. <http://dx.doi.org/10.1021/cr980391o>.
- [221] R. Kubo, A. Kawabata, and S. Kobayashi. Electronic Properties of Small Particles. *Annual Reviews of Materials Science*, 14:49, 1984. <http://dx.doi.org/10.1146/annurev.ms.14.080184.000405>.
- [222] K. Schouteden, A. Lando, E. Janssens, C. Van Haesendonck, and P. Lievens. Morphology and electron confinement properties of Co clusters deposited on Au(111). *New Journal Of Physics*, 10, 2008. <http://dx.doi.org/10.1088/1367-2630/10/8/083005>.
- [223] R.C. Ashoori. Electrons in artificial atoms. *Nature*, 379:413, 1996. <http://dx.doi.org/10.1038/379413a0>.
- [224] F. Aguilera-Granja, J.A. Alonso, and J.M. Montejano-Carrizales. Theoretical study of the metal-nonmetal transition in transition metal clusters. In JL Moran-Lopez, editor, *Current Problems in Condensed Matter*, page 109, 1998. ISBN 0-306-45915-9.
- [225] X. Lin, N. Nilius, H.-J. Freund, M. Walter, P. Frondelius, K. Honkala, and H. Häkkinen. Quantum Well States in Two-Dimensional Gold Clusters on MgO Thin Films. *Physical Review Letters*, 102:206801, 2009. <http://dx.doi.org/10.1103/PhysRevLett.102.206801>.
- [226] N. Fujima and S. Sakurai. Magnetic Shells of Co Clusters. *Journal of the Physical Society of Japan*, 68:586, 1999. <http://dx.doi.org/10.1143/JPSJ.68.586>.
- [227] S. Gueron, Mandar M. Deshmukh, E.B. Myers, and D.C. Ralph. Tunneling via Individual Electronic States in Ferromagnetic Nanoparticles. *Phys. Rev. Lett.*, 83:4148, 1999. <http://dx.doi.org/10.1103/PhysRevLett.83.4148>.
- [228] R. Desmicht, G. Faini, V. Cros, A. Fert, F. Petroff, and A. Vaures. Point-contact electrodes to probe charging effects in individual ultrasmall cobalt clusters. *Applied Physics Letters*, 72:386, 1998. <http://dx.doi.org/10.1063/1.120744>.
- [229] T.W. Odom, J.L. Huang, C.L. Cheung, and C.M. Lieber. Magnetic clusters on single-walled carbon nanotubes: The Kondo effect in a one-dimensional host. *Science*, 290:1549, 2000. <http://dx.doi.org/10.1126/science.290.5496.1549>.
- [230] K. Sell, A. Kleibert, V.V. Oeynhausen, and K.H. Meiwes-Broer. The structure of cobalt nanoparticles on Ge(001). *European Physical Journal D*, 45:433, 2007. <http://dx.doi.org/10.1140/epjd/e2007-00213-7>.

- [231] R. Singh and P. Kroll. Structural, electronic, and magnetic properties of 13-, 55-, and 147-atom clusters of Fe, Co, and Ni: A spin-polarized density functional study. *Physical Review B*, 78, 2008. <http://dx.doi.org/10.1103/PhysRevB.78.245404>.
- [232] Q-M. Ma, Z. Xie, J. Wang, Y. Liu, and Y-C. Li. Structures, stabilities and magnetic properties of small Co clusters. *Physics Letters A*, 358:289, 2006. <http://dx.doi.org/10.1016/j.physleta.2006.05.033>.
- [233] J.L. Rodriguez-Lopez, F. Aguilera-Granja, K. Michaelian, and A. Vega. Structure and magnetism of cobalt clusters. *Physical Review B*, 67, 2003. <http://dx.doi.org/10.1103/PhysRevB.67.174413>.
- [234] P. Gambardella, S. Rusponi, M. Veronese, S.S. Dhesi, C. Grazioli, A. Dallmeyer, I. Cabria, R. Zeller, P.H. Dederichs, K. Kern, C. Carbone, and H. Brune. Giant magnetic anisotropy of single cobalt atoms and nanoparticles. *Science*, 300:1130, 2003. <http://dx.doi.org/10.1126/science.1082857>.
- [235] A.N. Andriotis and M. Menon. Tight-binding molecular-dynamics study of ferromagnetic clusters. *Physical Review B*, 57:10069, 1998. <http://dx.doi.org/10.1103/PhysRevB.57.10069>.
- [236] M.B. Knickelbein. Magnetic moments of bare and benzene-capped cobalt clusters. *Journal of Chemical Physics*, 125, 2006. <http://dx.doi.org/10.1063/1.2217951>.
- [237] I. Horcas, R. Fernandez, J.M. Gomez-Rodriguez, J. Colchero, J. Gomez-Herrero, and A.M. Baro. WSXM: A software for scanning probe microscopy and a tool for nanotechnology. *Rev. Sci. Instrum.*, 78:013705, 2007. <http://dx.doi.org/10.1063/1.2432410>.
- [238] J.P. Hurault, K. Maki, and M.T. Bealmondo. Fluctuations of the Order Parameter in Small Superconducting Samples. *Physical Review B*, 3:762, 1971. <http://dx.doi.org/10.1103/PhysRevB.3.762>.
- [239] R.A. Buhrman and W.P. Halperin. Fluctuation Diamagnetism in a Zero-Dimensional Superconductor. *Phys. Rev. Lett.*, 30:692, 1973. <http://dx.doi.org/10.1103/PhysRevLett.30.692>.
- [240] J. P. Gollub, M. R. Beasley, R. Callarot, and M. Tinkham. Fluctuation-Induced Diamagnetism above  $T_c$  in Superconductors. *Physical Review B*, 7(7):3039, 1973. <http://dx.doi.org/10.1103/PhysRevB.7.3039>.
- [241] R.C. Dynes, J.P. Garno, G.B. Hertel, and T.P. Orlando. Tunneling Study of Superconductivity near the Metal-Insulator Transition. *Phys. Rev. Lett.*, 53:2437, 1984. <http://dx.doi.org/10.1103/PhysRevLett.53.2437>.

- [242] H.M. Jaeger, D.B. Haviland, B.G. Orr, and A.M. Goldman. Onset Of Superconductivity In Ultrathin Granular Metal-Films. *Physical Review B*, 40:182, 1989. <http://dx.doi.org/10.1103/PhysRevB.40.182>.
- [243] E. Bernardi, A. Lascialfari, A. Rigamonti, L. Romano, V. Iannotti, G. Ausanio, and C. Luponio. Zero-dimensional superconducting fluctuations and fluctuating diamagnetism in lead nanoparticles. *Phys. Rev. B*, 74(13), 2006. <http://dx.doi.org/10.1103/PhysRevB.74.134509>.
- [244] N.C. Koshnick, H. Bluhm, M.E. Huber, and K.A. Moler. Fluctuation superconductivity in mesoscopic aluminum rings. *Science*, 318:1440, 2007. <http://dx.doi.org/10.1126/science.1148758>.
- [245] J. Bardeen, L.N. Cooper, and J.R. Schrieffer. Theory of Superconductivity. *Physical Review*, 108(5):1175, 1957. <http://dx.doi.org/10.1103/PhysRev.108.1175>.
- [246] L. Solymar. *Superconducting Tunnelling and Applications*. Chapman and Hall, 1972.
- [247] S. Skalski, O. Betbeder, and P.R. Weiss. Properties of Superconducting Alloys Containing Paramagnetic Impurities. *Physical Review A*, 136:1500, 1964. <http://dx.doi.org/10.1103/PhysRev.136.A1500>.
- [248] A. Larkin and A. Varlamov. *Theory of fluctuations in superconductors*. Clarendon Press, Oxford, 2005.
- [249] L.G. Aslamazo and A.I. Larkin. Effect of Fluctuations on Properties of a Superconductor above Critical Temperature. *Soviet Physics Solid State, USSR*, 10:875, 1968.
- [250] L. G. Aslamazo and A. I. Larkin. Influence of Fluctuation Pairing of Electrons on Conductivity of Normal Metal. *Physics Letters A*, A 26:238, 1968.
- [251] V.L. Ginzburg and L.D. Landau. Theory of superconductivity. *Zhurnal Eksperimental'noi i Teoreticheskoi Fiziki*, 20:1064, 1950.
- [252] M. Tinkham. *Introduction to superconductivity*. Dover Publ., Mineola, NY, 2004.
- [253] C.T. Black, D.C. Ralph, and M. Tinkham. Spectroscopy of the superconducting gap in individual nanometer-scale aluminum particles. *Phys. Rev. Lett.*, 76:688–691, 1996. <http://dx.doi.org/10.1103/PhysRevLett.76.688>.
- [254] K. Wang, X. Zhang, M.M.T. Loy, T.-C. Chiang, and X. Xiao. Pseudogap Mediated by Quantum-Size Effects in Lead Islands. *Phys. Rev. Lett.*, 102:076801, 2009. <http://dx.doi.org/10.1103/PhysRevLett.102.076801>.

- [255] C. Brun, I.-P. Hong, F. Patthey, I.Y. Sklyadneva, R. Heid, P.M. Echenique, K.P. Bohnen, E.V. Chulkov, and W.-D. Schneider. Reduction of the Superconducting Gap of Ultrathin Pb Islands Grown on Si(111). *Physical Review Letters*, 102:207002, 2009. <http://dx.doi.org/10.1103/PhysRevLett.102.207002>.
- [256] B. Abeles, R.W. Cohen, and G.W. Cullen. Enhancement of Superconductivity in Metal Films. *Phys. Rev. Lett.*, 17:632, 1966. <http://dx.doi.org/10.1103/PhysRevLett.17.632>.
- [257] W.H. Li, C.C. Yang, F.C. Tsao, and K.C. Lee. Quantum size effects on the superconducting parameters of zero-dimensional Pb nanoparticles. *Physical Review B*, 68:184507, 2003. <http://dx.doi.org/10.1103/PhysRevB.68.184507>.
- [258] W.H. Li, C.C. Yang, F.C. Tsao, S.Y. Wu, P.J. Huang, M.K. Chung, and Y.D. Yao. Enhancement of superconductivity by the small size effect in In nanoparticles. *Physical Review B*, 72:214516, 2005. <http://dx.doi.org/10.1103/PhysRevB.72.214516>.
- [259] W. H. Li, C. W. Wang, C. Y. Li, C.K. Hsu, C.C. Yang, and C. M. Wu. Coexistence of ferromagnetism and superconductivity in Sn nanoparticles. *Physical Review B*, 77, 2008. <http://dx.doi.org/10.1103/PhysRevB.77.094508>.
- [260] S. Bose, P. Raychaudhuri, R. Banerjee, P. Vasa, and P. Ayyub. Mechanism of the size dependence of the superconducting transition of nanostructured Nb. *Phys. Rev. Lett.*, 95(14), 2005. <http://dx.doi.org/10.1103/PhysRevLett.95.147003>.
- [261] K.H. Bennemann and J.B. Ketterson. *Superconductivity*, volume 1: Conventional and Unconventional Superconductors. Springer, Berlin ; Heidelberg, 2008. <http://dx.doi.org/10.1007/978-3-540-73253-2>.
- [262] M. Zgirski, K.-P. Riikonen, V. Touboltsev, and K. Y. Arutyunov. Quantum fluctuations in ultranarrow superconducting aluminum nanowires. *Physical Review B*, 77, 2008. <http://dx.doi.org/10.1103/PhysRevB.77.054508>.
- [263] K.Y. Arutyunov, D.S. Golubev, and A.D. Zaikin. Superconductivity in one dimension. *Physics Reports-Review Section of Physics Letters*, 464(1-2):1–70, JUL 2008. <http://dx.doi.org/10.1016/j.physrep.2008.04.009>.
- [264] R.C. Dynes, V. Narayanamurti, and J.P. Garno. Direct Measurement of Quasiparticle-Lifetime Broadening in Strong-Coupled Superconductor. *Phys. Rev. Lett.*, 41:1509, 1978. <http://dx.doi.org/10.1103/PhysRevLett.41.1509>.
- [265] V.A. Schweigert and F.M. Peeters. Phase transitions in thin mesoscopic superconducting disks. *Physical Review B*, 57:13817, 1998.
- [266] T. Nishio, T. An, A. Nomura, K. Miyachi, T. Eguchi, H. Sakata, S. Lin, N. Hayashi, N. Nakai, M. Machida, and Y. Hasegawa. Superconducting Pb Island Nanostructures Studied by Scanning Tunneling Microscopy and Spectroscopy. *Phys.*

- Rev. Lett.*, 101:167001, 2008. <http://dx.doi.org/10.1103/PhysRevLett.101.167001>. <http://link.aps.org/abstract/PRL/v101/e167001>.
- [267] S.P. Chockalingam, M. Chand, A. Kamlapure, J. Jesudasan, A. Mishra, V. Tripathi, and P. Raychaudhuri. Tunneling studies in a homogeneously disordered s-wave superconductor: NbN. *Physical Review B*, 79:094509, 2009. <http://dx.doi.org/10.1103/PhysRevB.79.094509>.
  - [268] S. Bose, V.M. Silkin, R. Ohmann, I. Brihuega, L. Vitali, C.H. Michaelis, P. Mallet, J.Y. Veuillen, M.A. Schneider, E.V. Chulkov, P.M. Echenique, and K. Kern. Image potential states as quantum probe of graphene interfaces. *subm.*, 2009.
  - [269] S. Matsuo, H. Sugiura, and S. Noguchi. Superconducting Transition-Temperature Of Aluminum, Indium, And Lead Fine Particles. *J. Low Temp. Phys.*, 15(5):481, 1974. <http://dx.doi.org/10.1007/BF00654622>.
  - [270] J.M. Dickey and A. Paskin. Phonon Spectrum Changes in Small Particles and Their Implications for Superconductivity. *Phys. Rev. Lett.*, 21:1441, 1968. <http://dx.doi.org/10.1103/PhysRevLett.21.1441>.
  - [271] W.L. McMillan. Transition Temperature Of Strong-Coupled Superconductors. *Physical Review*, 167:331, 1968. <http://dx.doi.org/10.1103/PhysRev.167.331>.
  - [272] M. Strongin, R.S. Thompson, O.F. Kammerer, and J.E. Crow. Destruction Of Superconductivity In Disordered Near-Monolayer Films. *Physical Review B*, 1: 1078, 1970. <http://dx.doi.org/10.1103/PhysRevB.1.1078>.
  - [273] L-P. Levy. *Magnetism and Superconductivity*. Springer, Berlin, Heidelberg, 2000.
  - [274] W.J. Skocpol and M. Tinkham. Fluctuations near superconducting phase transitions. *Reports on Progress in Physics*, 38:1049, 1975. <http://dx.doi.org/10.1088/0034-4885/38/9/001>.
  - [275] S. Huefner, M.A. Hossain, A. Damascelli, and G.A. Sawatzky. Two gaps make a high-temperature superconductor? *Reports on Progress in Physics*, 71, 2008. <http://dx.doi.org/10.1088/0034-4885/71/6/062501>.
  - [276] N. Bergeal, J. Lesueur, M. Aprili, G. Faini, J.P. Contour, and B. Leridon. Pairing fluctuations in the pseudogap state of copper-oxide superconductors probed by the Josephson effect. *Nature Physics*, 4:608, 2008. <http://dx.doi.org/10.1038/nphys1017>.
  - [277] H. Meissner. Measurements on Superconducting Contacts. *Physical Review*, 109: 686, 1958. <http://dx.doi.org/10.1103/PhysRev.109.686>.
  - [278] H. Meissner. Superconductivity of Contacts with Interposed Barriers. *Physical Review*, 117:672, 1960. <http://dx.doi.org/10.1103/PhysRev.117.672>.

- [279] A.I. Buzdin. Proximity effects in superconductor-ferromagnet heterostructures. *Rev. Mod. Phys.*, 77:935, 2005. <http://dx.doi.org/10.1103/RevModPhys.77.935>.
- [280] P. Hilsch. Zum Verhalten von Supraleitern im Kontakt mit Normalleitern. *Zeitschrift fuer Physik A Hadrons and Nuclei*, 167:511, 1962. <http://dx.doi.org/10.1007/BF01378178>.
- [281] O. Bourgeois, A. Frydman, and R.C. Dynes. Proximity effect in ultrathin Pb/Ag multilayers within the Cooper limit. *Physical Review B*, 68, 2003. <http://dx.doi.org/10.1103/PhysRevB.68.092509>.
- [282] I. Sternfeld, V. Shelukhin, A. Tsukernik, M. Karpovski, A. Gerber, and A. Palevski. Proximity effect in granular superconductor-normal metal structures. *Physical Review B*, 71, 2005. <http://dx.doi.org/10.1103/PhysRevB.71.064515>.
- [283] S. Bose and P. Ayyub. Superconducting proximity effect in Pb/Ag nanocomposites. *Physical Review B*, 76, 2007. <http://dx.doi.org/10.1103/PhysRevB.76.144510>.
- [284] H. le Sueur, P. Joyez, H. Pothier, C. Urbina, and D. Esteve. Phase Controlled Superconducting Proximity Effect Probed by Tunneling Spectroscopy. *Phys. Rev. Lett.*, 100(19):197002, 2008. <http://dx.doi.org/10.1103/PhysRevLett.100.197002>. <http://link.aps.org/abstract/PRL/v100/e197002>.
- [285] S. Bose. *Finite size effects in nanocrystalline superconductors*. PhD thesis, Tata Institute of Fundamental Research, Mumbai, India, 2007.
- [286] V.Z. Kresin and Y.N. Ovchinnikov. Shell structure and strengthening of superconducting pair correlation in nanoclusters. *Physical Review B*, 74, 2006. <http://dx.doi.org/10.1103/PhysRevB.74.024514>.
- [287] H. Olofsson, S. Aberg, and P. Leboeuf. Semiclassical theory of Bardeen-Cooper-Schrieffer pairing-gap fluctuations. *Physical Review Letters*, 100, 2008. <http://dx.doi.org/10.1103/PhysRevLett.100.037005>.
- [288] A.M. Garcia-Garcia, J.D. Urbina, E.A. Yuzbashyan, K. Richter, and B.L. Altshuler. Bardeen-Cooper-Schrieffer theory of finite-size superconducting metallic grains. *Physical Review Letters*, 100, 2008. <http://dx.doi.org/10.1103/PhysRevLett.100.187001>.
- [289] J. von Delft. Superconductivity in Ultrasmall Metallic Grains. *Annalen der Physik*, 10:219, 2001. [http://dx.doi.org/10.1002/1521-3889\(200103\)10:3<219::AID-ANDP219>3.0.CO;2-I](http://dx.doi.org/10.1002/1521-3889(200103)10:3<219::AID-ANDP219>3.0.CO;2-I).
- [290] R.W. Cohen and B. Abeles. Superconductivity in Granular Aluminum Films. *Physical Review*, 168:444, 1968. <http://dx.doi.org/10.1103/PhysRev.168.444>.

- [291] R.W. Richardson. A restricted class of exact eigenstates of the pairing-force Hamiltonian. *Physics Letters*, 3:277, 1963. [http://dx.doi.org/doi:10.1016/0031-9163\(63\)90259-2](http://dx.doi.org/doi:10.1016/0031-9163(63)90259-2).
- [292] E.A. Yuzbashyan, A.A. Baytin, and B.L. Altshuler. Finite-size corrections for the pairing Hamiltonian. *Physical Review B*, 71, 2005. <http://dx.doi.org/10.1103/PhysRevB.71.094505>.
- [293] M. Brack and R.K. Bhadhuri. *Semiclassical Physics*. Addison Wesley, New York, 1997.
- [294] C.H. Chang. Transfer operator approach on three-dimensional quantum billiards with SO(2) symmetry. *Physical Review E*, 67, 2003. <http://dx.doi.org/10.1103/PhysRevE.67.046201>.
- [295] N.W. Ashcroft and N.D. Mermin. *Solid State Physics*. Brooks Cole, 1976.
- [296] R.W. Cohen and B. Abeles. Granular Superconductors. *J. Appl. Phys.*, 39:2560, 1968. <http://dx.doi.org/10.1103/PhysRev.168.444>.
- [297] T. Cren, D. Fokin, F. Debontridder, V. Dubost, and D. Roditchev. Ultimate Vortex Confinement Studied by Scanning Tunneling Spectroscopy. *Phys. Rev. Lett.*, 102:127005, 2009. <http://dx.doi.org/10.1103/PhysRevLett.102.127005>. <http://link.aps.org/abstract/PRL/v102/e127005>.
- [298] I. Brihuega, P. Mallet, C. Bena, S. Bose, C. Michaelis, L. Vitali, F. Varchon, L. Magaud, K. Kern, and J.Y. Veuillen. Quasiparticle Chirality in Epitaxial Graphene Probed at the Nanometer Scale. *Phys. Rev. Lett.*, 101:206802, 2008. <http://dx.doi.org/10.1103/PhysRevLett.101.206802>.
- [299] M. Hoesch, M. Muntwiler, V.N. Petrov, M. Hengsberger, L. Patthey, M. Shi, M. Falub, T. Greber, and J. Osterwalder. Spin structure of the Shockley surface state on Au (111). *Phys. Rev. B*, 69:241401, 2004. <http://dx.doi.org/10.1103/PhysRevB.69.241401>.



# Curriculum vitae

Christian Heinrich Michaelis

1979 born in Jena, Germany  
married, three children

1998 Abitur

1998 Civil service

2004 Diploma in materials science, Friedrich Schiller University Jena, Germany

2004 Ass. Project Leader, EMS Electro Medical Systems, Nyon/Lausanne, Switzerland

2005 PhD student at the Max Planck Institute for Solid State Research, Stuttgart, Germany

A more detailed cv is available on request from the author.



# Danksagung

Zum Schluss möchte ich all jenen danken, die zum Gelingen dieser Arbeit beigetragen haben:

- Prof. Dr. Klaus Kern für die Vergabe des Themas und die Möglichkeit in seiner Abteilung zu arbeiten, für die vielen Diskussionen und die Unterstützung während meiner Zeit am Max-Planck-Institut in Stuttgart.
- Prof. Dr. E. Scheer, Prof. Dr. S. Mecking und Prof. Dr. P. Nielaba von der Universität Konstanz für die freundliche Bereitschaft als Gutachter und Prüfer zu fungieren.
- Prof. Dr. M. Alexander Schneider für die gründliche Einführung zu Beginn meiner Zeit in Stuttgart.
- Dres. Peter Wahl, Christian Ast, Lucia Vitali und Klaus Kuhnke, die stets ein offenes Ohr für meine Fragen hatten.
- Dr. Ivan Brihuega für die weitere Betreuung der Doktorarbeit zusammen mit Dr. Sangita Bose.
- Dr. Markus Ternes für die Betreuung am Ende und für die Hilfe bei der Erstellung der Doktorarbeit (zusammen mit S. Bose).
- Max Assig, mit dem man wunderbar über Tieftemperaturprobleme diskutieren kann.
- Robin Ohmann vom 4K-STM, mein Trauzeuge.
- Violetta Sessi, für die Entführung in die Welt der Synchrotrons und die Motivation im Kopf-an-Kopf-Rennen.
- Miguel Moreno, Tobias Herden und Steffen Kahle vom subK Team. Tobias macht tolle Fotos.
- Dres. Sebastian Stepanow und Stephan Rauschenbach mit dem Team der IBD.
- Allen Werkstätten und Servicegruppen im Haus: den Technikern der Abteilung (Wolfgang Stiepany, Peter Andler, Andreas Koch und v.a. Rafail Chaikevitch),

der Kristallpräparation, dem Tieftemperaturservice, der feinmechanischen Werkstatt, der großen Werkstatt, den Glasbläsern, der Elektronik, der Haustechnik und der Verwaltung.

- Meinen Kollegen als Doktorandensprecher: Hasan, Peter und Roland.
- Dr. Peter P. Schepp und Anja Mangold von der Deutschen Gesellschaft für Materialkunde, Frankfurt.
- Der Stadt Stuttgart für die Übernahme der Kosten für die Tagesmutter und für die Kitaplätze. Der Stiftung Familie in Not des Landes Baden-Württemberg für die finanzielle Unterstützung.
- Meiner Familie, besonders Opa Bernhard, der uns während Konferenzen immer eine große Hilfe war.

Der größte Dank gilt meiner Frau und insbesondere meinen Kindern Judith (\*2005), Dorothee (\*2007) und Clemens (\*2009), deren Lachen schöner ist als jedes supraleitende Spektrum

